UNIVERSITY OF CALIFORNIA, SAN DIEGO

# Application of Microfluidic Device for the Study of Bacteria

A dissertation submitted in partial satisfaction of the
requirements for the degree Doctor of Philosophy

in

Physics

by

Chih-Yu Yang

Committee in charge:

Professor Alex Groisman, Chair
Professor Lin Chao
Professor Terence Hwa
Professor Gürol Süel
Professor Massimo Vergassola

2018

The Dissertation of Chih-Yu Yang is approved, and it is acceptable in quality and form for publication on microfilm and electronically:

_____

_____

_____

_____

_____

Chair

University of California, San Diego

2018

TABLE OF CONTENTS

LIST OF FIGURES

LIST OF TABLES

ACKNOWLEDGEMENTS

This degree would not be achieved without the help of people. I would like to share the honor with all my mentors, colleagues, friends, and family, who gave me a lot of advice and support me when I was upset during these five years.

First, I would like to express my sincere appreciation to my advisor, Dr. Alex Groisman, for his support to my research. He was patient when I made mistakes, and guided me when I struggled. I would like to thank Dr. Terence Hwa, Dr. Massimo Vergassola, Dr. Gürol Süel, and Dr. Lin Chao, for their participation in my committee. Their inspiration to my graduate research was valuable not only for the past doctoral research, but also for the future work.

I would like to thank the lab members, Dr. Edgar Gutierrez, Dr. Mihael Erickstad, and Edward Ronan. They provided me with valuable advice and knowledge toward physics and biology. They shared their experience with me, selflessly. I would also like to thank Dr. Jérôme Wong Ng, Dr. Jonas Cremer, Dr. Igor Segota, Dr. Markus Arnoldini, Tomoya Honda, and John T. Sauls, not only as colleagues, but also as friends. The projects would not be accomplished without their efficient and effective collaboration. Furthermore, I would like to thank all the collaborators and friends for accompanying me working hard.

Thank you, my parents, for bringing me to the world, providing for me with resources and freedom to learn whatever I would like to learn, and endowing me with the enthusiasm for the love of science.

Last but not least, thank you, my wife, Nicole Lee, for the endless love and support. Thanks for sharing both pleasure and sadness, and making me a better man. Thank you, my daughter, Nian Yang, for bringing smiles and laughs to my world. Thank you, my little

daughter, who is about to be born in May, 2018, for bringing me expect to the whole new life.

Thanks to everyone who helped me and taught me in San Diego.

Chapter 2 covers the materials from the manuscript "The Aggregation Temperature of *E.coli* Depends on the Steepness of Thermal Gradient" by Chih-Yu Yang, Michael Erickstad, Jérôme Wong Ng, Edgar Gutierrez, and Alex Groisman. The manuscript was completed and ready to be submitted to *Biophysical Journal*. The dissertation author was the first author of the manuscript.

Chapter 3 covers the materials from "Effect of Flow and Peristaltic Mixing on Bacterial Growth in a Gut-like Channel" by Jonas Cremer, Igor Segota, Chih-Yu Yang, Markus Arnoldini, John T. Sauls, Zhongge Zhang, Edgar Gutierrez, Alex Groisman, and Terence Hwa, which was published in *Proceedings of the National Academy of Sciences* in 2016. The dissertation author was the co-author of this paper, in charge of gut-like device manufacture and flow characterization.

Appendix A is the project to apply porous device to study environmental stress response of *E.coli*. The project was not fully finished and more future works need to be done.

## VITA

2011 B. S. in Physics, National Taiwan University, Taiwan.

2014 M. S. in Physics, University of California San Diego, La Jolla

2018 Ph. D. in Physics, University of California San Diego, La Jolla.

## PUBLICATIONS

Journal Article

- Chih-Yu Yang, Michael Erickstad, Jérôme Wong-Ng, Edgar Gutierrez, Alex Groisman. "The aggregation temperature of *E.coli* depends on the steepness of thermal gradient" (manuscript)
- Jonas Cremer*, Igor Segota*, Chih-Yu Yang, Markus Arnoldini, John T. Sauls, Zhongge Zhang, Edgar Gutierrez, Alex Groisman, Terence Hwa."The effect of flow and peristaltic mixing on bacterial growth in a gut-like channel", *PNAS* 113:11414-9 (2016).

ABSTRACT OF THE DISSERTATION

Application of Microfludic device for the Study of Bacteria

by

Chih-Yu Yang

Doctor of Philosophy in Physics

University of California, San Diego, 2018

Professor Alex Groisman, Chair

Microfluidic device has been widely used in biological research, due to not only the dimension, but also its ability of fresh medium supply, medium exchange, gradients generation, and force control. This study applied microfluidic device in research of bacterial behavior, including chemotaxis, thermotaxis, bacterial growth in a gut-like channel, and mechanical stress response. *E.coli* was used in all our experiments because it is a relatively well-studied organism.

Bacterial chemotaxis is a movement in response to spatially chemical gradients. Similar to chemotaxis, bacterial thermotaxis is the response of bacteria toward spatial temperature gradients. Linear temperature gradients were created by microfluidic device,

and *E.coli* were loaded in the device to test its spatial. The result was surprising, showing that temperature preference of *E.coli* is a function of temperature gradient rather than a constant.

Organ-on-chip is one of the broad applications of microfluidic device, and we applied it to study bacterial growth in a gut-like channel. The human microbiome in the gut has been shown to play important roles in the health. To better understand the population dynamics of microbes in proximal colon, a gut-like channel was built by a fluidic device called “minigut”. Such device mimicked the contractions and peristaltic movement of human gut. With the minigut device and theoretical analysis, the bacterial spatial density profile could be studied. The results suggest that flow and mixing play a major role in shaping the microbiota of the colon.

Moreover, microfluidic device was applied to study bacterial stress response. A porous device was designed to physically confine *E.coli* while providing adequate nutrient through diffusion for their growth. The goal was to test the response and molecular regulation of *E.coli* toward mechanical stress.

Overall, microfluidic device provided appropriate environmental conditions to study bacterial behavior, which could not be done by traditional methods. With such combination between physics and biology, more experimental research could be reached and conducted.

# CHAPTER 1

# INTRODUCTION

Microfluidic device has been widely used in biological research. The order of magnitude of its cross-section is between 0.1~500 μm, covering the size of many microorganism from *E.coli* mammalian cells, to Caenorhabditis elegans. Such dimension makes it an excellent experimental tool for microorganism. In addition, microfluidic device has the ability of nutrient supply, cell sorting, gradient generation, and force control, due to the continuous flow generated by the pressure difference between inlets and outlets. Therefore, microfluidic device could be designed as a chemostat for cell growth, applied to sort particles with different sizes, and manipulate single cell. There are a lot more applications of microfluidic device such as digital PCR, electric field generation, droplet manipulation, and so on, but this thesis only focuses on the application to gradient generation, nutrient supply, and force control. Before further discuss, it is better to define the coordinates in chapter 1 to simplify the explanation, by assuming x as the direction of flow, y as the direction of the width of channel, and z as the direction of the height of channel.

Based on the theory of flow dynamics (1), microfluidic device is able to create laminar flow due to its low Reynolds number, which is proportional to the scale of cross-sectional length and flow velocity. If the cross-sectional length scale of device is above the

order of 10 mm, turbulent flow will be easily generated, which influence the characterized flow pattern. Laminar flow is the flow that there is no interruption between parallel layers (along x direction). Each molecule in flow will follow the same streamline, and will not move in the direction perpendicular to the wall. Therefore, with no external force, microorganism such as bacteria will remain the same horizontal position (y position) relative to the wall, which is extremely important especially when studying bacterial taxis. In addition, flow velocity pattern along cross-section depends on cross-sectional shape. For an instance, based on the Navier-Stokes equation, if the shape is a rectangular cross-section with large width-height (y/z) ratio, the flow velocity pattern results in a parabola along z direction but quite a plateau pattern along y direction. A plateau pattern means that except the region close to two sides of walls, the flow velocity is almost a constant in the major center region, assuming the width-height ratio is large enough. For an example, if the width of channel is 10 (y position between -5 and 5) and height of channel is 1 (z position between 0 and 1), the velocity at y = 4, z = 0.5 is only 5% different from the velocity at y = 0, z = 0.5. Consequently, most of particles in the same layer (x position) loaded in the channel will proceed together with the same velocity. As a result, the traveling time between each molecule in the same x position is the same, except molecules near the side walls. This is important in biological experiment, because one can be sure that all cells at the same x position experience the same amount of time interval in experimental setup, such as nutrients, antibiotic, and so on. Therefore, rectangular cross-sectional microfluidic device has a lot of advantages and was applied in this research.

There are several ways to manufacture microfluidic device. Traditional photolithography is the most widely used method, due to the well-established

manufacturing protocol and fine structure it can reach. The photolithography process is as follows. SU-8 photoresist is commonly used as the base of mold, which is spin-coated on a silicon wafer. The thickness of SU-8 on silicon wafer depends on the speed and time of spin-coating. After pre-baking process, the wafer with SU-8 is placed beneath photomask, which has microfluidic pattern on it, and exposed under UV light. SU-8 absorbs wavelength of UV region, allowing fabrication of thick structure with relatively vertical sides. After post-baking process, UV-treated SU-8 is washed by SU-8 developer, to remove the part not solidified. If the device has multilayers, same process is followed before developing. After the SU-8 fabrication mold is made, Polydimethylsiloxane (PDMS) is poured on the mold, baked, and solidified. As a result, a microfluidic device made of PDMS is created and can be bound with coverslip to form a closed device.

However, photolithography is time consuming, especially for thick layer (>100μm) wafer. It takes several hours to make a single wafer. Although one layer contains several independent molds, once making a mistake such as wrong thickness, one has to redo the whole process all over again. Moreover, it is not convenient to make a device thicker than 300 μm by photolithography. Therefore, to make a device with large thickness, such as the minigut research in this thesis, one needs to take alternative methods. Laser cutting is a faster way to make device. It only takes minutes to cut a mold controlled by programming software. Laser is the tool to shape the device, which the focused beam is about 0.001 inches. Laser cutting is not able to create a fine structure comparing to photolithography, but it is good enough for large scale device which those defects can be ignored. In this study, acrylic is used as a material for laser cutting, and bound with solidified PDMS, to

make a minigut device. There are more ways for microfluidic device manufacturing such as 3D printing, which is a novel way to create complicated 3D device.

In this study, microfluidic device was applied in research of bacterial behavior, including chemotaxis, thermotaxis, bacterial growth in a gut-like channel, and mechanical stress response.

Chapter 2 describes the research in bacterial thermotaxis, with linear temperature gradients generated by microfluidic device. Comparing to chemotaxis, which *E.coli* accumulate toward either the highest or the lowest concentration among a spatial chemical gradient, thermotaxis involves an intermediate accumulation of *E.coli* in a spatial temperature gradient. Instead of gathering toward the highest or lowest temperature in environment, studies showed that *E.coli* are able to find and accumulate around intermediate temperature. Experiment was conducted by loading cells in a spatial temperature profile. Based on existing thermotaxis theory, bacteria are able to do random walk and reach equilibrium with enough time. Results showed a linear relation between accumulating temperature and temperature gradient, which means that the temperature preference of *E.coli* is a function of temperature gradients rather than a constant.

Chapter 3 presents the study of bacterial growth in a gut-like channel under contraction movement, supported from the Bill and Melinda Gates Foundation through the Healthy Birth, Growth, and Development knowledge integration program. The human microbiome in the gut has been shown to play important roles in the health. To better understand the population dynamics of microbes in proximal colon, a device called “minigut” was created to provide not only the environment for bacterial growth but also peristaltic wave mimicking gut contraction. The net flow generated by pressure difference

between inlet and outlet supplied nutrients for bacterial growth, which worked as a chemostat. However, force from the net flow drove bacteria toward outlet and eventually resulted in bacterial washout. Therefore, repeated peristaltic movement is crucial for maintaining steady-state density distribution of bacteria along the channel. The effective diffusion driven from peristaltic contraction pushed part of the bacteria even faster toward the outlet combing with the net flow, but also pushed part of them toward the inlet against the net flow. As a result, part of bacteria stayed in the channel in equilibrium despite the net flow. With experiments and theoretical simulations, this study provided a threshold value of flow rate and peristaltic frequency to reach a steady-state spatial profile of bacteria density, which can also be used to study the spatial density profile of cross-feeding community.

Chapter 4 summarizes the contributions of this dissertation, and discusses possible future works to understand more details relative to this study.

# CHAPTER 2

# THE AGGREGATION TEMPERATURE OF *E. COLI* DEPENDS ON THE THERMAL GRADIENTS

Thermotaxis is the temperature response of *Escherichia coli* toward temperature gradients by run and tumble phase. Previous studies have shown that the aggregation temperatures of *Escherichia coli* in nutrient-rich medium depended on the ratio of chemoreceptors, Tar/Tsr. However, temperature response toward large and linear temperature gradient has not been studied. Here, we report a series of thermotaxis experiments in *Escherichia coli* with different linear temperature gradients, ranging from ~8$^{o}$C/mm to 52$^{o}$C/mm. Experiment was conducted by microfluidic device made of polydimethylsiloxane (PDMS), with temperature gradient generated across 500 μm wide test channel (gradient channel). The results showed that the aggregation temperatures decreased monotonically as gradient became steeper.

## 2.1 Background

Motile bacteria are capable of sensing and responding to a variety of environmental cues. A paradigm for such responses is chemotaxis of *E. coli* in spatial gradients of soluble chemoattractants, a behavior guiding *E. coli* towards spatial regions with greater

concentrations of various nutrients and, hence, improved growth conditions. *E. coli* chemotaxis is physically achieved through a combination of smooth swimming and tumbling, which are tied to two different states of cellular flagellar motors. During smooth swimming streaks, a cell keeps swimming in a certain direction, whereas tumbling results in a change in the swimming direction. When a cell moves up the gradient of an attractant, the concentration of the attractant around the cell increases with time, making the intervals of smooth swimming longer and the tumbling events less frequent (2, 3). The resulting migration of a cell can be reasonably modeled by a biased random walk, with the bias being provided by the gradient of attractant and increasing with steepness of the gradient (4, 5). The frequency of tumbling is controlled through histidine kinase CheA, whose activity is inhibited when the concentration of attractant increases in time (6-8). CheA phosphorylates the response regulator CheY, which in its active phosphorylated state tends to induce tumbling. Dephosphorylation of CheY by the phosphatase CheZ, which is usually constitutively active, leads to smooth swimming.

The fact that chemotaxis of *E. coli* depends on temporal changes in the local concentration of attractant, as experienced by a moving cell, has greatly facilitated studies of the underlying molecular signaling networks. Cells are tethered to a substrate by a single flagellum, exposed to step-wise changes in the concentration attractant, and the resulting changes in the dynamics of rotation of the flagellum are monitored. In addition, *E. coli* cells have been immobilized on a substrates and their responses to step-wise changes of attractant have been monitored using Föster Resonance Energy Transfer (FRET) microscopy and fluorescently labeled CheY and CheZ, with a stronger FRET signal indicating a higher level of activity of CheY (9).

Other major types of directed migration of *E. coli* towards regions with better growth conditions are aerotaxis (oxygen taxis), pH-taxis, and thermotaxis that, respectively, occur in response to gradients of oxygen tension, pH, and temperature. Aerotaxis is similar to chemotaxis in gradients of nutrients in the sense that it is largely unidirectional, because both greater nutrient concentration and greater oxygen concentrations are usually beneficial. *E. coli* is repelled from oxygen concentrations above the atmospheric level of ~21% (10), but there is no clear evidence of repulsion from physiological levels of oxygen (11). Both pH-taxis and thermotaxis are essentially different, however. *E. coli* favor a near-neutral pH of ~7.5 and are repelled by excessively acidic or alkaline pH environments that are detrimental for *E. coli* growth (12, 13). The optimal temperature for *E. coli* growth is usually considered to be 35 - 40 °C. The *E. coli* growth rate in reach medium is very low below 10 °C, gradually increases to ~ 25% of the maximum at room temperature, reaches the maximum at 35 - 40 °C and precipitously drops above 42 °C to as little as 10% of the maximum at 47 °C and to nearly zero at 50 °C.

Given the pH preferences of *E. coli*, it is reasonable to assume that, if placed into a spatial gradient of pH, *E. coli* would aggregate at pH ~ 7.5. The FRET biosensor data on the responses of immobilized *E. coli* to stepwise changes in pH is suggestive of such aggregation. It has not been shown directly, however. There is direct evidence of aggregation of *Serratia marcescens*, another motile gram-negative bacteria, at intermediate pH in a spatial gradient of pH (14). Similarly, it is reasonable to assume that, if placed in a temperature gradient, *E. coli* would aggregate at 35 - 40 °C. The responses of tethered *E. coli* (in terms of changes in the direction of flagellum rotation) to short 3 °C positive pulses of the ambient temperature indicated that *E. coli* are thermophilic (warm-seeking) at

temperatures below 37 °C and cryophilic (cold-seeking) above 37 °C (15). This result suggests that in a temperature gradient, free-swimming *E. coli* should aggregate at ~ 37 °C.

Nevertheless, until recently (16) there has been no clear experimental evidence of aggregation of *E. coli* at an intermediate temperature in a gradient by means of thermotaxis, and studying *E. coli* thermotaxis has proved to be difficult in general. One of the reasons is that the two receptors that are commonly considered to be primarily responsible for temperature sensing in *E. coli*, Tsr and Tar (16 - 19), are methyl-accepting chemotaxis protein (MCP) chemoreceptors, which are most abundant in *E. coli*. Tsr and Tar have strong affinities to serine and aspartate, respectively, and are also sensitive to a variety of other chemoattractants. As a result, the response of Tsr and Tar to temperature changes strongly depends on the concentrations of serine and aspartate in the medium and can be completely suppressed or even reversed when the concentration of attractants is increased. At a given temperature and medium composition, the responses of the Tsr and Tar receptors to a temperature change may be opposite, and the outcome may be decided by the relative abundance of the two receptors. This relative abundance is generally variable, and, for *E. coli* grown in an exponential culture, the Tar/Tsr ratio has been reported to increase by as much as an order of magnitude between $OD_{600}$ of 0.1 and 0.5 (16, 20). Hence, the results on thermotaxis experiments depend on the stage of growth reached by cells used in the experiment, and to make the results consistent, it is essential to always grow and prepare cells in the same way. In addition, temperature sensitivity has also been reported for two other MCP receptors, Trg and Tap (21), as well as for Aer (22), which is primarily responsible for aerotaxis.

Another inherent difficulty in the studying of thermotaxis is that temperature has major effects on *E. coli* physiology, affecting their growth rate, metabolism, and respiration, as well the swimming speed, $v$, and the characteristic time between consecutive tumbling events, $\tau$ (23, 24). Therefore, when *E. coli* are exposed to a temperature gradient for a long time, especially in a nutrient-rich medium, their concentration distributions may become uneven due to different growth rates at different temperatures. Furthermore, spatial variations in the rates of consumption of nutrients and respiration, especially at high cell densities, may lead to gradients of chemoattractants and oxygen, causing chemotaxis and aerotaxis (25). To avoid or, at least, minimize these secondary effects for thermotaxis study, it is preferable to perform experiments at a small cell density, in a motility medium or minimal medium, and in a setup where thermotactic response can be measured within a short time interval.

In the absence of directional bias, the movement of *E. coli* can be modeled by diffusion with an effective coefficient $D \sim \tau v^2$ (4, 5). Hence, if *E. coli* are placed in a compartment with a size $w$, their spatial distribution is expected to reach a steady state after a time $t_d = w^2/2D = w^2/(2\tau v^2)$, which represents the maximal time scale reaching equilibrium. With directional bias in the environment with temperature gradient, the time scale might be shorter than $t_d$, but the bias is usually small and difficult to quantify. Therefore, if the readout of a thermotaxis assay is the shape of the steady-state spatial distribution of *E. coli* in a certain temperature gradient, a time scale $t_d$ should be allowed after the exposure of *E. coli* to the gradient, before reliable measurements of the steady-state distribution can be taken. Importantly, the time $t_d$ increases as $w^2$. With the characteristic values of $v$ and $\tau$ at ~20 μm/s and ~ 1 sec, respectively, the characteristic

value of $D$ is ~400 μm$^2$/s, corresponding to $t_d$ of ~2 min, ~20 min, and ~ 3 hrs for $w$ = 0.3, 1.0, and 3.0 mm, respectively. The time of 20 min is a physiological scale corresponding to the doubling time of *E. coli* in an optimal medium at 37 °C. Therefore, to minimize changes in *E. coli* physiology in a thermotaxis assay, with the readout in steady-state distribution in a temperature gradient, it is preferable to limit the size of the compartment with the gradient to $L$ < 1 mm.

In a number of studies on *E. coli* thermotaxis (23, 24-27), the temperature gradients was relatively shallow and spread over lengths on the order of 10 mm, which *E.coli* take larger time scale to migrate. On the other hand, experiments in those spatially extended gradients brought to light the phenomenon of pseudo-thermotaxis, which is the migration of bacteria in temperature gradients that is not directly related to their warm-seeking or cold-seeking behavior, but solely due to temperature dependence of the swimming speed, $v$, and time, $\tau$ (5, 23). When $v$ is position dependent, the steady-state local density of bacteria is expected to be proportional to 1/ $v$ (5). The variation of $v$ with temperature depends on composition of the medium. It can reach a factor of 2 between 20 and 40 °C and can lead to migration of *E. coli* towards higher or lower temperatures (23).

Thermotaxis-driven aggregation of *E. coli* at intermediate temperatures was recently reported by Yoney and Salman (16), who generated non-linear axisymmetric temperature gradients by heating water in a microchannel with an infrared (IR) laser. The gradients were much sharper than in the previous literature, with the temperature changing from 30 to 55 °C over 100 μm. The experiments were performed in a nutrient-rich M9CG medium at a cell density $OD_{600}$ ~ 0.3, and the aggregation temperature was reported to depend on the Tar/Tsr receptor ratio, which depends on the density the cells were grown to

in an exponential culture prior to the thermotaxis assay (16). However, there was no intermediate temperature aggregation observed for cells in motility medium, and the temperature aggregation in steep 1-D linear gradient was still unknown.

While our manuscript was prepared for publication, a detailed study of the *E. coli* thermotaxis published, which combined intracellular signaling experiments using FRET microscopy with step-wise changes in temperature in different media, mathematical modeling, and microfluidic experiments with an earlier version of the device used in our paper (28). This study was focused on the signal transduction through the Tsr and Tar receptors. The main conclusions of this study was that the thermotactic aggregation of *E. coli* at an intermediate temperature in a gradient requires the presence of both Tsr and Tar, which are largely interchangeable, and occurs when either one, but not both of the receptors, is stimulated with its specific chemoattractant, serine and aspartate, respectively. This study also suggested that thermotactic aggregation cannot occur in a motility buffer and in the absence of chemoattractants for Tsr and Tar, in general.

Microfluidic technologies have been successfully used to study bacterial chemotaxis (29). Notably, Kalinin *et al*. used microfluidic devices with microchannels casted in hydrogel to perform detailed studies of *E. coli* chemotaxis in a variety of well-defined linear gradients (30). The studies highlighted the large range of ambient concentrations of attractant, to which *E. coli* can adapt, and indicated that it is more appropriate to interpret *E. coli* chemotaxis as the sensing of fractional rather than absolute concentration changes. A conceptually new type of directed migration assay enabled by microfluidics is to continuously perfuse a suspension of swimming cells through a long channel with a gradient of a migration-eliciting factor applied across the channel (31). If

the cross-channel gradient does not change with the position along this gradient channel and the residence time of cells in it is longer than the diffusion time $w^2/2D$, where $w$ is the channel width, the cross-channel distribution of cells at the downstream end of the gradient channel is expected to represent their steady-state distribution in the gradient. An advantage of this approach is that the continuous perfusion makes it possible to collect data on large numbers of individual cells, with the data collection done continuously, without changing anything in the experimental setup.

This type of assay is difficult to implement for chemotaxis, because cross-channel gradients of the common chemoattractants are normally set at the beginning (upstream) of the gradient channel and gradually change along the channel due to molecular diffusion (31). On the other hand, the continuous flow assay was successfully implemented for aerotaxis (11). Stable linear cross-channel gradients of oxygen were generated by the diffusion of oxygen through the porous microfluidic device between two parallel gas-filled channels, which flanked the liquid-filled gradient channel with *E.coli* and functioned as a source and sink. A somewhat analogous approach was used to generate gradients of temperature in a microfluidic device, with the goal to study temperature dependence of protein conformations (32). Warm and cold water were circulated at relatively high rates through two large-cross-section parallel channels, which served as the source and sink of heat and created a near-linear gradient of temperature across the strip between them (Fig. 2.1) (32).

Here, we performed a series of experiments on *E.coli* thermotaxis in various linear gradients of temperature using a microfluidic device that combines elements from the devices of Ref. (32) and (11). Two parallel channels with hot and cold water flank a 500

μm test channel (gradient channel), generating a stable linear gradient of temperature across the test channel, where a suspension of *E. coli* is slowly perfused. A new element of the device is a cell motility filter (H-filter (33)), which is added upstream of the gradient channel and makes it possible to exclude non-motile cells from the thermotaxis assays. Importantly, experiments were performed in a motility medium (with glycerol as the energy source) and at a low cell density (OD ~ 0.03), and the value of $t_d$ (maximal equilibrium time) across the channel was only ~ 5 min. This experimental setup was designed to minimize the secondary chemotaxis effects, effects of the medium composition upon the thermal responses of the Tsr and Tar receptors, and long-term temperature-induced changes in the *E. coli* physiology. When the temperature gradients covered sufficiently broad ranges, we consistently observed distinct peaks in cross-channel distributions of *E.coli* density versus temperature, indicating aggregation at intermediate temperatures. To our surprise, however, as the gradients became sharper, the aggregation temperatures steadily decreased, from ~41 °C for a gradient of 26 °C/mm to as low as ~30 °C for 52 °C/mm.

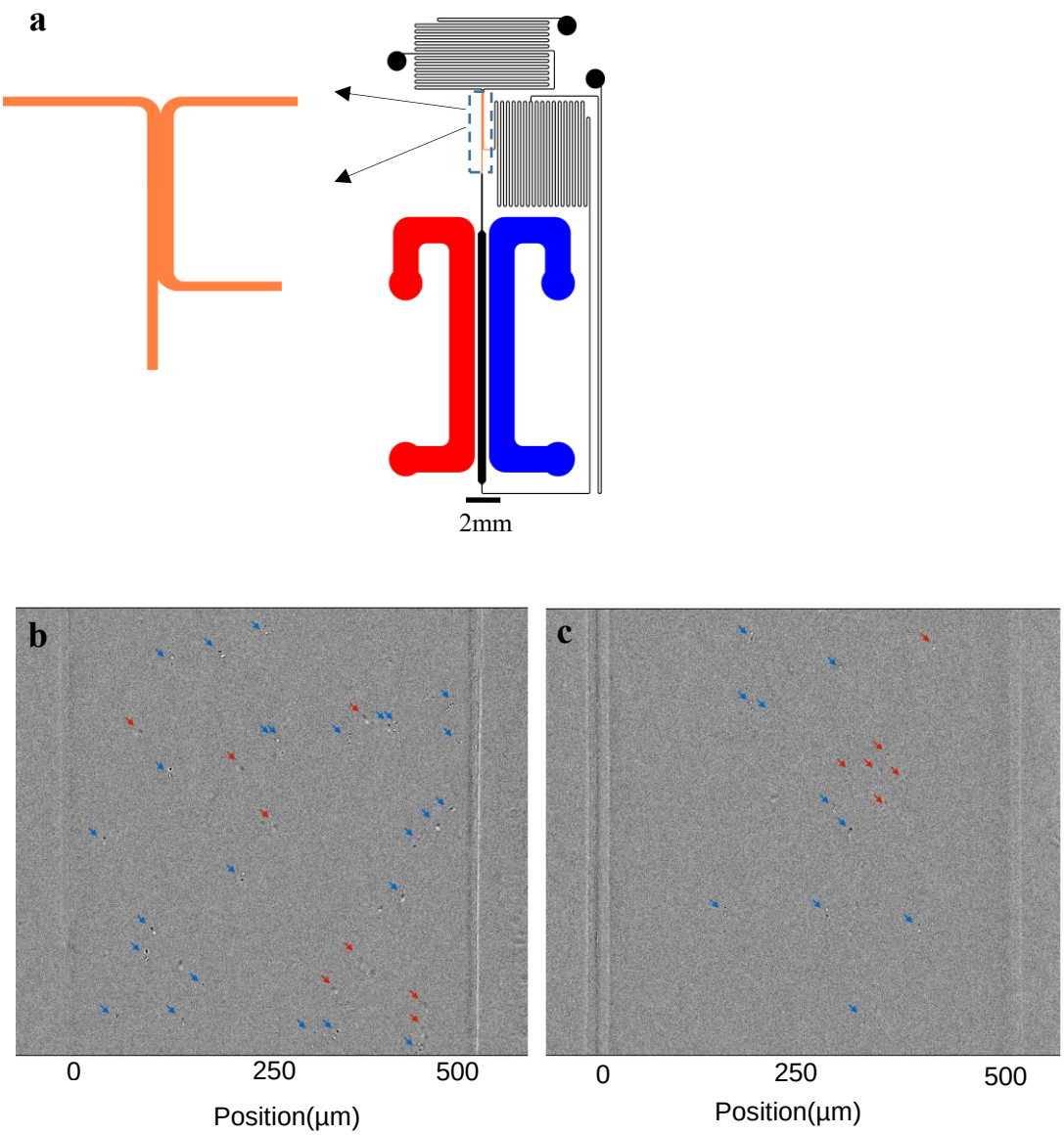


**Figure 2.1**: Microfluidic device with magnified h-filter. The device has a network of 100 μm microchannel (black, orange) and two 1mm deep side channels (red, blue). The 100 μm microchannel has one buffer inlet, one cell inlet, and one outlet. Flows from two inlets converge at the inlet of h-filter (orange). Cells with good motility had a chance to enter the main channel (gradient channel), which the gradient was generated by two 1mm deep side channels, and finally flowed out toward the outlet. (b): Micrograph of cell experiment near the entrance of gradient channel. The graph was the subtraction of two consecutive graphs in 133ms. Each pair of dark and white dots represents one cell, which dark dot is the second picture of consecutive graphs and white dot is the first one. Left side wall: 26°C, right side wall: 43°C. Blue arrows show the position of cells in focus, which matlab counted as cells, and red ones show cells out of focus, which were not counted. (c): Micrograph of cell experiment at downstream ( ~360 s from entrance). Left side wall: 26°C, right side wall: 43°C. The total amount of cell at downstream is less than the upstream due to sedimentation.

## 2.2 Materials and Methods

### 2.2.1 Bacterial Culture

Thermotaxis experiments were performed on an *E. coli* strain RP437. *E.coli* from a single colony in LB agar plate were grown overnight in TB (Tryptone broth, with 10 g Tryptone and 5 g NaCl added to 1 L of water and brought to pH = 7 with NaOH) with streptomycin at 34 °C. A 50 µL of the overnight culture was then added to 5 mL TB and grown to $OD_{600}$ of ~ 0.24 ± 0.02 (~2.5 hrs). Cells were washed three times and resuspended in a motility medium (10 mM potassium phosphate, 0.1 mM EDTA, 50mM glycerol and 1 uM L-methionine; pH 7.0) via centrifugation (3600 rpm, 11 mins). The final OD was adjusted to $OD_{600}$ ~ 0.1±0.01, and the suspension was immediately fed to the microfluidic device.

### 2.2.2 Microfluidic Setup

The microfluidic device used in the thermotaxis experiments (Fig. 2.1(a)) is made of a microfabricated monolith polydimethylsiloxane (PDMS) chip sealed with a #1.5 microscope cover glass. The device has a network of 100 µm deep microchannels and two separate 1 mm deep channels. The 100 µm deep microchannel network has two inlets (cell inlet and medium inlet), and a single outlet. The main element of this network is a rectilinear gradient channel, which has a length of 15 mm and a width $w$ = 500 µm and across which the temperature gradients are applied. The bacterial suspension is fed to cell inlet and is perfused through the gradient channel towards the outlet at a mean flow velocity $v_{fl} \approx 30$ µm/s. Along ~13.5 mm of its length, the gradient channel is flanked by two 1 mm deep channels, which are $d$ = 834 µm apart from each other (with 167 µm partitions

between them and the test channel) and are both 1.6 mm wide. The circulation of cold water, with a temperature $T_c$, through the 1 mm deep channel on the left, and hot water, with a temperature $T_h$, through the 1 mm channel on the right, creates a near-linear temperature profile across the gradient channel with a slope of ~ $(T_h - T_c)/d$. This technique of on-chip generation of a temperature gradient and this general layout of the device are adapted from a previous publication (32).

To account for the edge effects at the upstream and downstream ends of the gradient channel, we performed 3D numerical simulations of temperature distribution profiles in Comsol. The simulations indicated that the temperature gradient across the gradient channel remains unchanged (within the precision of the simulations or ~2%) along a gradient channel segment with a length $L$ = 12mm. The distribution of *E. coli* across the gradient channel is expected to reach a steady state after a time $t_d = w^2/2D = 310$ sec, where, as before, D ~ 400 μm$^2$/sec is the effective diffusion coefficient of motile *E. coli*. This time is shorter than the residence time of bacteria in the segment of the test channel with a constant temperature gradient, $t_{res} = L/v_{fl} = 400$ sec. Therefore, the distribution of *E. coli* across the gradient channel measured near its downstream end is expected to represent their steady-state distribution in the temperature gradient.

The flow through the 100 μm deep microchannel network is driven and controlled by the application of differential pressure between the two inlets and the outlet. To this end, the reservoirs connected to the inlets (modified 1.7 mL Eppendorf tubes) are pressurized with compressed air at ~ 14 kPa and the gradient channel is connected to the inlets and outlet through long and narrow (60 μm wide) resistance channels. The experimental setup and microfluidic device are conceptually similar to those that we previously used to study

aerotaxis of *E. coli* (11). However, the thermotaxis device has an additional element, an H-filter (33), which is a channel with a width $w_h$ = 150 μm and length $L_h$ = 3.5 mm located upstream of the test channel, serving to prevent non-motile *E. coli* from reaching the test channel. The left and right sides of the H-filter inlet (upstream end) are connected, respectively, to the medium and cell inlets of the device. At the outlet, the left and right sides of the H-filter channel are connected, respectively, to the test channel and the device outlet, with 1/3 of the stream directed towards the test channel and the remaining 2/3 directed towards the device outlet (through a dedicated bypass channel line; the 1:2 split is set by the resistance channel). Under normal operating conditions, the motility medium and bacterial suspension are fed to the H-filter inlet at flow rate ratios of ~1:1,controlled through the pressures at the two inlets. Hence, in the absence of bacterial motility and diffusion, the entire stream of the bacterial suspension is directed towards the bypass line and does not enter the test channel (Fig. 2.S1). The mean flow velocity in the H-filter channel is $v_h \approx 300$ μm/s, corresponding to a residence time $L_h/v_h = 12$ sec, which is comparable to the effective cross-channel diffusion time for motile *E. coli*, $w_h{}^2/2D = 28$ sec. Therefore, at the H-filter outlet, motile *E. coli* are broadly distributed across the channel, and a substantial portion of them enters the gradient channel. An estimate, ignoring the non-uniformity of the flow velocity over the channel cross-section, suggests that, when bacterial suspension and motility medium are fed to the H-filter at 1:1 ratio, no non-motile cells and as much as 30% of motile cells are directed towards the test channel. On the way between the outlet of the H-filter and the inlet of the test channel, motile *E. coli* then become nearly uniformly distributed across the channel width.

In addition to enabling the positive selection for motile *E. coli*, the H-filter also makes it possible to adjust the concentration of bacterial suspension in the test channel. When the flow rate ratio between the bacterial suspension and motility buffer at the H-filter inlet is reduced below 1:1, the concentration of *E. coli* in the test channel is reduced as well (nearly proportionally). As compared with the *E. coli* the suspension fed to cell inlet, the suspension in the test channel is normally diluted ~3-fold (as judged by counting individual *E. coli* in the field of view), corresponding to $OD_{600} \approx 0.03$. Another added benefit of the H-filter is the refreshment of the *E. coli* medium. As a result of the cross-channel diffusion of motile cells, >50% of the *E. coli* medium content is replaced with fresh motility medium as short as ~30 sec before the beginning of the thermotaxis assay, which is the time in flow between the outlet of the H-filer and the inlet of the test channel. The refreshment of the medium immediately before the thermotaxis assays, low concentration of *E. coli* in the medium, the absence of strong chemoattractants and rapidly metabolized nutrients in the medium, and the relatively short duration of the assays (~7 min), were expected to facilitate the establishment of well-defined, reproducible medium conditions during the thermotaxis assays.

### 2.2.3 Temperature control and video microscopy setup

The thermotaxis experiments were done on an inverted fluorescence microscope (Nikon TE2000) in an environmental enclosure. The temperature in the enclosure was set at $T_e$ = 34 °C, the same as the *E. coli* culture growth temperature, and to further standardize the experimental conditions, the reservoir with *E. coli* was placed inside the enclosure. In experiments with relatively steep temperature gradients, corresponding to large temperature differences between $T_h$ and $T_c$, the temperature at the middle of the test channel

(average between $T_h$ and $T_c$) was usually close to $T_e$. Therefore, the effect of the heat exchange between the microfluidic device and air beneath it upon the temperature profile in the test channel was minimal. To circulate cold and hot water through the two 1 mm deep circulation channels, we used two separate circulation water baths, which were set to different temperatures. The flow rates were ~2.0 mL/sec. To accurately assess the temperatures inside the circulation channels (deep side channels), the tubing lines connected to their inlets and outlets had in-line thermistors, which were placed at equal short distances from the inlets and outlets. The temperature in a circulation channel was calculated as the average between the temperature readings of the thermistors upstream of the inlet and downstream from the outlet (32). The largest difference between the upstream and downstream thermistors while $T_h$ = 67 °C was measured as 1.0 °C.

Micrographs of *E. coli* in the gradient channel were taken with a 20x/0.75 Nikon objective (1 mm working distance), 0.55x video coupler, and a 2/3" digital b/w CCD camera (Basler A102f) under oblique brightfield illumination. The field of view was 550 μm along the test channel and covered the entire width of the channel. The objective was focused at the midplane of the channel (50 μm from the bottom). To detect individual bacteria, two consecutive micrographs were taken with a short time interval (~133 ms). A certain constant value was then added to all pixels of the first micrograph, and the second micrograph was digitally subtracted from it. In the resulting image, regions without cells appeared as uniform grey background, whereas each cell produced a pair of a dark and bright spots at positions where the cell was located in the first and second micrographs (Fig. 2.1(b)(c)). Because of the motion of cells with the flow, these locations were on average ~4 μm apart along the flow direction, which is the product of the average flow velocity of

~30 μm/s and the 133 ms interval. The image was processed with a home-made code - im2bw, built in Matlab that used smoothing and thresholding to identify cells and their locations. Because of the relatively large depth of the gradient channel, the defects at the top and bottom of the channel (and bacteria stuck to the top and bottom) were very much out of focus and had very little effect on the uniform grey background. The pairs of micrographs were taken with an interval of $\Delta t = 5$ sec, corresponding to an ~150 μm average displacement along the flow, which is ~1/4 of the size of the field of view. However, within this interval, cells were expected to move a distance of as much as $\sqrt{2D\Delta t} = 60$ μm in the vertical direction, much greater than the depth of field of the video microscopy setup (< 5 μm). Therefore, a great majority of cells that were identified in the images were counted only once.

To visualize the temperature profile in the test channel at various $T_h$ and $T_c$, we used a 10 ppm solution of HPTS (8-Hydroxypyrene-1,3,6-trisulfonic acid) fluorescent dye in 50mM Tris (pH 7.6, 25$^o$C) buffer, which was perfused through the test channel at a low speed. The pH of Tris buffer decreases with temperature, and HPTS becomes less fluorescent as pH of the medium decreases, resulting in a reduction of fluorescence of the HPTS solution by as much as 1.7% per 1 $^o$C. Fluorescence microscopy was conducted with a standard GFP filter cube and with stable illumination derived from a 455 nm LED, with the 10x/0.25 objective focused at the gradient channel midplane. Fluorescence background resulting from the camera noise, incomplete blocking by the fluorescence filters, and residual autofluorescence was accounted for by taking micrographs of the test channel with plain buffer in it. Flat-field correction was performed by taking fluorescence micrographs of the gradient channel with the HPTS solution without temperature gradient applied and

fitting the cross-channel distribution of brightness with a polynomial. To be able to convert the local intensity of HTPS fluorescence in the gradient channel into local temperature, we measured cross-channel profiles of fluorescence at different spatially uniform temperatures. To this end, both circulation channels were connected to the same bath ($T_h = T_c$) that was consecutively set to 25, 30, 35, 40 and 45 $^{o}$C. The cross-channel fluorescence profiles were practically flat after the proper background subtraction and flat-field correction in an ~340 μm wide central region of the channel at all temperatures, which fluorescence profiles were distorted near the side walls. Due to the concentration gradient (Chap. 2.5.3; Fig. 2.S5(b)) generated by temperature gradient, which causes a molecular concentration gradient across 500 μm channel, the net fluorescence gradient was the combination of temperature-caused pH gradient and HPTS/Tris concentration gradient. To confirm such effect, we measured the concentration gradient by HPTS/Phosphate (pH 7.4 in 25 $^{o}$C), which the pH of phosphate buffer is much less sensitive to temperature change (0.025 pH difference from 25 to 37 $^{o}$C), comparing to Tris, and the resulting fluorescence gradient was mainly from molecular concentration gradient. Therefore, the temperature gradient profile was deduced by dividing the molecular concentration gradient from the net fluorescence gradient in temperature gradient (Fig. 2.2).

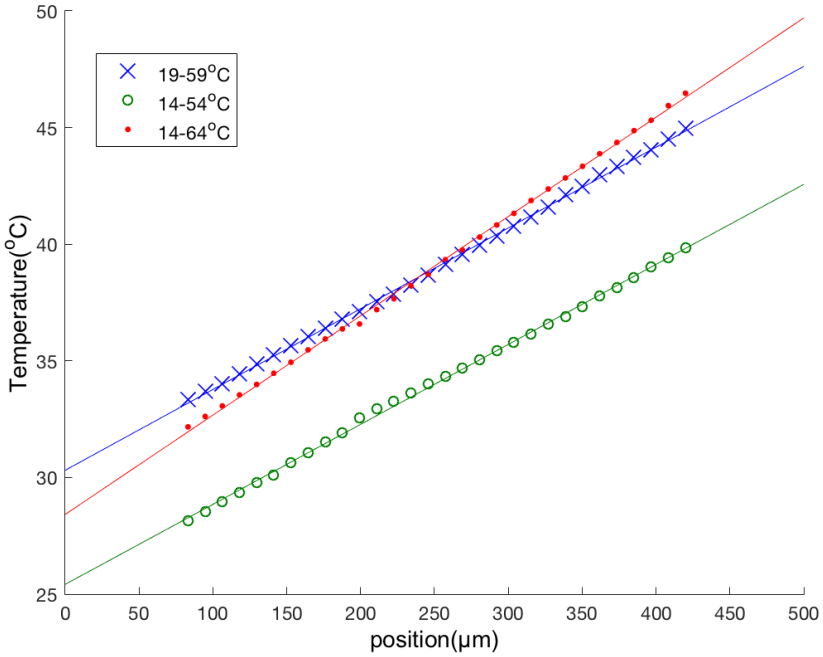


**Figure 2.2**: Fluorescence measurement of HPTS/Tris (pH 7.6, 25 °C). Three temperature gradients were measured. The result was corrected by dividing molecular concentration gradient from the fluorescent gradient (Fig. 2.S5(b)). All other temperature gradient profile were mathematically deduced from this measurement.

## 2.3 Results

Distributions of temperature across the gradient channel were measured for the $T_c$ and $T_h$ values of, respectively, 19 and 59 °C, 14 and 54 °C, and 14 and 64 °C (Fig. 2.2). In all cases, the temperature profiles in the 400 μm wide central region of the channel were nearly linear, with slopes, $\Delta T/\Delta x$, proportional to the difference $T_h - T_c$, $\Delta T/\Delta x = a(T_h - T_c)$, with the pre-factor $a = 0.87\ \mathrm{mm}^{-1}$, in a good agreement with the numerical simulation prediction of $a = 0.82\ \mathrm{mm}^{-1}$. Therefore, we adapted the formula $\Delta T/\Delta x = a(T_h - T_c)$ for calculation of temperature gradients in our thermotaxis experiments. In what follows, we report temperature gradients in terms of the temperature at the left wall and right walls of the gradient channel, $T_l$ and $T_r$, which are adjacent to the cold and hot

circulation channel, respectively. Based on our numerical simulations, we calculated these two temperatures as $T_l = 0.2825T_h + 0.7175T_c$ and $T_r = 0.7175T_h + 0.2825T_c$.

We first studied thermotaxis of *E. coli*, in two shallow temperature gradients with $\Delta T/\Delta x = 8$ ºC/mm, one with $T_l$ = 36 ºC and $T_r$ = 40 ºC and the other one with $T_l$ = 39 ºC and $T_r$ = 43 ºC (Fig. 2.3). The distributions of *E. coli* across the gradient channel were assessed at the downstream end of the channel (11mm from the beginning). The experiments were run for ~30 min after *E. coli* suspension was first fed into the microfluidic devices, with an average of 5000 cells analyzed per experiment. Each of the two experiments was performed three times ($N$ = 3) on three different sets. An obvious feature of both distributions is that they are relatively flat, with only ~2-fold difference between the highest and lowest cell densities across the gradient channel.

*E. coli* start showing cryophilic behavior in $T_l$ = 39 ºC and $T_r$ = 43 ºC. This reversal of behavior from thermophilic to cryophilic appears to be reasonable in view of the fact that the *E.coli* growth rate (in a rich medium) sharply drops at temperatures above ~ 43 ºC. It is also worth noting that there was no sign of aggregation of *E. coli* at any intermediate temperatures in either of these shallow gradients.

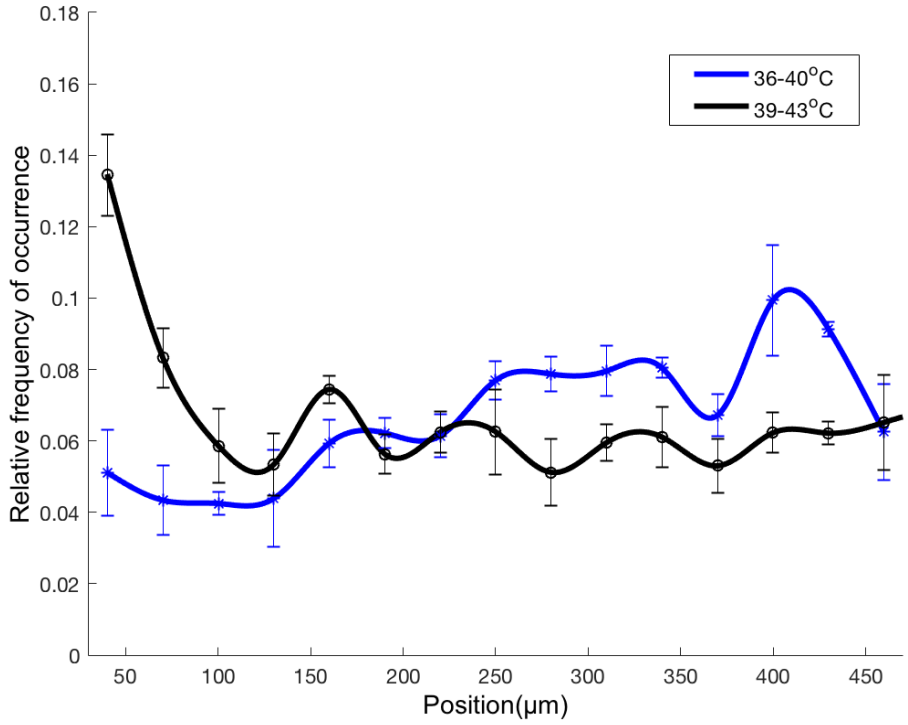


**Figure 2.3**: In shallow gradient (8 ºC/mm), *E.coli* showed thermophilic behavior in 36-40 ºC but cryophilic in 39-43 ºC. Errorbars showed SD of three independent experiments.

We then studied thermotaxis of *E. coli* in steeper temperature gradients, with temperature profiles in the gradient channel covering relatively broad ranges both below and above the putative aggregation temperature of 37 ºC. We performed four different experiments (with N = 3 repeats of each, as before) with the values of $T_l$ and $T_r$ of, respectively, 33 and 46 ºC, 31 and 48 ºC, 28 and 50 ºC, and 24 and 50 ºC (Fig. 2.4). The temperature gradients were $\Delta T/\Delta x = 26$, 34, 43, and 52 ºC/mm, respectively. The salient features of cross-channel distributions of *E. coli* in all of these experiments are well-pronounced single peaks and large ratios between the maximal and minimal local densities of cells, clearly showing that in these gradients, *E. coli* aggregate at certain intermediate temperatures. To our surprise, however, we found that the aggregation temperatures

(temperatures at the peaks of the distributions) are not identical for different gradients, but rather monotonically decrease, as the gradient becomes steeper, from peak ~ 41 $^{o}$C at $\Delta T/\Delta x = 6$ $^{o}$C/mm to 38 $^{o}$C at 34 $^{o}$C/mm, to 34 $^{o}$C at 43 $^{o}$C/mm, and to 30 $^{o}$C at 52 $^{o}$C/mm.

To verify that the aggregation in the temperature gradients is not a transient effect depending on the residence time in the gradient channel, $t_{res}$, we repeated the experiment with the steepest gradient, 24 - 50 $^{o}$C ($\Delta T/\Delta x = 52$ $^{o}$C/mm), while measuring the cross-channel distributions of *E. coli* at two different positions: near the end of the gradient channel (the regular position), with $t_{res}$ = 360 sec, and at 2/3 of the way from the beginning to near the end, with $t_{res}$ = 240 sec (Chap. 2.5.4). The two distributions (Fig. 2.S2) were similar, both having peaks at ~ 30 $^{o}$C, indicating that the aggregation around these temperatures is stable, once established, and persists for at least 120 sec. This experiment was performed only once, as a control, making the data more noisy than those in Fig. 2.4.

Next, we tested whether the aggregation temperature depends on the steepness of the gradient or on the entire range of temperatures that *E. coli* are presented with and are allowed to explore. To this end, we first performed another experiment with $\Delta T/\Delta x = 34$ $^{o}$C/mm, but with the interval $T_l$ - $T_r$ shifted by 5 $^{o}$C, from 31 - 48 $^{o}$C to 26 - 43 $^{o}$C (Chap. 2.5.4; Fig. 2.S3). When plotted in the coordinates of the frequency of occurrence (bacterial density) *vs.* temperature, the distributions of *E. coli* in both experiments had peaks around 37-38 $^{o}$C (Fig. 2.S3(b)). On the other hand, when the abscissa was changed to the distance from the left (cold) channel wall (Fig. 2.S3(a)), the two distributions had peaks as far as 100 μm apart (1/5 of the channel width). Next, we performed an additional experiment with $\Delta T/\Delta x = 43$ $^{o}$C/mm (Fig. 2.S3(c)(d)), but with the interval $T_l$ - $T_r$ shifted by 5 $^{o}$C, from 28 - 50 $^{o}$C to 23 - 45 $^{o}$C. Again, when plotted in the coordinates of the frequency of occurrence

*vs.* temperature, the distributions of *E. coli* in the two experiments had peaks at about the same temperature of 34 $^{o}$C (Fig. 2.S3(d)). On the other hand, when the abscissa was changed to the distance from the left channel wall (Fig. 2.S3(c)), the peaks of the two distributions were ~100 μm apart. It is worth noting, however, that there appears to be systematic shifts between the two distributions in Fig. 2.S3(b) and the two distributions in Fig. 2.S3(d) at temperatures away from their peaks. Conversely, the distributions in Fig. 2.S3(a) and Fig. 2.S3(c) somewhat converge towards the channel sidewalls, with bacterial densities tending to reach zero at the physical boundaries (channel walls) rather than at certain temperatures. The results of these two experiments indicate that the aggregation temperature of *E. coli* depends on the steepness of the gradient rather than the total range of temperatures that cells are allowed to explore. On the other hand, the detailed shape of the distribution of *E. coli* in a temperature gradient depends on the range of temperatures and region of space that cells are confined to.

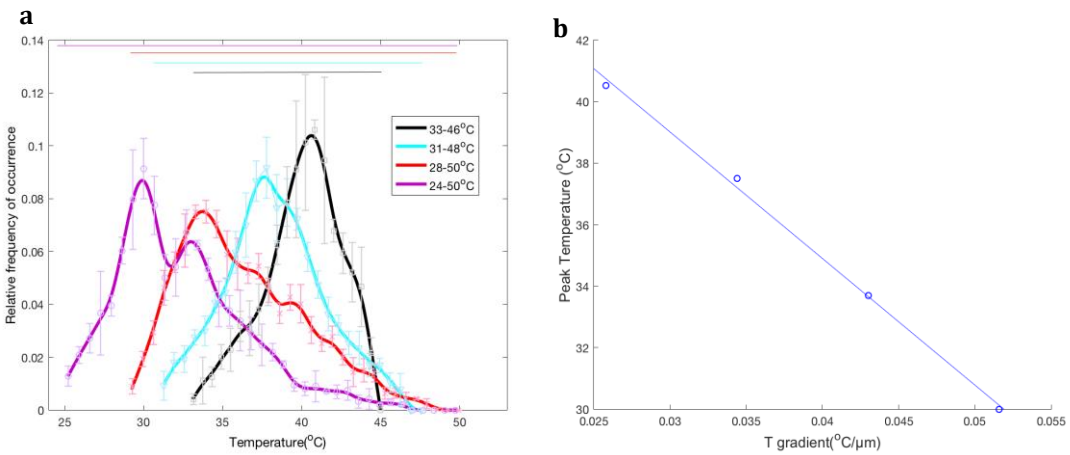


**Figure 2.4**: (a) *E.coli* distribution of relative frequency of occurrence with temperature in four temperature gradients, 33 and 46 ºC, 31 and 48 ºC, 28 and 50 ºC, and 24 and 50 ºC. Errorbars showed SD of three independent experiments. The horizontal bars on the top part of figure showed the range of actual channel (500um), and the color of each bar corresponds to the same color code of curves. (b) The peak temperature was defined by the temperature corresponding to the maximum value of relative frequency of occurrence in (a). A fitted linear relation between peak temperatures and temperature gradients was found within these four temperature gradients.

## 2.4 Discussion

We used a microfluidic device to study thermotaxis of *E. coli* in a variety of linear temperature gradients, which spanned nearly an order of magnitude in steepness, from 8 to 52 ºC/mm, and were all generated across the same 500 μm wide channel. The microfluidic device and experimental setup have a number of features that facilitate carrying out consistent, reproducible, and informative thermotaxis experiments. The arrangement with continuous flow of an *E. coli* suspension through a long channel with a cross-channel temperature gradient and with the assessment of the *E. coli* distribution at the channel end makes it possible to analyze a large number of cells per experiment (high throughput), even when the cell density is relatively low ($OD_{600}$ = 0.03). Low cell density leads to low rate of global changes in the medium composition caused by cellular metabolism and also minimizes cell-to-cell interactions mediated by the local consumption and secretion.

Because of the low cell density and high gas-permeability of the microfluidic chip made of PDMS, *E. coli* respiration is not expected to cause any substantial reduction in the oxygen tension in the gradient channel (34). To further reduce the effects of changes in the medium composition during the thermotaxis assays, we had *E. coli* suspended a motility medium without major chemoattractants or rapidly metabolized nutrients, with glycerol as the energy source. Our tests indicated that the growth rate of *E. coli* strain RP437 in this medium at 34 °C was 0.

Rapid circulation of temperature-controlled water through two parallel, closely spaced deep channels is a flexible and versatile way to generate temperature gradients. Temperature gradients in the gradient channels always have the same, near-linear shape. Both the steepness of the gradient and the range of temperatures that cells are presented with can be varied in broad ranges. In addition, they both are linear functions of the temperatures of the cold and hot water circulated through the two channels, $T_c$ and $T_h$. Hence, all parameters of the temperature gradients can be readily calculated from the measured values of $T_c$ and $T_h$, and the gradients do not need to be calibrated for each individual thermotaxis experiment. In addition, the temperature gradients in the test channel are largely one-dimensional, with relatively little temperature changes along the channel depth. Based on our numerical simulations, the gradient along the depth is always < 12% of the temperature variation along the same distance of 100 μm in the cross-channel direction. In low cell density, we believe that for the purposes of experiments on thermotaxis, this technique is able to achieve stable temperature gradient and high throughput with continuous flow.

The proposed experimental setup, with a relatively deep gradient channel, $h$ = 100 μm, also makes it easy to visualize and detect *E. coli* cells without fluorescent markers, by the subtraction of images taken with a short interval under brightfield illumination. Furthermore, we note that the ~18 sec time of passage of bacterial suspension flowing at 30 μm/sec through the 550 μm field of view of the video microscopy setup is longer than the characteristic time of the diffusion-like motion of *E. coli* along the channel depth, $h^2/2D = 12.5$ sec, making it possible to sample nearly all cells passing through the channel. Thus, the maximal number of sampled cells is not limited by the relatively small depth of field of the optical setup (~5 μm) and, at a given cell density, is proportional to the channel depth.

Another important feature of the experimental setup is the microfluidic H-filter (33) upstream of the test channel. This filter does not allow any non-motile *E. coli* to enter the gradient channel, thus improving the consistency and reproducibility of the thermotaxis experiments and increasing the visibility of the peaks of cell density. Notably, in all experiments with *E. coli* aggregation at intermediate temperatures, the ratios between the maximal and minimal cell densities were >10, (Fig. 2.4 and 2.S3). The H-filter also enables real-time adjustment of the concentration of *E. coli* in the test channel, and last, but not least, it exchanges >50% of the content of the medium to that of fresh motility medium as short as 30 sec before the beginning of the thermotaxis assay. This refreshment of the medium and its minimal nutrient content, the low concentration of *E. coli* in the medium, the oxygen-permeability of the device, and the relatively short duration of the assays (~ 6 min) all contribute towards the establishment of well-defined conditions during the thermotaxis assays.

The main results of our study are: thermotactic aggregation of *E. coli* in a motility medium at intermediate temperatures in temperature gradients, and the dependence of the aggregation temperatures on the steepness of the gradient and the range of temperatures that *E. coli* are presented with. Thermotactic aggregation of *E. coli* at intermediate temperatures was reported in two previous publications in nutrient-rich medium (16, 28). Nevertheless, none of them discovered the aggregation in pure motility medium with energy source. In Ref. (16) the case is made that the two receptors are essentially different and that Tsr always mediates thermophilic response, but loses its sensitivity at high temperatures, whereas Tar mediates thermophilic response at low temperatures and cryophilic response at high temperatures. Therefore, whereas the aggregation was only shown in a nutrient-rich medium (M9CG), it was also predicted to occur in motility media. In addition, due to the spatially dependent diffusion coefficient caused by temperature gradient (Chap. 2.5.3), molecular concentration gradient is generated by the temperature gradient, which turns out to be chemical gradient with strong chemoattractant existing in the medium. In this case, the aggregation resulted not only from thermotaxis but also chemotaxis. In order to study the effect, we measured the molecular concentration profile (Fig. 2.S5(b)) by measuring the fluorescence of HPTS/Phosphate across temperature gradient. The pH of phosphate buffer was relatively stable with temperature, with temperature coefficient ~ 0.003 (temperature coeff. of Tris ~ 0.03). Therefore, almost all the non-uniformity of fluorescence came from concentration gradient.

In contrast, the extensive data on the intracellular signaling in *E. coli* in response to step-wise changes in temperature in Ref. (28) indicate that the temperature responses of Tsr and Tar are surprisingly similar, both without chemoattractants and at equivalent

concentrations of serine and MeAsp. Based on this data, a detailed model is built, in which the inversion of the response of *E. coli* from thermophilic to cryophilic can only occur in the presence of either serine or aspartate (or MeAsp). However, the aggregation is not expected to occur in the absence of both chemoattractants or when they both are present at comparable concentrations (28).

Therefore, the observed aggregation of *E. coli* in a motiltiy medium at intermediate temperatures is a new result, which cannot be readily explained in the framework of the model from Ref. (28). It is worth noting, however, that glycerol is a known attractant of energy taxis for *E. coli* (35,36), which can sense glycerol concentrations as low as 1 μM (36). However, glycerol was still a relative desirable energy source in this study (Chap. 2.5.1). The second main result of the study, the temperature shift of the *E. coli* aggregation towards lower temperatures in steeper temperature gradients, is a surprising finding, for which we do not have any satisfactory explanation.

To clarify the mechanisms of thermotactic aggregation of *E. coli*, it would certainly be instructive to repeat the microfluidic experiments in the broad gradients (Fig. 2.4) under the conditions used in the intracellular signaling assays in Ref. (28): with *Δtsr* and *Δtar* mutants as well as with wild-type *E.coli* in a medium with either serine or MeAsp or with equivalent concentrations of the two attractants. We note that, if needed, an attractants can be added to the bacterial suspension at the inlet of the H-filter and its concentration will then become completely spatially uniform by the entry of the temperature gradient channel. The effect of serine was also tested in this study, and the resulting distribution supplied with 10 μM was shown in Figure 2.S7. As a result, the time of pre-incubation of *E. coli* cells in the medium with the attractant before the thermotaxis assay will be <1 min, thus

improving the control of the medium composition and maximizing the consistency experiments.

## 2.5 Supplemental Materials

### 2.5.1 Carbon source in motility medium

Without energy source, cells stopped swimming shortly after entering test channel and stayed at the hot side wall without moving (data not shown). Therefore, energy source was necessary for thermotaxis experiment, and glycerol was supplied in this study with the following reasons. First, tethered buffer supplied with 50mM glycerol was used by Paster and Ryu (15), who discovered inverse temperature response of *E.coli* with single cell experiment, suggesting that *E.coli* might aggregate at around 37$^{o}$C. Such concentration was below the reported chemotaxis threshold of *E.coli*, which was 100 mM (37). Consequently, the aggregation of *E.coli* was expected to be less affected by the existence of glycerol than other carbon sources. Although research (36) showed that glycerol induced energy taxis of *E.coli*, the mechanism involved in energy taxis required metabolism while chemotaxis and thermotaxis did not, which means that energy taxis would not directly affect chemotaxis and thermotaxis. In addition, study showed that glycerol is a chemorepellent with gradient 0.1 mM per mm (38), but another study showed that *E.coli* would not be repelled and move away from glycerol below 50 mM concentration, while gradient not shown (36). In consequence, the quantitative effect of glycerol in *E.coli* was still up in air. Though there were possible concerns in using glycerol, it was still less complicated comparing to other carbon sources. Research showed that lactate also induced energy taxis similar to glycerol, and *E.coli* chemotaxis toward glucose was significant (37). Moreover, glucose and lactate

stopped the synthesis of flagella in growth media while glycerol does not (39). Based on these above studies, we decided to use glycerol as energy source in thermotaxis study, in order to provide energy source without complicated confounding factors.

### 2.5.2 Revision of device

In an early version of the device, the test channel was 50 μm deep rather than 100 μm. Such shallower channel caused two problems. First, a large portion of cells was lost near the downstream of test channel due to cell sedimentation and sticking to the channel bottom. Second, imaging plane was close to the top and bottom of the test channel (25 μm from the bottom and top ceiling). Cells stuck to the top and bottom were visible, after two consecutive micrographs were subtracted (due to shaking of the whole device), making it difficult to automate the identification of moving cells with Matlab. Therefore, cell distributions were often unreliable in 50 μm deep channel.

### 2.5.3 Concentration gradient caused by temperature gradient

Temperature gradient across the test channel was measured by HPTS (8-Hydroxypyrene-1,3,6-trisulfonic acid trisodium) dye. HPTS fluorescence signal was indirectly related to temperature. It becomes less fluorescent as pH of medium decreases, and the pH of medium (Tris) decreases as temperature increases. However, temperature gradient could cause diffusion coefficient gradient (spatially dependence D), which resulted in non-uniform dye concentration in equilibrium (5). By the modified version of Fick's law, it claimed that concentration was inversely proportional to the square root of diffusion coefficient in equilibrium state, which $C_{(x1)}/C_{(x2)}=(D_{(x2)}/D_{(x1)})^{1/2}$. Diffusion coefficient is proportional to absolute temperature and inversely proportional to dynamic viscosity, which the viscosity differs with temperature. As a result, if temperature gradient

was zero (flat-temperature gradient), concentration was uniform across the channel. Through calculation, diffusion coefficient at 30°C ($D_{303K}$) is about 23% less than diffusion coefficient at 43°C ($D_{316K}$), which $D_{303K}=0.77*D_{315K}$. If such temperature gradient was generated, from 30°C (left wall) to 43°C (right wall), there would be ~13% of concentration difference across the 500 μm channel based on modified Fick's law. Consequently, the signal of HPTS across temperature gradient would be amplified by the molecular diffusion. Without taking such effect into consideration and measuring temperature gradient only by the slope of dye signals, the result of simulation was amplified by 30% (43% to 60% in test channel of total gradient), which was significant. In order to prevent such molecular drifting, the time scale between HPTS flowing into test channel and its distribution measurement should be short enough comparing to molecular diffusion time scale but long enough to reach thermal equilibrium, because thermal conduction is much faster than molecular diffusion. The equilibrium time scale was ~ 100 seconds for molecular diffusion and ~ 1 sec for thermal diffusion. To confirm the time reaching thermal equilibrium, we tested it by setting both side channels 45°C, while incubator temperature = 25°C (Fig. 2.S5(a)). HPTS dye solution would not start equilibrating with 45°C-side channels until entering test channel. Signal spatial profile was measured under different time intervals after entering test channel, for 5, 10, 20, and 40 seconds, to see if they reached equilibrium. The way setting the time was to apply 3 psi pressure difference between inlets and outlet to run the flow fast, and start counting time right after turning off the pressure difference. By applying 3 psi pressure difference, flow velocity was larger than 3mm/s in test channel, which was fast enough to count the time accurately right after turning off the pressure. The result showed that brightness between different time intervals are similar (with 0.25% error)

after 10 seconds. After measuring thermal equilibrium time, we measured the molecular diffusion equilibrium time scale by flowing HPTS/Phosphate (pH 7.4 in room temperature) solution in temperature gradient with Th=51 $^{o}$C, Tc = 21 $^{o}$C (Fig. 2.S5(b)). By simulation, 30$^{o}$C temperature difference between side channels gave ~12$^{o}$C temperature gradient across test channel. The pH of phosphate buffer was poorly sensitive to temperature, with only 0.025 pH difference between 25$^{o}$C and 37$^{o}$C. Therefore, the signal gradient across channel mostly reflected molecular diffusion. Signal spatial profile was measured the same way as thermal equilibrium test with different time intervals, 10, 20, 40, 80, 160, and 320 seconds. The slope of 320 s ($C_{0\ \mu m}/C_{500\ \mu m}$ = 7.63%) was 20 times steeper than the one of 10s ($C_{0\ \mu m}/C_{500\ \mu m}$ = 0.4%)), suggesting that molecular diffusion did amplify the slope of signal with poorly temperature sensitive buffer. Based on thermal and molecular diffusion equilibrium measurements, we chose 20 seconds intervals to calibrate HPTS/Tris brightness profile, and analyzed the data by dividing the spatial slope of HPTS by measured molecular concentration gradient as a background noise, which was 2% across 500 μm at 20 seconds. The resulting ratio of temperature gradient in channel to temperature difference between two side channels ($T_H$-$T_C$) was 43%, similar to simulation result.

### 2.5.4 Characterization of flow and cell distribution test

To verify whether it was laminar flow or turbulence flow, the distribution of fluorescence beads (0.5μm radius) across temperature gradient (34$^{o}$C/mm) was tested. The result showed a slight increase of beads count with increasing temperature (Fig. 2.S6(a)). To see if this increment was significant, we reduced the fluctuation by averaging the beads count (relative frequency of occurrence) in every 94μm interval, and the distribution showed 33% difference between the maximum and minimum relative frequency of

occurrence(Fig. 2.S6(b)), which was not significant comparing to the result of cell distribution in the same temperature gradient (Fig. 2.4, 31-48$^{o}$C).

In order to test if cell distribution depends on the residence time in T gradient, cross-channel distribution at 2 different position: near the end of test channel with residence time ~ 360 sec, and 2/3 of the distance from the beginning to near the end with residence time ~ 240 sec, was measured (Fig. 2.S2(a)). The measurement was conducted in the same experiment set (Set 1). The results of distribution in two different residence time were similar, peaking around 30 $^{o}$C. This means that cell aggregation was stable and persisted for at least 120 sec. The cell distribution versus temperature was measured again in residence time 360 sec and 720 sec in another experimental set (Set 2). As Fig 2.S2 (b), the distribution at 720 sec is not as sharp as the one at 360 sec. To quantitatively analyze the sharpness of peak, we applied similar idea as the full width at half maximum (FWHM) of distribution, which was used in Q factor to analyze the bandwidth, and compared it to the the test with residence time 240 sec and 360 sec (Set 1, Fig. 2.S2(a)). In addition to the half maximum, we calculated the full width at 70% maximum. Larger full width represented shallower peak. Moreover, the kurtosis was calculated to analyze the sharpness of each distribution, comparing to normal distribution which the kurtosis is 0. Positive and larger kurtosis means sharper peak comparing to normal distribution, and negative means shallower peak comparing to normal distribution. The results were shown as (table 2.1). It is not obvious to see the difference of FWHM between each distribution. However, by comparing the full width at 70% maximum, the bandwidth of the distribution of 720 sec was significantly larger than the others. In addition, all of the distributions showed positive kurtosis except the 720 sec one. Therefore, we concluded that the peak of cell distribution

versus temperature became shallower in 720 sec residence time comparing to the distribution of 240 sec and 360 sec residence time. To observe the favored temperature of *E.coli*, cell distribution with sharp peak was relatively more suitable for this study. Based on these statistical results, we chose 360 sec as residence time for thermotaxis experiments.

To test cell distributions in gradients with the same steepness but different temperature ranges, we measured the distribution across temperature gradients with the same steepness of gradient but different temperature (Fig. 2.S3). The aggregation temperature (peak) of each distribution in Fig. 2.S3(b) was nearly independent of the temperature range (~1.5$^{o}$C discrepancy), but the shape of the distribution changes with the range versus temperature (systematic shift). The possible reason for the systematic shift in might be wall effect. In 26$^{o}$C-43$^{o}$C, the peak (~300 μm) is closer to the right side wall, meaning that once cells hit the right side wall, the time that they needed to reach back toward the peak was shorter. In comparison, the distance from peak to left side wall was larger, which means that cells needed more time running back toward the peak once they hit the left side wall. Thus, a slight aggregation in the left part of test channel was caused. In converse, in 31$^{o}$C-48$^{o}$C experiment, peak is closer to the left side (~200 μm). Therefore, there would be slightly less cells between the left side wall and center, comparing to the 26$^{o}$C-43$^{o}$C distribution. Similar situation in Fig. 2.S3(d), two peaks differed by ~1$^{o}$C, which was closer to the one in Fig 2.S3(b). Same reason as before, two peaks were now both closer to left side wall, so the wall effect affected them similarly. If shifting temperature to 10$^{o}$C (Fig. 2.S4), unlike Fig. 2.S3, cell distribution did not shift that much comparing to temperature shift. One possible reason is that the lowest temperature under

18°C-40°C is too low, so that cells didn't respond normally. That might be the reason why the peak in 18°C-40°C is not as sharp as the one in 28°C-50°C.

### 2.5.5 Supplementary Figures

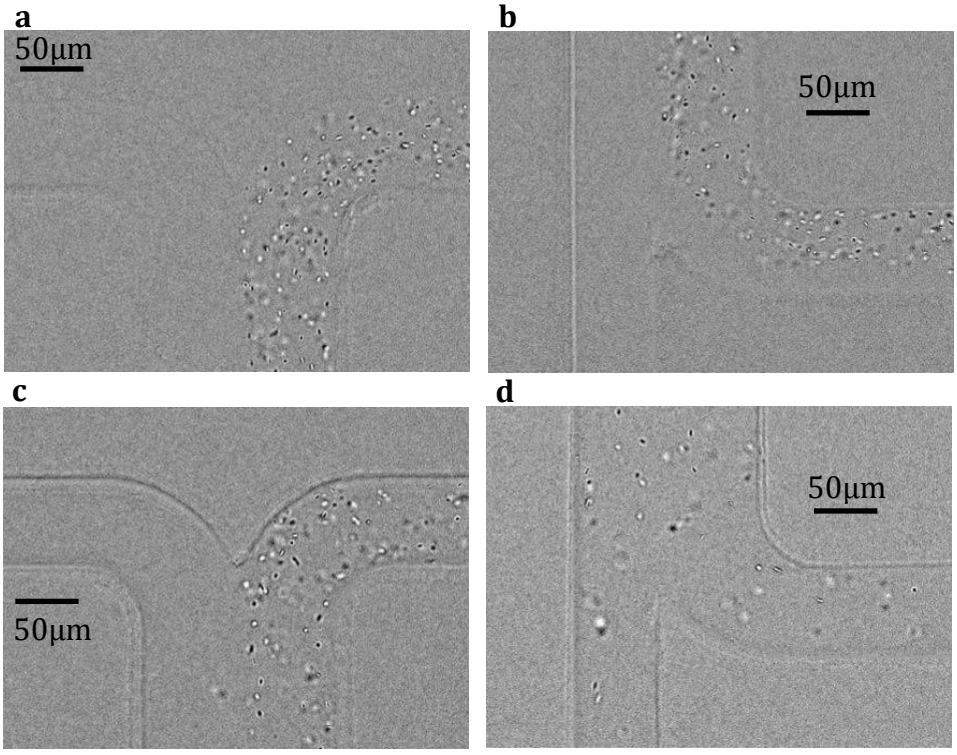


**Figure 2.S1**: h-fliter function (a) and (b) show cells with bad motility. (a) Upstream of h-filter, with buffer flowing from left side and immotile cells flowing from right side. (b) Downstream of h-filter. Immotile cells all flowed toward outlet(right side). None of the cells flowed downside toward test channel. (c) and (d) are cells with good motility. (c) Upstream of h-filter, with buffer flowing from left side and motile cells flowing from right side. (d) Downstream of h-filter. There are some motile cells (~1/3) flowing downside toward test channel.

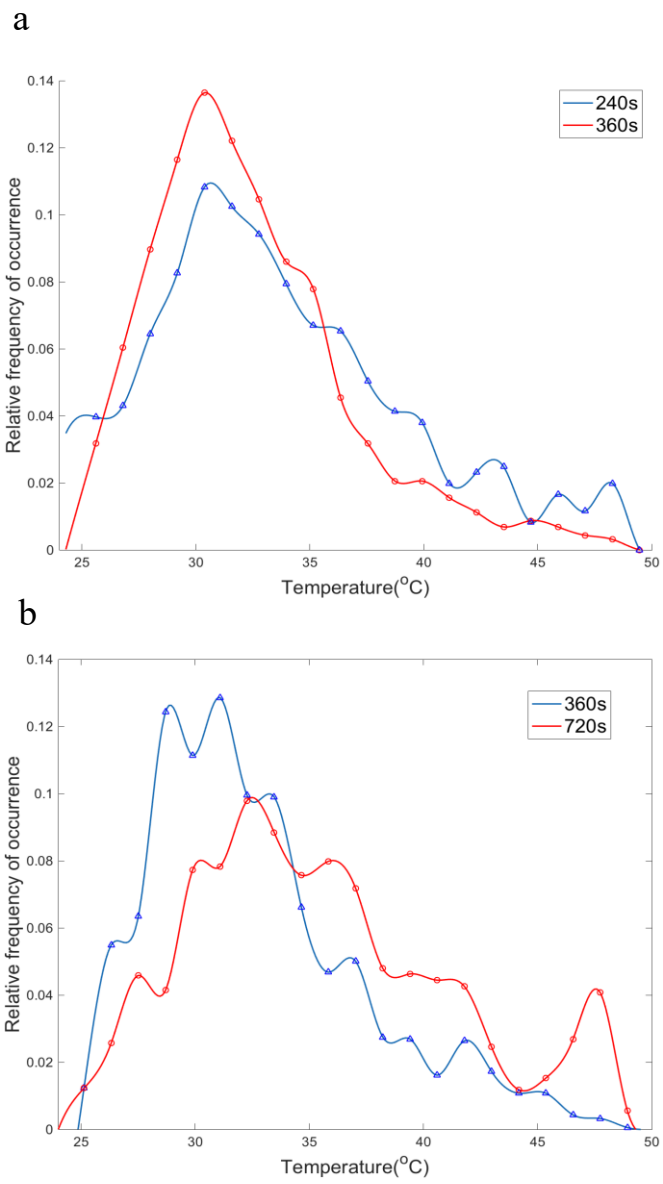


**Figure 2.S2**: Cell distributions were measured at different position along the test channel, which represents different time intervals for them staying in temperature gradient. (a) Set 1. Measurement of cross-channel distribution at 2 different position, with residence time 240 sec (blue) and 360 sec (red) respectively. (b) Set 2. Measurement of cross-channel distribution at 2 different position, with residence time 360 sec (blue) and 720 sec (red) respectively.

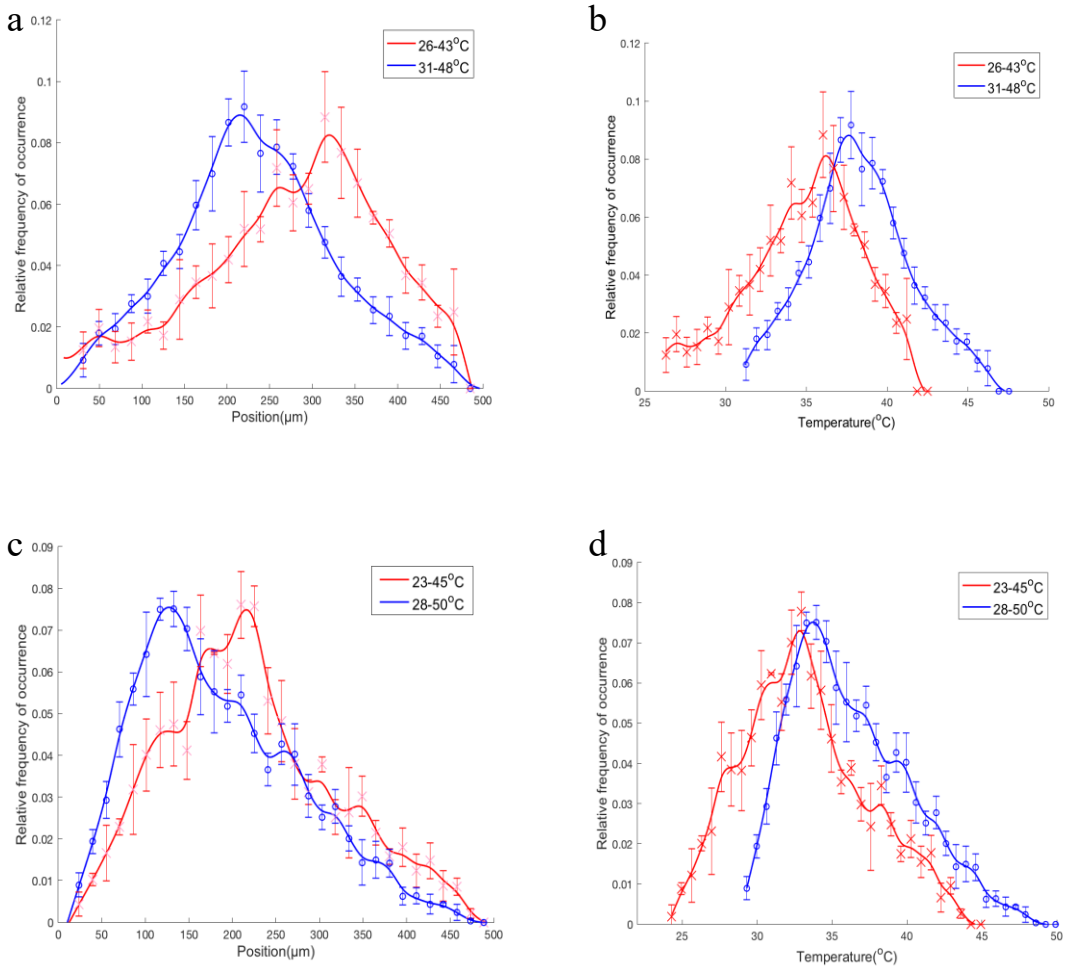


**Figure 2.S3**: Temperature gradients were shifted in order to compare distribution curve with different temperature ranges under the same gradient. (a)(b)Temperatures of hot and cold circulators was shifted from 59ºC-19ºC to 54ºC-14ºC, which corresponded to 31ºC-48ºC and 26ºC-43ºC in test channel. (a) shows that the peak shifted from position ~ 200 μm to 300 μm, with temperature shifting from 31ºC-48ºC to 26ºC-43ºC. (c)(d), distribution with x-position shifted with temperature gradient changing from 64ºC-14ºC to 59ºC-9ºC, which corresponded to 28ºC-50ºC and 23ºC-45ºC in test channel.

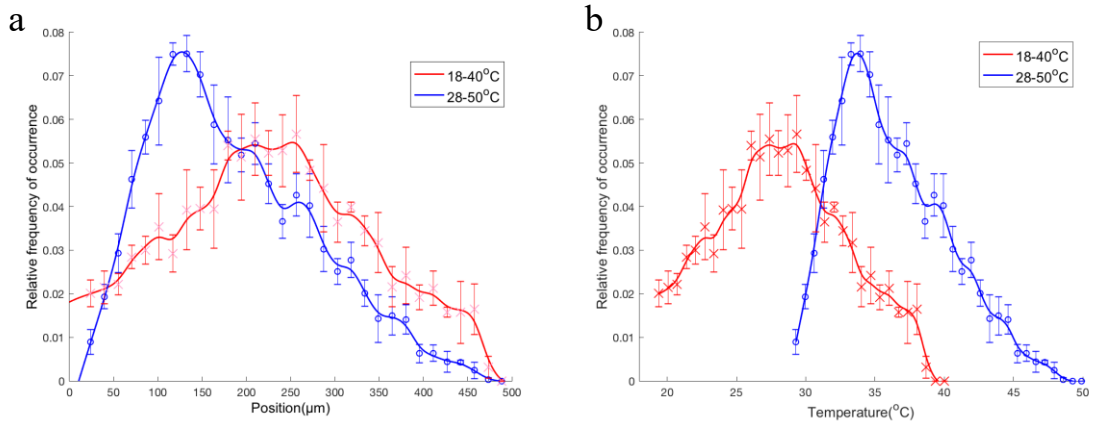


**Figure 2.S4** Temperature gradient was shifted by 10ºC in the steepness of 22 ºC/500 μm, from 28ºC-50ºC and 18ºC-40ºC inside test channel.

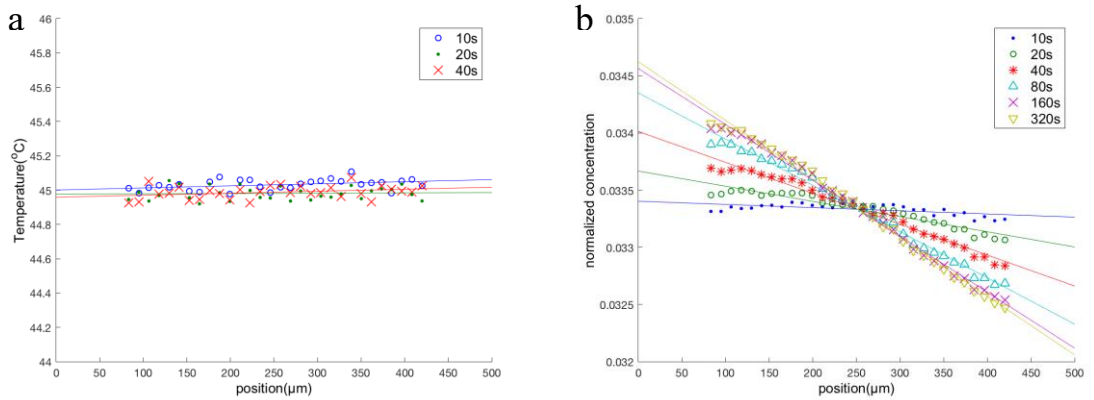


**Figure 2.S5:** (a) Temperature equilibrium test with HPTS/Tris. The temperature distribution along position with different time imterval. (b) Molecular diffusion test. Molecular concentration measured by HPTS/Phosphate was tested with different time interval in temperature gradient.

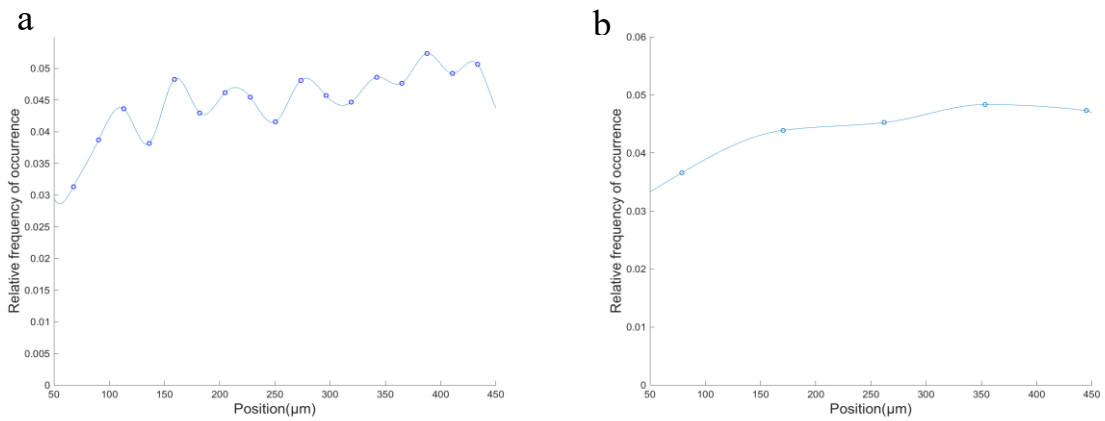


**Figure 2.S6:** (a) Distribution of beads across temperature gradient (34ºC/mm), versus position between 50μm and 450μm. b) Distribution of beads across temperature gradient by averaging the beads count (relative frequency of occurrence) from (a) in every 94μm to reduce the fluctuation data in (a).

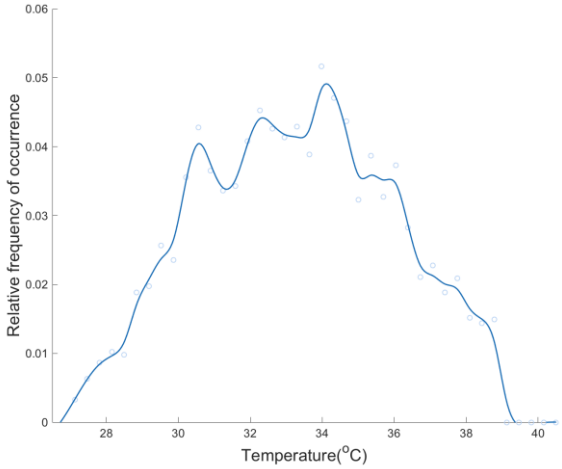


**Figure 2.S7:** Cell distribution versus temperature with 10 μM serine added. The temperature gradient in this experiment was 26ºC/mm. The aggregation temperature in temperature gradient 26ºC/mm shifted from above 40ºC (Fig. 2.4(a)) black curve, motility medium without serine) to 32~34ºC.

### 2.5.6 Supplementary Tables

| | 240s(set 1) | 360s(set 1) | 360s(set 2) | 720s(set 2) |
|---|---|---|---|---|
| FWHM(°C) | 9.59 | 8.41 | 7.30 | 9.17 |
| FW at 70% maximum(°C) | 5.24 | 5.04 | 5.82 | 7.59 |
| Kurtosis | 0.0351 | 1.1667 | 0.4353 | -0.4016 |
| Peak Temperature(°C) | 30.62 | 30.38 | 29.95 | 32.6 |

**Table 2.1:** Statistical result between distributions at different residence time. Full width at half maximum, full width at 70% maximum, kurtosis, and peak temperature of each distribution were shown.

## Acknowledgements

Chapter 2 covers the materials from the manuscript “The Aggregation Temperature of *E.coli* Depends on the Steepness of Thermal Gradient” by Chih-Yu Yang, Michael Erickstad, Jérôme Wong Ng, Edgar Gutierrez, and Alex Groisman. The manuscript was completed and ready to be submitted to *Biophysical Journal*. The dissertation author was the first author of the manuscript.

# CHAPTER 3

# THE EFFECT OF FLOW AND PERISTALTIC MIXING ON BACTERIAL GROWTH IN A GUT-LIKE CHANNEL

The ecology of microbes in the gut has been shown to play important roles in the health of the host. To better understand microbial growth and population dynamics in the proximal colon, the primary region of bacterial growth in the gut, we built and applied a fluidic channel that we call the mini-gut. This is a channel with an array of membrane valves along its length allowing to mimic active contractions of the colonic wall. Repeated contraction is shown to be crucial in maintaining a steady-state bacterial population in the device in spite of strong flow along the channel that would otherwise cause bacterial washout. Depending on the flow rate and the frequency of contractions, the bacterial density profile exhibits varying spatial dependencies. For a synthetic cross-feeding community, the species abundance ratio is also strongly affected by mixing and flow along the length of the device. Complex mixing dynamics due to contractions is described well by an effective diffusion term. Bacterial dynamics is captured by a simple reaction-diffusion model without adjustable parameters. Our results suggest that flow and mixing play a major role in shaping the microbiota of the colon.

## 3.1 Background

The large intestine of vertebrates harbors vast amounts of bacteria. The importance of this gut microbiota to the health of the host has been a topic of intense recent interest. The composition and function of this complex microbial community have been shown to have a strong influence on host physiology and affect pathological conditions as diverse as cancer (41), inflammatory bowel diseases (42), intestinal infections (43), malaria (44), autism (45), and obesity (46). Many of the connections between the pathologies and microbiota have been found by using fecal samples as a proxy for the content of the gut, and much effort has been invested in characterizing the composition of the microbiota with sequencing of bacterial genomes in fecal samples (47, 48). It is also known that bacterial composition show spatial variation along the human gut in healthy and diseased subjects (49, 50, 51).

To better understand the spatiotemporal composition of the gut microbiota and how it is formed, it is important to analyze and understand the different physiological conditions and the resulting physical forces affecting bacterial growth dynamics in the colon and how these conditions change with time and space. One obvious feature of these dynamics is the movement of luminal content down the colon. In adult humans, this movement has a mean velocity of approximately 20 μm/s in the proximal colon, the prime site of bacterial fermentation (see SI for velocity estimation). Importantly, the inflow to the colon from the small intestine has very low bacterial content (52, 53). Therefore, the movement down the colon alone can be expected to rapidly deplete bacterial density in the lumen of the proximal colon (even if the bacteria have high growth rates), a situation we refer to as

"washout" (Fig. 3.1A). In the real colon, different factors might counter-act this washout. One possibility would be active swimming of bacteria (Fig. 3.1B). However, while some bacteria in the colon may be motile (54), many abundant members of the gut microbiota do not carry genes for flagella (e.g. B. thetaiotaomicron, B. ovatus, F. prausnitzii (57). Correspondingly, flagellin, the main protein of flagella, is not strongly expressed in the colon (55) and flagellar activity might even be actively disrupted by the host (56). Furthermore, effective countering of the movement of the luminal content would require persistent swimming of the bacteria up the colon at a speed on the order of 20 μm/s, which is unrealistic. Another possible mechanism preventing washout would be replenishment of the lumen microbiota by bacteria shed from a bacterial reservoir adhering to the mucus layer and the epithelium on the colon walls (or "wall growth", Fig. 3.1C) (58-60). However, for realistic bacterial growth rates, simple estimates indicate that a proper replenishment would require the number of wall-bound bacteria to be comparable to that of bacteria in the lumen, whereas the observed abundance of the wall-bound bacteria is several orders of magnitude lower (see Supplementary Text). Further, oxygen levels are still high in the mucus layer but very low in the lumen (61). Given that most bacteria in the lumen are strict anaerobes, they can hardly grow within the mucus layer(62, 61). Correspondingly, the composition of the bacterial community inhabiting the mucus layer is very different compared to that in the lumen (51, 61, 63, 64). Thus, while all these proposed mechanisms to maintain bacterial densities observed in the colonic lumen probably play a role, we argue that they are not sufficient, even if combined, to explain the high bacterial density observed.

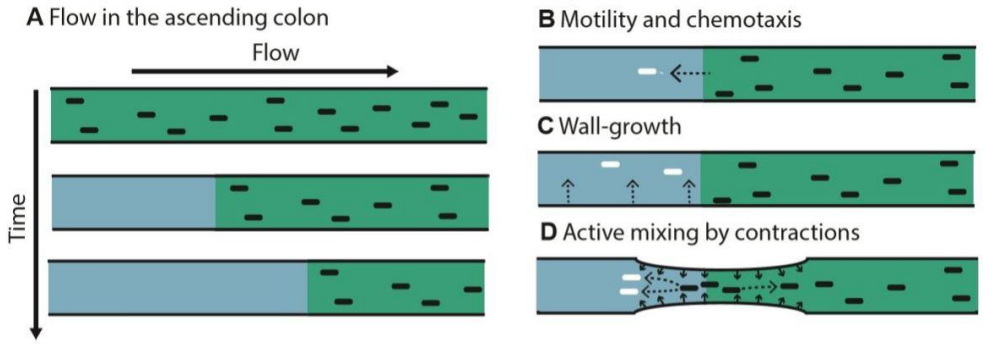


**Figure 3.1.** Washout by flow and possible counteracting factors. (A) Flow alone leads to emptying of channel content over time. Additional factors are required to counteract this 'washout' and help to maintain a stable bacterial density over time. Such factors may include: (B) Active motility by bacteria to swim towards the nutrient source; (C) Wall-growth; (D) Peristaltic mixing, with backflow generated by contractions of colonic walls.

In this work, we investigate another mechanism which might be essential for preventing washout: contractions of the intestinal walls. For the human colon, these contractions include relatively frequent but uncorrelated contractions in the proximal colon as well as less frequent but more coordinated peristaltic movements along the whole colon (65). Importantly, these contractions can lead to a mixing of luminal content, here referred to as "peristaltic mixing". Due to this mixing, some volume elements are displaced against the main flow-direction (backflow), as illustrated in Fig. 3.1D. Simple simulation of the hydrodynamic flow indicated that local movement of the luminal content up the colon coupled with bacterial growth can prevent the washout and generate a steady state with a high-density bacterial population under large-scale movement of the luminal content down the colon, see Fig. 3.S1. There have been multiples studies of the gut microbiota using various in vitro setups and flow systems. Early studies have focused on the effect of chemical composition of the medium, for example employing a 3-stage chemostat setup (66). Over time, this approach has become increasingly advanced, with more robust cell seeding and automated control, (67-69). To mix the medium and emulate the intestinal

contractions, peristaltic contractions of the walls were used; but these setups can be view as chains of discrete compartments, without the possibility to study continuous spatial structure (70). A continuous flow system involving differential water and acid uptake from a flexible tube has also been developed (71); however, wall contraction and mixing were not implemented there. Peristaltic-like perturbations have also been recently used in microfluidic gut-on-chip devices (72, 73, 74); however, the perturbations studied were of small amplitudes, mainly designed to stretch and stimulate epithelial cells. To study the role of wall contractions and mixing for bacterial growth, we built and tested a new laboratory model of the large intestine, the mini-gut. The mini-gut differs from the in vitro gut-like devices discussed above by emulating wall-contractions with an array of flexible membrane valves evenly spread along the length of the channel. Longitudinal flow rate as well as the amplitude and timing of contractions of different valves are adjusted and controlled separately. We studied the dynamics of bacterial growth in the mini-gut device at different medium perfusion velocities with periodic contractions of the valves generating a peristalsis wave. Confocal microscopy was used to observe bacterial growth dynamics continuously over space and time. Several distinct regimes are observed: the washout regime (with near-zero bacterial density), the chemostat regime (with near uniform density), and a third regime where the steady-state distribution of bacteria exhibited spatially varying density along the channel. We then characterized the dynamics of an engineered bacterial community of two cross-feeding strains in the mini-gut and observed distinct spatial dependence of bacterial composition. Our results establish that growth dynamics in the device can be effectively modeled by a reaction-diffusion system, with the complex mixing

dynamics due to channel contractions described by a simple diffusion term. The model effectively captures the experimental results without freely adjustable parameters.

## 3.2 Results

### 3.2.1 Model and Analysis

To study the role of flow and mixing on bacterial growth, we first develop a mathematical model. We consider growth occurring in a tube geometry of length L, with x denoting the position along the tube. Nutrient (but not bacteria) enters the tube at x=0, and the culture (medium and bacteria) exits at x=L. The rate of flow is constant along the tube, denoted by v. Mixing generated by the contraction of the channel is modeled by an effective diffusion coefficient, D (eddy diffusivity). A more detailed hydrodynamic model taking flow-vortices and laminar flow-profiles into account leads to similar predictions regarding growth and washout; see SI and Fig. 3.S1. We explicitly model the dynamics of bacterial density ρ(x,t) and nutrient concentration n(x,t) over time t with reaction-diffusion equations. With that, the model shares similarities with previous description of growing populations under constant influence of convection (wind, water-flow, etc.), see e.g. (75, 76). The equations for density and nutrients are given by:

$$\frac{\partial \rho}{\partial t} = D\frac{\partial^2 \rho}{\partial x^2} - v \cdot \frac{\partial \rho}{\partial x} + \lambda(n) \cdot \rho \qquad (1)$$

$$\frac{\partial n}{\partial t} = D\frac{\partial^2 n}{\partial x^2} - v \cdot \frac{\partial n}{\partial x} - \lambda(n) \cdot \rho / Y \qquad (2)$$

.

Here, flow is described by a convection term with flow-velocity $v$. Bacterial growth follows Monod kinetics, given by a nutrient-dependent growth rate $\lambda(n) = \lambda_0 \cdot n/(K_M +$

$n$), with the Monod constant being $K_M$, and the maximum growth rate in the medium being $\lambda_0$ (77). The yield $Y$ gives the conversion factor between nutrient concentration and bacterial density. Boundary conditions ensure a constant inflow of nutrients with concentration $n_{in}$ at $x = 0$, and a constant outflow at $x = L$; see SI.

We explored the criterion for washout, i.e., the disappearance of a stable culture ($\rho \to 0$) in the long-time limit ($t \to \infty$), by solving Eqs. (1) and (2) numerically starting with a uniform initial bacteria density. The effect of flow and mixing was studied by varying $v$ and $D$, using growth and yield parameters that we measured (Supplementary Table S1). The results are shown in Fig. 3.2A for fixed $L$ and $\lambda_0$, by plotting the spatially averaged bacterial density ($\bar{\rho}$) obtained in the long-time limit for different $v$ and $D$. We see that high density is attained for low flow and strong mixing, whereas in the opposite limits of high flow or weak mixing, bacterial density vanishes, indicating washout.

The nature of the parameter dependence can be understood qualitatively by a simple consideration (see Box 1 for more details). There are two important dimensionless parameters, the ratio of the diffusive mixing length, $\ell \equiv D/v$ , to the channel length, $L$, i.e, $\ell/L$, and the ratio of local dilution rate, $v^2/D$, to growth rate $\lambda_0$, i.e., $\alpha \equiv v^2/(D\lambda_0)$. The entire channel may be regarded as a well-mixed chemostat if $\ell/L \gtrsim 1$, i.e., above the dashed cyan line in Box 1. There, washout occurs if the flow rate exceeds a critical value $v^* = \lambda_0 \cdot L$ (dashed white line in Box 1). In the opposite regime, where $\ell/L \ll 1$ (below the dashed cyan line in Box 1), the channel is a chain of locally mixed regions (of lengths $\ell$). Spatially varying density profiles are expected in this case for $\alpha \lesssim 1$ (teal region in between the dashed red and cyan lines). Washout occurs to the right of the dashed red line.

We compared this qualitative picture to the numerical solution of Eqs. (1) and (2). From the results shown in Fig. 3.2A, we defined a washout condition, the combination of $v$ and $D$ values where the average density drops to zero for long times; see the solid white line in Fig. 3.2A. This white line is reasonably well captured by the condition $\alpha = 1.8$, shown as the dashed red line. Note that the phase boundary towards washout (white line) flattens for large $D$, as $v$ approaches the chemostat washout limit (dashed white line). The results obtained for different combinations of $L$ and $\lambda_0$ are shown in Fig. 3.S2. Convergence towards a steady state is shown in Fig. 3.S3.

We next show the spatial density profiles of the steady-state solution, $\rho(x, t \to \infty)$ for different flow and mixing rates; see Fig. 3.2C and 2D, with the different values of $v$ and $D$ used in the simulation indicated in Fig. 3.2B. In agreement with the qualitative picture presented in Box 1, the density profiles are essentially flat above the cyan line (i.e., for $\ell/L \gtrsim 1$); see conditions V1 and D5. Washout is observed to the right of the red line ($\alpha \gtrsim 1$); see conditions V5 and D1. In between the cyan and red lines, the profiles exhibit substantial spatial dependencies.

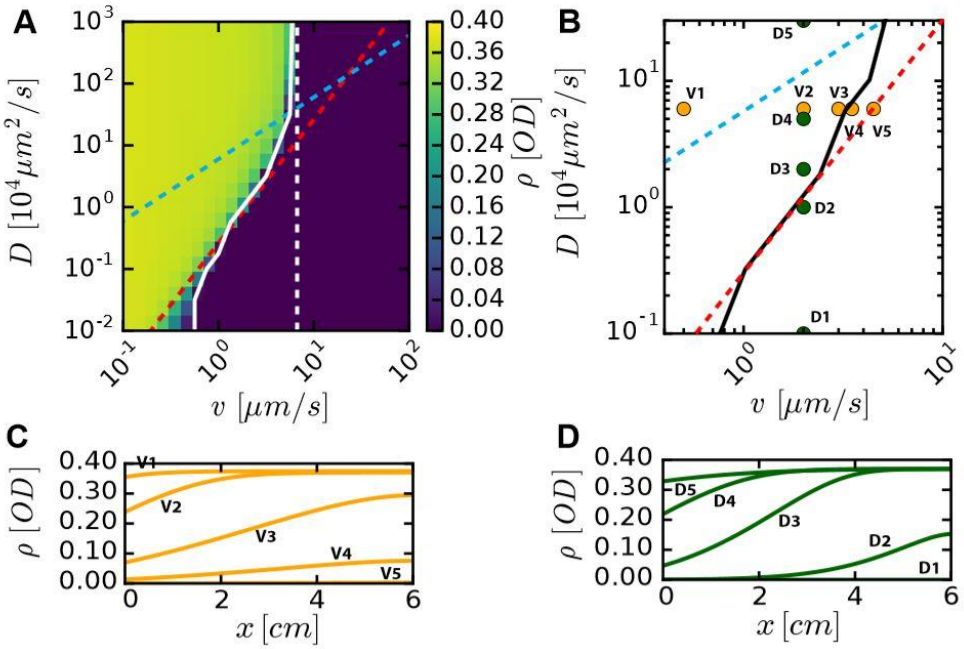


**Figure 3.2.** Model predictions for bacterial densities when varying degree of mixing and flow. (A) The bacterial density averaged over the channel length predicted by the model is plotted against $v$ and $D$ values. Solid white line denotes boundary towards washout, where average density has reached zero (<0.1% of the maximum value). Dashed red line shows $\alpha$=1.8, dashed cyan line show D/v=L. Chemostat washout condition $v/(\lambda L) \geq 1$. is denoted by the dashed white line. Steady state spatial density profiles in (C) for fixed D=2x10$^4$ μm$^2$/s and various values of v, and in (D) for fixed v=2 μm/s and various values of D, as shown in (B). The solid black line is the empirical phase boundary obtained from (A). Growth rate and nutrient inflow concentration used are $\lambda$=0.42 1/h and $n_{in}$ =2 mM, respectively.

### 3.2.2 Experimental Setup

Intestinal flow and contractions are difficult to control or characterize in vivo. To test the predictions of the above model, we constructed a fluidic mini-gut device (Fig. 3.3A and S4). In this device, bacterial growth occurs in a rectangular channel, 7 cm long with a 2x4 mm cross-section. Fresh medium containing nutrients is continuously supplied from one end of the channel, setting a mean flow velocity that can be changed from zero to over 50 μm/s. The ceiling of the channel is made of a silicone elastomer and has a regular array of 8 individually addressable, pressure-actuated membrane valves (4 mm wide valves with 7 mm period of the array)(78). The application of pressure to a valve leads to its

contraction, emulating local contraction of intestinal walls (see the SI for a detailed technical description). The application of different levels of pressure to the valves at different times generates a broad range of spatial-temporal patterns of valve contraction and partial channel occlusion (from a minor reduction of the channel height all the way to the ceiling touching the floor). As expected, the flow in the channel resulting from contraction of the valves led to efficient mixing along the channel, especially, when the ceiling touched the floor, resulting in major occulusion. The efficiency of mixing was characterized for different patterns of valve contraction that involved the actuation of each of the eight valves during each cycle of valve contraction (e.g., a peristaltic wave, valves actuated in a random order, etc). To this end, a small blob of a fluorescent dye (or particles) was injected near the middle of the channel, and the spreading of the fluorescence intensity (proxy of dye concentration) along the channel was measured as a function of the number of cycles of valve contraction (Fig. 3.S5 and SI).

For periodic peristaltic waves and an aqueous solution of the fluorescent dye, the spreading, quantified as the standard deviation of the spatial dye distribution along the channel, was well fitted by a square root of the number of cycles (Fig S5A,B). Hence, the spreading was a diffusion-like process with an effective diffusion constant, $D$, set by the valve-generated hydrodynamic flow (known in fluid dynamics as the eddy diffusivity). At the shortest feasible period of the peristaltic wave ($\sim$10 sec), $D$ reached $\sim 10^5\ \mu m^2/s$, more than 3 orders of magnitude enhancement as compared to the molecular diffusion of the fluorescent dye (Supplementary Information and Fig. 3.S5). Importantly, the value of $D$ for an aqueous suspension of 2 μm fluorescent beads (similar in size to bacterial cells) was close to the value measured for the fluorescent dye (Fig. 3.S5 C and D), in spite of

$\sim$100 times lower particle (molecular) diffusivity of the beads (0.2 vs. 25 μm$^2$/s). This result suggests that flow-induced effective diffusivity, $D$, is universally applicable to particles and molecules of all sizes (an expected outcome for $D$ significantly greater than the molecular diffusivity). Furthermore, when random patterns of valve contractions were applied instead of the regular peristaltic waves, the spreading of the fluorescent dye along the channel was substantially slower ($\sim$5 times reduced effective $D$; Fig. 3.S5 E and F). Last, we measured the spreading of the fluorescent dye when the carrier liquid had an ~10x greater viscosity than water (Fig. 3.S5 G-J) and found $D$ to be $\sim$2 times lower than for the aqueous solution. (The reduction in $D$ was likely mostly caused by changes in the flow pattern rather than in the molecular diffusivity of the dye.) The tested range of viscosity agrees with direct observations in the gut (79). For most of the experiments with bacteria, we applied peristaltic waves with a period of 120s and had a solution with viscosity 2 times higher than water, resulting in an effective diffusion constant $D \approx 2 \cdot 10^4$ μm$^2$/s (Fig. 3.3B). This diffusion constant is $\sim$20 times greater than the molecular diffusivity of small molecules and $\sim 10^5$ greater than the particle diffusivity of non-motile *E. coli*.

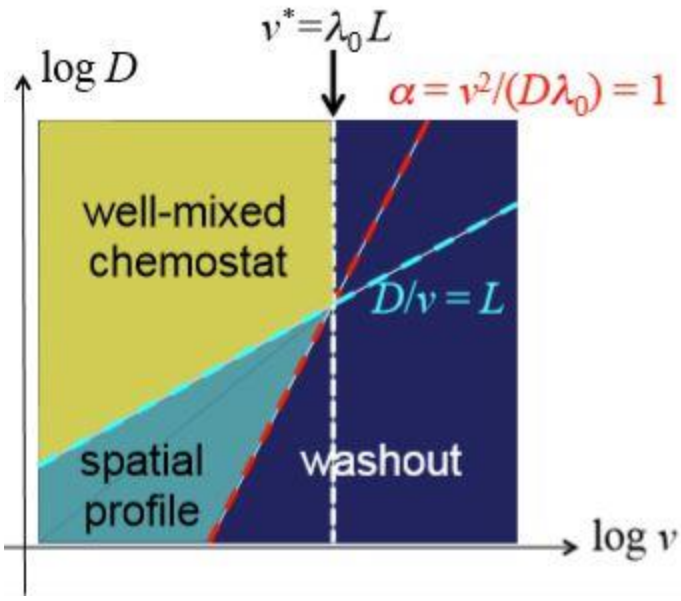


**Figure 3.3: Qualitative description of the behaviors of the reaction-diffusion model.** The combined effect of flow and mixing defines a "diffusive mixing length" $l \equiv D/v$. For length scale below ι, the culture is locally well mixed. If mixing is sufficiently strong such that ι becomes comparable to the length of the channel, i.e., $l \sim L$, then we may regard the entire channel as a well-mixed chemostat, with a "dilution rate" v/L. A chemostat can only sustain a stable culture below the chemostat washout condition (90), i.e., when the ratio of dilution and growth rates, $\alpha_L \equiv (v/L)/\lambda$, is below 1. This translates to a critical flow velocity $v^*=\lambda L$ above which washout occurs (dark blue region). This condition is shown as the dashed white line, together with the dashed cyan line, $l = L$, which indicates the boundary of the chemostat regime (region in yellow). For lower degrees of mixing where $l \leq L$ (to the left of the dashed cyan line), chemostat results do not apply. Here, the system consists of a number of locally well-mixed segments of length ι, and the characteristic ratio of dilution to growth becomes $\alpha \equiv (v/l)/\lambda = v^2/(D\lambda)$, for each of these segments. We may expect $\alpha=1$ as an approximate criterion for washout in a long channel. This condition is shown as the dashed red line, above which washout occurs (dark blue). In between the cyan and red line (teal region), we expect a stable solution to exist in the channel. Solution in this regime is generally not expected to be spatially uniform, as it is no longer well mixed.

### 3.2.3 Spatiotemporal Density Profiles in the Mini-gut

To study bacterial growth under the influence of flow and mixing and to test the predictions of the reaction-diffusion model, we grew fluorescently labeled *E. coli* cells (strain EQ403, see SI) in minimal medium in the device. Cells were first grown in batch culture to the mid-log phase before transferring to the device. Flow of the medium was then turned on and mechanical contractions were applied at set amplitude and frequency for the duration of the experiment. At regular intervals, cell density was monitored along the

device by counting cells in a fixed volume using a confocal microscope, see SI and Fig. 3.S6. We characterized the spatiotemporal dynamics in the device for different combinations of mixing and flow conditions (Fig. 3.S7A). In agreement with the theoretical predictions, weak peristaltic mixing (low effective diffusivity) led to washout (blue symbols, Fig. 3.S7B; see also Fig. 3.S8A), while stronger mixing stabilized the culture (red symbols, Fig. 3.S7C). Conversely, for a given effective diffusivity, fast flow led to washout (orange symbols, Fig. 3.S7B) while reduced flow rate stabilized the culture (red and green symbols, Fig. 3.S7C). The full spatiotemporal dynamics were measured for a constant rate of cycles of membrane contractions (constant effective D) and varying flow rates, v , (Fig. 3.3C-E) as well as for varying D and constant v (Fig. 3.S8A,B). The drop in bacterial density over time for the fast flow (Fig. 3.3C) indicated washout that occurred despite mixing. At lower flow rates (Fig. 3.3D, 3E), stable bacterial densities were obtained. The culture in Fig. 3.3E had a steady state with a weak spatial dependence, while the one in Fig. 3.3D exhibited a strong spatial dependence, with ~4x higher density at the exit compared with the entrance.

To compare the experimental results to the predictions of our model (Fig. 3.2 and Box 1) qualitatively, we use the experimental values of $v$, $D$, and $\lambda$ to obtain the mixing length $\ell = D/v$ and the $\alpha$-parameter (Fig. 3.3 and Fig. 3.S7A,B). For the conditions corresponding to Fig. 3.3E, we have $\ell \approx L$ and $\alpha \approx 0.1$, indicating that the entire channel can be regarded as a well-mixed chemostat, and hence little spatial dependence should be expected. For the conditions corresponding to Fig. 3.3D, $\ell \approx L/6$ and $\alpha \approx 1.2$, indicating that the system is in the regime where a strong spatial pattern is expected. For the conditions of Fig. 3.3C and S8A, we have $\ell \ll L$ and $\alpha \gg 1$, corresponding to the washout regime.

For more quantitative comparisons, we simulated the reaction-diffusion model (Eqs. 1-2) using the same experimental values of $v$, $D$, and $\lambda$ (Table S1, Fig. 3.S10AB). The spatiotemporal density profiles predicted by the model are shown below the corresponding data in Fig. 3.3F-H, and Fig. 3.S8C,D. The agreement between the predicted and observed density profiles is remarkable given the lack of any fitting parameters in the model. We note, however, that bacterial growth at the channel walls inevitably leads to deviations from model predictions. Moreover, there is a steady increase in the experimental noise due to increased scattering of light by cells growing on the walls and gas bubbles emerging on the walls, practically limiting the duration of experiments to ~20 hrs.

The model also predicts that, at long times, the effect of small variations of $v$, $D$, and $\lambda$ on bacterial density distribution is strongest at conditions leading to non-uniform bacterial density along the channel, $\alpha \lesssim 1$ and $\ell < L$ (Fig. 3.3D, G). We performed two more experiments at the same flow conditions as in Fig. 3.3D ($D = 2 \cdot 10^4\ \mu m^2/s$, $v = \mu m/s$), and the results (Fig. 3.S9) indicated general robustness of the experimental system and reproducibility of the growth dynamics. Similarity and slow evolution of the density distributions at long times were also consistent with the existence of a final stable distribution that, according to the model, the system converges to.

Together with the direct characterization of mixing dynamics (Fig. 3.S5), our results establish that complex hydrodynamic mixing due to channel wall contractions is captured by the reaction-diffusion model and that regularly occurring wall contractions can effectively prevent washout. A combination of bacterial growth, flow, and mixing can generally lead to systematic variations in bacterial density along the min-gut.

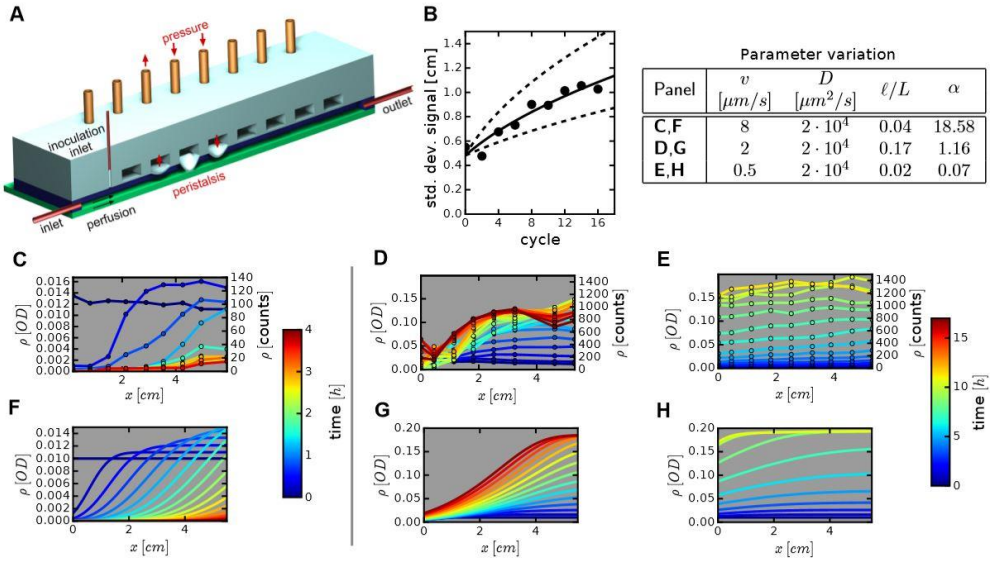


**Figure 3.4.** Effect of mixing and flow on bacterial growth. (A) Schematic of the mini-gut device with controlled "contractions" implemented by pressure-induced membrane deformations. (B) Mixing dynamics due to wall-contraction is quantified by locally injecting fluorescent dye near the middle of the channel and measuring the spreading of the dye distribution along the channel with time. The width of the distribution is shown after different numbers of cycles of peristaltic contractions. The data is shown for a waiting time of 120s between cycles, and it is fitted to diffusion-like spreading (solid line), with an effective diffusion constant of $D=2\text{x}10^4$ μm$^2$/s; see Fig. 3.S5 for further details. (C-E) Cells from strain EQ403 grown in the device at different flow-conditions. Bacterial densities measured at various times and locations are plotted. Each line is a snap shot of the density profile, with the time color-coded. (C) Flow-dominated regime with no cells in steady state (washout). (D) Intermediate regime with distinct spatial dependence of bacterial density. (E) Mixing-dominated regime with little spatial dependence. The flow and mixing parameters are indicated in the legend table. Panels (F), (G), and (H) show numerical simulations of the corresponding system using the reaction-diffusion model with only independently measured parameters, see text. Experimentally measured cell-counts are converted to optical density (OD) using a constant conversion factor, see Fig. 3.S6 and Supplementary Information. Relative errors in density are below 20%.

### 3.2.4 Effect of Spatial Coupling on Cross-feeding

We next considered the effect of flow and mixing on interacting microbial populations. A common form of interaction among gut microbes is assumed to be cross-feeding (80). Examples include the breakdown of polysaccharides by Bacteriodetes and the utilization of the resulting monosaccharides by Bacteriodetes and other species including Firmicutes and *E. coli*; see e.g., Ref. (81). Cross-feeding on many fermentation products has also been described, including the uptake of acetate and lactate (81), and hydrogen

uptake by methanogens and sulfate reducing bacteria (82). To observe the possible effect of flow and peristaltic mixing on cross-feeding dynamics, we conducted experiments to investigate a simple mode of cross feeding using two synthetically designed *E. coli* strains, as illustrated in Fig. 3.4A. For the Producer (P), we used strain EQ403 whose properties were described above. This strain can break down lactose into glucose and galactose, but only metabolize glucose. As the Consumer (C), we constructed strain EQ386 which could not utilize lactose, but could grow on glucose or galactose; see SI for strain details and Fig. 3.S10 for characterization. The two strains were labeled by mCherry and GFP respectively, so that the abundance of each strain could be followed in the device over time using fluorescent microscopy. The two strains were first grown together in lactose batch culture; see Fig. 3.S10CD. Although the P strain grew faster initially, the two strained approached the same final density eventually since each strain could metabolize half of the nutrients (lactose). To study the result of flow and mixing, P and C were grown separately in batch cultures, in lactose and galactose minimal media respectively. Exponentially growing cells were harvested, washed and transferred together to the device, which is perfused with lactose minimal medium. Flow and mixing were set to the intermediate level described above (Fig. 3.3D), and cell count for each strain was monitored by microscopy as described above. The results are shown in Fig. 3.4B, 4C. Since C is not expected to affect the growth of P, the density profile of P is very similar to that obtained previously when P was grown alone (compare Figs. 3.4B and 3.3D). The density profile of C (Fig. 3.4C) is clearly very different from that of P. The average density is much lower, and the overall change in density of C at the entrance (x=0) and exit (x=6m) is larger, and the rise in density is shifted towards the distal end. (The mid-point of density increase is at x=1.5cm for P and x=3.5cm

for C.) Two effects may likely account for the shifted density profile for C: (i) C is closer to washout due to its slower growth rate in galactose. (ii) galactose accumulation increases along the proximal part of the device (due to the rise in P, Fig. 3.4B), so that C grows better towards the distal end. We examined bacterial growth for this cross-feeding system mathematically by expanding the reaction-diffusion model to two strains and two types of nutrients (lactose and galactose, assuming that glucose derived from lactose degradation is completely consumed by P), and including the differences in metabolism for the two strains (SI). Using previously determined physical parameters for the device and the measured growth properties of the two strains (Table S1, Figs 3.S10AB and SI), the model provides good predictions for the spatiotemporal bacterial and nutrient profiles with the bacterial profiles shown in Figs. 3.4D, 3.4E. Nutrient profiles are shown in Fig. 3.S11. Model predictions for the density of C (Fig. 3.4E) capture the observed density profile remarkably well again, given the lack of any adjustable parameters. The predicted spatial profiles of nutrient concentrations (Fig. 3.S11) show that the availability of galactose is indeed distal-shifted. Thereby reduced growth makes it even harder for C to maintain in the channel. Compared to batch culture growth, flow limits strong cross-feeding to occur in the channel when mixing is limited and does not lead to a well-mixed situation.

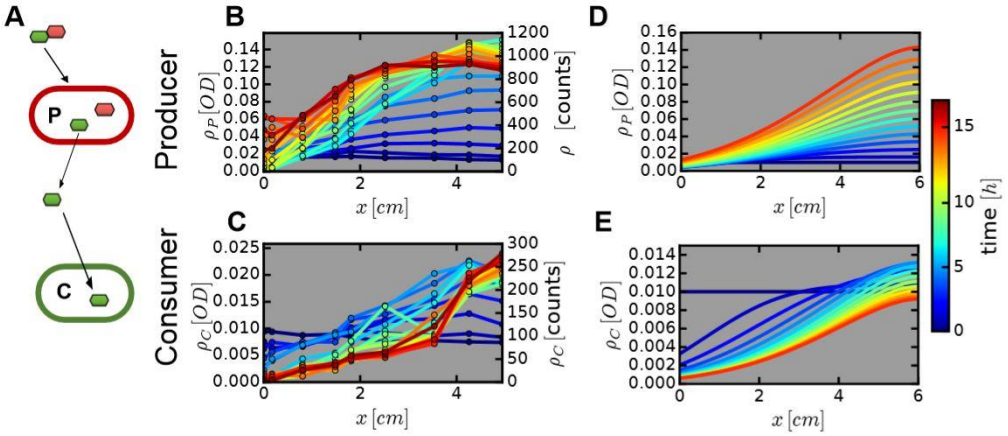


**Figure 3.5.** Two strain cross-feeding ecology. (A) The Producer strain (EQ403) that breaks down lactose (disaccharide of galactose and glucose, shown as linked red and green hexagons), but is able to metabolize only glucose (red hexagon), releasing galactose (green hexagon). The Consumer strain (EQ386) only metabolizes galactose released by the producer. The density profiles for the producer and consumer are shown in panel (B) and (C) respectively. Corresponding numerical solutions of the model are shown in (D) and (E). Producers and consumers were initially uniformly distributed ($OD_{600}$=0.01) and lactose was the only carbon source provided. In both theoretical model and experiment, the parameters used correspond to the intermediate regime shown in Fig. 3.3C. Relative errors in experiments are below 20%.

## 3.4 Discussion

In this work, we developed a new fluidic device, the mini-gut, to study bacterial growth in a gut-like system with controlled flow and wall contractions. The device allows the continuous observation of bacterial densities over time. The goal of this study was not to engineer a realistic model of the colon, but to evaluate the interplay between flow, mixing, and bacterial growth. Through mathematical modeling and experiments in the device, we demonstrated that the physical forces of flow and mixing could have a significant effect on bacterial growth and ecology: When combined with bacterial growth, recirculation flow generated by the channel wall contractions is sufficient to counter the washout effect that longitudinal flow along the channel exerts on the bacterial culture. Whereas strong and frequent wall contractions lead to homogeneous bacterial density and infrequent contractions do not prevent washout, contractions at an intermediate frequency

create a stable distribution with bacterial density substantially increasing along the channel. In this regime, different locations along the channel become different niches with distinct steady states. When a second bacterial strain is introduced into the channel, cross-feeding of metabolites of the first strain, these niches become even more distinct, with large variations of the density of the second strain and of the ratio of densities of the two strains. At a quantitative level, our work shows that despite the complexity of hydrodynamic flow associated with the contraction of the channel wall, its effect on bacterial growth can be captured by an effective diffusion term (eddy diffusivity) in a reaction-diffusion model.

For adult humans, with 1.5L/day of luminal fluid entering the colon (83), the average flow rate in the proximal colon is very high, $20\ \mu m/s$ or even higher across the first 20-cm of the proximal colon (see Supplementary Information). The degree of physical mixing by colonic contractions has not been systematically characterized in *vivo*. However, uncoordinated but continuous mixing has been observed in the proximal large intestine(84). Research also indicated that the balance of drift and diffusion was relevant in the real human gut (85). Further, observations with radiolabeled particles confirmed mixing in the proximal colon (86). Given the presence of strong flow and mixing, we expect the interplay of these two processes with bacterial growth to play an important role in maintaining a steady microbial population in the proximal large intestine. Some aspects of our model and the *in vitro* predicitions could be tested in future animal experiments. Interventions in mice to change the transit times through the gut, a proxy for flow velocity, have been successfully implemented (87) and could be adapted to test our predictions.

The prospect of partial local mixing, together with other changes along the length of the proximal colon not considered in this work, including changes in the flow rate (due to water absorption) (88), the oxygen content (61), and pH profile (89), makes it likely that growth and abundance of primary strains from the main phyla *Bacteriodetes* and *Firmicutes* are also strongly position-dependent in the proximal colon. This would in turn trigger a Domino effect that imposes spatial dependence on species that depend metabolically on these primary producers. Given that most of bacterial growth in the gut is happening in the proximal large intestine, these effects can contribute substantially to the microbiota composition of feces.

## 3.5 Supporting Information

In this supplementary text we give detailed information on the device construction, the used bacterial strains and growth-conditions, as well as the experimental procedures. We also present the details of the mathematical model.

The device is assembled of several parts, which are made of acrylic, polydimethylsiloxane (PDMS, silicone elastomer), and glass (Fig. 3.S4A). The 4 mm wide, 2 mm deep, and 60 mm long channel, serving as model of the colonic luminal tube, is machined in 2 mm thick acrylic by laser cutting. The acrylic part is 84 mm long and 20 mm wide. The channel is tapered at its inlet, a 0.6 mm diameter hole is drilled through the 2 mm thick face of the acrylic, and a short segment of hypodermic tubing (gauge 25) is glued into the hole to provide an inlet to the channel. To facilitate the assembly of the device, both sides of the acrylic part are coated with ~130 μm thick layers of a pressure-sensitive adhesive transfer tape (468MP by 3M), which are applied to the raw sheet of

acrylic prior to the laser cutting. To emulate flexible walls of the colon, the mini-gut channel is sealed from the top with a two-layer structure made out of flexible PDMS membrane and has an array of 8 identical and evenly spaced pressure-actuated valves. The valves are 4 mm wide with 3 mm spacing between them, such that the array spans 53 mm along the mini-gut channel. The upper layer of the PDMS structure is a ~84x20 mm (same as the acrylic part), ~10 mm thick chip, which is cast from a lithographically fabricated master mold. The master mold is a polished silicon wafer with ~300 μm tall micro-relief on its surface and is made using photolithography with an SU8 UV-curable epoxy (SU8-2100 by Microchem). The PDMS chip has an array of eight identical 300 μm deep microgrooves, which are 8 mm long, parallel to the shorter dimension of the chip, and evenly spaced by 7 mm along the longer dimension of the chip. The grooves are 4 mm wide at one end and are tapered to ~2 mm at the other end. ~1.5 mm holes are punched through the chip at both ends of the grooves and the engraved side of the chip is bonded to the lower layer of the PDMS structure, which is an ~150 μm thick flat-parallel sheet. The 150 μm sheet of PDMS is made by spin-coating a silicon wafer for 30 sec at 1000 rpm with a PDMS pre-polymer (50:50 mixture of Sylgard 184 by Dow Corning and XP565 (XP565 without Slygard 184) by Silicones Inc.) and curing the PDMS on the wafer in an 80°C oven for 2 hours. To promote good bonding, the surfaces of the PDMS chip and sheet are both treated with oxygen plasma. Upon bonding, the 300 μm deep microgrooves on the chip become cavities sealed at the bottom with the thin (150 μm) layer of PDMS, and the holes punched in the chip are used to pressurize the cavities, making the thin membrane at the bottom bend outwards. Two more holes are punched in the two-layer PDMS structure at the locations corresponding to places at the end and near the beginning of the mini-gut

channel. These holes are used as the min-gut outlet and a dedicated inoculation inlet for the injection of bacterial suspensions into the mini-gut channel. To assemble the mini-gut device, the bottom of the PDMS structure (the side of the 150 μm sheet not bonded to the chip) is treated with oxygen plasma and bonded to the adhesive on the top of the acrylic part by the application of pressure. Finally, the bottom of the acrylic part is sealed with a 75x25 mm microscope slide. Because PDMS is highly gas-permeable, pressurizing the cavities in the PDMS structure results in flow of air through the thin membranes at the bottom and can eventually lead to the formation of air bubbles in the mini-gut channel. To suppress the air bubble formation, the cavities are filled with water, which is injected from the narrow (2 mm) ends of the cavities. After the cavities are filled, the holes at the wide (4 mm) ends of the cavities are blocked, and the holes at the narrow ends of the cavities are used to pressurize the cavities. The application of air pressure to a cavity bends a 4x4 mm segment of the thin PMDS membrane (the region where the 4 mm wide cavity in the PDMS chip intersects with the 4 mm wide mini-gut channel) towards the bottom of the channel. The cavities are pressurized individually through eight separate lines of PVC tubing, with each line ending with an L-shaped segment of hypodermic tubing inserted into the PDMS chip. The other end of each line of tubing is connected to the “common” port of a dedicated miniature 3-way solenoid valve (LHDX0514600BA by LeeValves). The tubing line is vented to the atmosphere, when the valve is not powered, and connected to a pressure-regulated source of compressed air, when the valve is powered. The eight solenoid valves were individually switched on and off using a board of eight relays and an Arduino Mega microcontroller. The controller is programmed to periodically repeat certain patterns of actuation of the solenoid valves and thus of bending of the PDMS membrane valves. The

individual membranes and cavities, as well as their pressure inlet ports, tubing lines, and solenoid valves, are numbered 1 to 8 starting from the valve most proximal to the mini-gut inlet. Because of inevitable minor differences in the actual thickness of the PDMS membranes (and their Young's moduli) between different batches, to ensure that the bending of the membranes at the top of the mini-gut channel is consistent between experiments with different devices, each device is individually calibrated. The calibration is performed by applying varying air pressure to the valve ports and observing the membranes under a microscope. Whereas the pressure is switched on and off individually for different valves, the pressure applied to different valves in the "on" state is the same and, because of inevitable minor differences between individual membranes, their deformations in the "on" state are somewhat different as well. To minimize the effect of this variability, the standard choice is to use a pressure just above the level at which the least compliant membrane touches the bottom of the mini-gut channel (the membrane deformation of ~2 mm). Once a membrane touches the channel bottom, its deformation becomes less pressure-dependent, because of the opposing reaction force. These relatively large membrane deformations might be comparable to what happens during haustrations and coordinated peristalsis in the colon in vivo, providing major displacements of the content of the lumen in single events. In addition, the point (pressure level) when the membrane touches the channel bottom is practically simple to register under a microscope. The pressure at which the least compliant membrane touched the mini-gut channel bottom varied between 24 and 31 kPa (3.5 to 4.5 PSI). This level of pressure, which is set by the diameter (4 mm), thickness (150 μm), and Young's modulus (~2 MPa) of the membrane valves, and the depth of the mini-gut channel (2 mm) is a reasonable compromise. On the

one hand, it corresponds to relatively high effective spring constants of the valves, such that the valves remain largely flat when there is no pressure applied and rapidly recoil to near-flat shapes when depressurized. On the other hand, this pressure is sufficiently low to minimize the risk of delamination of the 150 μm membrane from the PDMS chip and of the chip from the acrylic part.

The standard pattern of actuation of the valves is a peristaltic wave propagating from the mini-gut channel inlet to its outlet (Fig. 3.S4B). The valves 1 and 2 are pressurized first, then valve 1 is depressurized and valve 3 is pressurized, then valve 2 is depressurized and valve 4 is pressurized, and so on. The standard interval between consecutive steps is 0.5 sec, with the interval between consecutive peristaltic waves being an experimentally controlled variable defining the time-averaged rate of movement of the content of the mini-gut channel (peristaltic mixing) induced by the deformation of its top wall. Whereas this spatial pattern may be a closer emulation of coordinated peristalsis than more disordered haustrations in the colon, for this pilot study, we have chosen to select mostly one simple spatial-temporal pattern of deformation of the top wall in order to have a single variable quantifying the rate of mixing in the channel (frequency of the peristaltic waves). As a different limit of contraction modes, we also checked the effect of randomly chosen contraction patterns for mixing (Fig. 3.S5 C,D). Here, during a contraction cycle, each valve was chosen to contract once, with the order following a random sampling. For repeated cycles, orders were newly determined from a random sampling. Timing was similar to the peristaltic patterns as described before. Timing was similar to the peristaltic patterns as described before. For shown mixing behavior, drawn contraction order was {(6, 1, 4, 5, 7, 3, 2, 8), (4, 6, 1, 7, 8, 2, 5, 3), (7, 2, 8, 4, 5, 1, 3, 6), (2, 5, 7, 8, 3, 6, 4, 1), (2, 5,

1, 3, 8, 7, 4, 6), (6, 4, 3, 7, 2, 5, 8, 1), (5, 2, 6, 4, 8, 1, 3, 7), (5, 2, 1, 7, 4, 3, 6, 8)} for the 8 cycles.

During the normal operation of the mini-gut device, the movement of the content of the mini-gut is due to a combination of continuous perfusion from the inlet to the outlet and periodic peristaltic waves (Fig. 3.S4A). (The inoculation inlet is blocked immediately after the bacterial suspension is injected into the mini-gut channel.) The channel is perfused by connecting both the inlet and outlet to reservoirs with growth medium and by connecting the inlet reservoir to a source of pressure-regulated compressed air, thus applying a higher pressure to the inlet than the outlet. To achieve the desired flow rate through the mini-gut, with mean flow velocities around 10 μm/sec, at practically convenient air pressures (~70 kPa), the tubing line connecting the mini-gut inlet with the inlet reservoir has a fluidic resistor in it, which is a 75 mm long segment of PEEK tubing with an inner diameter of 63 μm. The mean flow velocity in the mini-gut is readily adjusted by varying the pressure applied to the inlet reservoir. The velocity is proportional to the pressure (with a coefficient of proportionality of ~1 μm/sec per 4 kPa). The mini-gut outlet is connected to the outlet reservoir through a low-resistant PVC tubing line. Therefore, when the membrane valves bend down, thus reducing the effective volume of the mini-gut channel, the medium is pushed from the channel nearly exclusively towards the channel outlet and the outlet tubing line, and the pressure in the mini-gut channel remains nearly unchanged. As a result, the membranes that are not pressurized always remain nearly flat. (When the peristaltic wave is over and the mini-gut channel regains its full volume, the medium from the outlet tubing returns to the channel.)

To test the effect of the peristaltic waves (or random contraction patterns) of the advection of a low-diffusivity species (such as ~1 μm size bacteria) in the mini-gut channel, we tracked the spreading of a fluorescent dye (high molecular weight dextran, FITC, FD-500S from Sigma). Alternatively, we aslo tracked fluorescence beads $2\mu m$ in size. To adjust viscosity we used different concentrations of a glycerol solution (no glycerol for 1x viscosity of water ($\sim 4\ cPs$ at room temperature), 25% for 2x viscosity, 50% for 10x viscosity). A small volume of solution of the dye was injected into the mini-gut channel between valves 4 and 5 (through a specially made hole), and the distribution of the dye along the length of the channel was visualized under light sheet fluorescence illumination using macro-photography with a Canon EOS-1D Mark I. The image covered the entire channel. The light sheet illumination was derived from a solid state 450nm laser, whose beam, illuminating the mini-gut channel from a side, was expanded to a line along the length of the channel cylindrical lenses ("line" mode of the laser beam). The camera had two f/1.4 lenses attached to it, with the second lens mounted in reverse to the first one (reversed lens macrophotography) and an optical filter blocking the laser light inserted between the lenses, such that only the fluorescence light emitted by the dye was collected by the camera. To prevent scattering from laser cutting strip patterns, the side part of the acrylic channel was polished. Further, to prevent scattering by changed refraction index a solution of 15% NaBr and 35% KI was used to match the refraction index of PDMS, which is about 1.41. By aiming the laser from the side, we were able to illuminate across the entire channel, which gave us the signal from the entire channel, not just a single plane. The device was photographed after the dye was injected into the channel and also after 1, 2, 4, 8, and 16 complete cycles of contractions. The images were digitally processed by

subtracting the background (intensity with no dye in the channel) and calculating the distribution of the mean intensity across the channel as a function of the position along the channel. To correct for non-uniformity of the illumination (uneven intensity of the laser beam) and light collection, the distribution of intensity was then normalized with the distribution obtained with the min-gut channel filled with a uniform solution of the fluorescent dye (flat-field correction). The reduction of the complex three-dimensional distributions of dye in the channel to simplified one-dimensional profiles is justified by the results of our numerical simulations, which indicate that in the context of prevention of bacterial washouts, the main effect of secondary flows in the channel is the displacement of the channel content upstream along the channel. To quantify spreading of the fluorescent signal, we normalized the intensity and corrected for variations in illumination intensity by setting the background signal (boundary of profile which has not been reached) to zero for each cycle. Calculations were then performed with the proper conversion factor from pixels to actual position along the channel. Intensity patterns shown in Fig. 3.3 show signals averaged over 10 pixels.

All the strains used in this study were derived from *E. coli* K-12 strain NCM3722 (91), and are summarized in Table S2. Strains NQ1242 and EQ356 are deleted for $galK$ and $lacIYZ$, respectively. Fluorescence is expressed by plasmids with mCherry and GFP under the control of a constitutive tet promoter. Constructs are described in the following. All oligos used for making constructs are listed in Table S3.

The lacI, lacZ and lacY genes involved in lactose utilization were deleted from the chromosome of MG1655Seq following the methods of Datsenko and Wanner (92).The

Kmr gene present in pKD4 was amplified using primers lacI-P1 and lacY-P2 (Supplementary Table 3). The PCR products were treated with DpnI, gel purified, then electroporated into electro-competent cells of MG1655Seq expressing a lambda recombinase encoded in pKD46. After 1 hr incubation at 37 oC with LB, the cells were plated onto LB + Km agar plates. The plates were incubated at 30 oC overnight. The Kmr colonies were verified for the replacement of the lacIYZ genes with the Kmr gene by colony PCR, followed by sequencing with primer lacY-ver-R. Then the Kmr gene replacing the lac genes was transferred to the NCM3722 strain by P1 transduction. The Kmr gene was flipped by transformation of pCP20 (92), yielding strain EQ356. The deletion of galK in MG1655Seq background is described in (93). Such deletion was transferred to NCM3722 by P1 transduction, yielding NQ1242.

PtetM2 is a stable version of Ptet. PtetM2 was amplified from Ptet using the primers Ptet-mod-F2 and Ptet-mod-R. The PCR products were digested with XhoI/KpnI, gel purified and then were substituted for Ptet in pZA31Ptet-gfp (94), yielding pZA31PtetM2-gfp. This plasmid was transformed into EQ356, yielding green fluorescence-producing strain EQ386.

mCherry was amplified from pRSET.B-mCherry (95) using primers mCherry-Kpn-F and mCherry-Bam-R. The PCR products were digested with KpnI and BamHI, gel purified and then substituted for gfp in pZA31Ptet-gfp (94), yielding pZA31Ptet-mCherry. This plasmid was transformed into NQ1242, yielding red fluorescence-producing strain EQ403.

Growth was carried out in MOPS-buffered minimal media, following Neidhardt (96). pH was adjusted to pH 7.4 with NaOH. For experiments with plasmids, 30 $\mu g/ml$ chloramphenicol was added. 10 $mM\ NH_4Cl$ was added as nitrogen source. When not stated otherwise, $2mM$ lactose or galactose was added as carbon source.

Cells were grown at 37°C, in a water-bath shaker (220 rpm) or in the mini-gut device. For initiation of growth, strains from a fresh colony on an LB plate were grown first as seeding cultures in LB broth. At $OD_{600} \sim 0.5$, strains were transferred to fresh minimum medium containing the described carbon and nitrogen sources. Cells were grown over night. The next morning, with cells still in exponential phase, cells were washed twice by centrifuging at 10,000 RPM for 1.5 min. For batch culture growth, cells were then diluted to $OD_{600} \sim 0.05$ and growth was observed over time. For growth in the mini-gut, one or two strains where diluted to $OD_{600} = 0.01$ for each strain. Cells were then loaded into the device via the inlet-channel of the device. For growth experiments in the device, viscosity has been adjusted using… leading to a viscosity of approximately 2x higher than water.

Growth-rate and yield has been observed for strains EQ403 and EQ386 in medium supplemented with the proper carbon source. No growth was observed for EQ403 and EQ386 for growth with galactose or lactose as sole carbon source respectively. Exponential growth was observed with strains EQ403 and EQ386 when growing in lactose and galactose as sole carbons source respectively, c.f. Fig. S7AB with growth rates 0.32 $h^{-1}$ and 0.61 $h^{-1}$, respectively. To estimate yield, growth of EQ403 and final $OD_{600}$ was observed for different lactose amounts supplemented to the media, giving a yield of $Y =$

$0.184\,\frac{OD}{mM}$. The Monod constant, $K_m = 0.1$ was estimated from the same experiments by fitting Monod growth kinetics to the observed growth curve.

To analyze lactose consumption in the delta galK strain NQ1242, four samples of 200µl were taken at regular intervals during exponential growth. These samples were filtered by centrifugation using 0.22µm nylon filter centrifuge tubes (Corning Costar Spin-X Centrifuge Tubes). The filtrate was then analyzed using a Shimadzu Prominence HPLC using RID detection. Isocratic HPLC was used with 10mM $H_2SO_4$ as mobile phase at 0.4ml/min pump speed. Samples were separated using ion exchange chromatography; the column (Phenomenex, Rezex ROA-Organic Acid H+ (8%), LC column 300 x 7.8mm) was kept at 40°C; data from the RID detector (Shimadzu RID-20A) was recorded for 40 min. Data was subsequently exported and analyzed in Ref. (97) to determine the areas under the peaks of interest. The corresponding concentrations were determined by comparing these areas to a measured standard curve.

Cell growth in the device was observed with a Leica SP8 laser scanning microscope (inverted). Fluorophores were excited with lasers at wavelengths 488 and 552 nm. Detectors were scanning in the wave-length range $495 - 545$ nm for GFP and $585 - 700$ nm for mCh. Temperature was controlled using an environmental chamber with temperature stabilized at 37°C. Cells were observed with a 10x long distance objective ($NA = 0.3$). Cell-densities were determined by observing within defined volumes of $100 \cdot 100 \cdot 300\ \mu m^3$ (3nl) at different positions along the length and depth of the device. We took 9 images at equidistant locations along the length of the device, then for each of those, 2 images across the width of the device and for each of those 5 images across the height of

the device (total 9×2×5 = 90 images). It took about 7 minutes in total to do this entire scan, which includes moving the stage between each of the 90 positions. Distance of $\delta z = 250\ \mu m$ was used between different z-slices. Conversion to cell-counts was done by a customized script using ImageJ (Fiji). High contrast allows reliable detection of cell densities up to OD of ~0.5 (approx. $10^9$ cells per ml). Cell count was confirmed by a calibration curve. For this, a device was loaded with cell-cultures from batch culture growth at different $OD_{600}$ levels. The behavior is shown in Fig. 3.S5. Linear behavior is observed in the range $OD_{600} = 0.001$ to $OD_{600} = 0.5$.

To investigate the role of laminar flow-profiles, we performed simulations explicitly considering flow-velocity profiles. The results are shown in Fig. 3.S1. In this paragraph, we describe these simulations in detail. The domain of numerical simulations is a two-dimensional channel, 70 mm long and 2 mm tall. The flow in the channel is a superposition of a longitudinal flow from left to right and a recirculation vortex. The longitudinal flow represents the time-averaged flow of the luminal content down the colon and has a parabolic (Poiseuille) profile along the vertical direction, uniform profile along the channel (horizontal direction), and a maximal velocity of 3 μm/sec. The recirculation vortex represents the effect of haustrations and peristalsis in the colon that result in relative displacements of different parts of the cross-section of the lumen, with zero net mass transport along the colon. The recirculation vortex is localized to an upstream part of the computational domain (18 mm long, 6 to 24 mm from the channel entry) and has a maximal longitudinal velocities of 15 μm/sec upstream in the lower half of the channel and 15 μm/sec downstream in the upper half of the channel. Growth of the bacterial concentration, *c*, is modelled by an exponent with a characteristic time $T$ = 40 min and a non-linear

saturation (representing the depletion of nutrients and accumulation of metabolites) at a relative concentration $c$ = 10: $dc/dt = (c - 0.1c^2)/T$ . The diffusion constant for bacteria is set at 5 $\mu m^2$/sec. The initial condition is a uniform seeding of bacteria at $c$ = 1 in a 2 mm long segment between 2 and 4 mm from the channel entry. In Fig. 3.S1A, we show the schematics of the computational domain with color-coded distribution of the bacterial concentration, *c*, at a steady state reached with the recirculation vortex (1000 hrs after seeding of the bacteria). The steady state has non-zero concentration of bacteria in the bulk of the channel, with the highest level of *c* (~70% of the saturation) reached at the location of the recirculation vortex. In Fig. 3.S1B we show the dynamics of bacterial relative concentration, *c*, along the central axis of the channel at different time points from the beginning of the simulation with *no recirculation in the channel* (only longitudinal flow with no recirculation vortex). The inoculum initially seeded at the channel entry reaches the channel exit at ~7 hrs and by ~10 hrs there is a nearly complete washout. Now with added *recirculation vortex* (Fig. 3.S1C), the inoculum reaches the channel exit by ~10 hrs, but a part of it is retained in the region of the recirculation vortex. The concentration of bacteria in the region of recirculation steadily increases (up to ~70% of the saturation in the steady state), and those bacteria end up populating the channel downstream to a relative concentration of up to ~2. Hence, the simulation indicates that the combination of bacterial growth and of the flow upstream in the region of recirculation prevents the washout and leads to a steady state with characteristic concentrations at substantial percentages of the saturation level.

The main model used is defined by Eq. (1) and (2) introduced in the main text. The explicit consideration of both bacterial density and nutrients allows the investigation of how those quantities are coupled in a flow environment. Further, it allows the natural implementation of boundary conditions. Boundary conditions are chosen to match the conditions in the device, as follows: at the inlet $(x = 0)$ there is zero cell flux $j_\rho(x = 0) = -D\partial_x\rho|_{x=0} + v\rho(x = 0) = 0$ and fixed nutrient flux $j_n(x = 0) = -D\partial_x n|_{x=0} + v\, n(x = 0) = v\, n_{in}$. At the outlet, $(x = L)$, there is an unobstructed outflow of both cells and nutrients, with zero diffusive flux: $j_\rho(x = L) = -D\partial_x\rho|_{x=L} = 0$ and $j_n(x = L) = -D\partial_x n|_{x=L} = 0$.

Numerical solution of the partial differential equations was done employing an implicit scheme using python and the module FiPy, (98). Integration over time was performed with time steps $dt = 0.1\ s$ and a grid resolution with spacing $dx = 0.1\ mm$.

In the limit of very high mixing rates, where spatial differences vanish, the system behaves like a chemostat. Mathematically, this can be seen by noting that the main Equations (1) and (2) transform into the chemostat equations in this limit,

$$\partial_t r = f_r(r,n) - \frac{v}{L} r,$$

$$\partial_t n = -f_n(r,n) + \frac{v}{L} n_{in} - \frac{v}{L} n.$$

Here, $L$ denotes the length of the channel, and the dilution rate is given by $v/L$, compare with (99) (100). Nutrient concentration and bacterial density in the steady state are given by

$$n^* = K_m \frac{v/L}{l - v/L},$$
$$r^* = Y\left(n_{in} - K_m \frac{v/L}{l - v/L}\right).$$

Washout occurs for perfusion rates greater than,

$$v_{wo}^* = Ll \frac{n_{in}}{n_{in} + K_m}.$$

Typically, $n_{in} \ll K_m$, and thus washout is given at $v_{wo}^* = L\lambda$.

Producer strain EQ403 (*ΔgalK)* growing on lactose is unaffected by the consumer EQ386 (*ΔlacIYZ)*, which grows on galactose produced by the producer strain. Yield of galactose was set equal to the consumption of lactose by the producer strain, one molecule of galactose is obtained by breakdown of own molecule lactose; galactose production is described by the local source term $\frac{\lambda_P}{Y_P}\frac{n_L}{n_L+K_{M,L}}\rho_P$. Here $\lambda_P$ is the maximal producer growth rate, $Y_P$ the yield factor for the producer growing on, $n_L$ the lactose concentration, $\rho_P$ the producer density and $K_{M,L}$ Monod constant for lactose uptake by the producer. The complete set of equations is given by

$$\partial_t \rho_P = D\partial_x^2 \rho_P - v\partial_x \rho_P + \lambda_P \frac{n_L}{n_L + K_{M,L}} \rho_P$$
$$\partial_t n_L = D\partial_x^2 n_L - v\partial_x n_L - \frac{\lambda_P}{Y_P}\frac{n_L}{n_L + K_{M,L}} \rho_P$$
$$\partial_t \rho_C = D\partial_x^2 \rho_C - v\partial_x \rho_C + \lambda_C \frac{n_G}{n_G + K_{M,G}} \rho_C$$
$$\partial_t n_G = D\partial_x^2 n_G - v\partial_x n_G - \frac{\lambda_C}{Y_C}\frac{n_G}{n_G + K_{M,G}} \rho_C + \frac{\lambda_P}{Y_P}\frac{n_L}{n_L + K_{M,L}} \rho_P.$$

Boundary conditions are similar to those described before with galactose inflow set to zero. Parameters are based on published results or separate experiments shown in this study. Values used for shown simulations comparing with experiments (Fig. 3.5) are summarized in Table S1.

To estimate flow velocities in the proximal colon (including cecum and ascending colon), we consider the fluid volume reaching the large intestine each day, $Q_{il}$: Typical values are given by $Q_{il} = 1.5 - 2.0\ l/day$ (101, 102). Average flow velocity is following by taking the diameter of the colon into account and assuming a tubular shape. Measured values fluctuate a bit, given in the range of $2 - 3\ cm$ for the ascending colon (103, 104). For such a diameter range, flow velocities at the beginning of the colon are in the range of $24 - 74\ \mu m/s$. Water uptake is happening along the whole colon, not only in the proximal part. Thus as rough estimation, we argue with an average flow-velocity of at least $20\mu m$/s in the proximal colon.

Different factors add to this picture making the whole dynamics more complex. For example, flow velocities are expected to vary over the day and depend on meal intake. However, a basal permanent flow rate has been observed. Furthermore, water uptake along the colon is leading to a reduction in flow-velocity along the colon (with fluid outflow clearly lower in the distal colon and rectum, and fecal weights typically reaching not more than $200\ ml/day$)(105). However, as indicated by the accumulation of fermentation products and local pH values, bacterial growth is mostly happening in the proximal colon, were flow velocities are still high.

In addition to mixing, wall growth might be an important factor contributing to a stable bacterial population in the ascending colon. Bacteria attached to the epithelial mucus layer and associated wall growth help to prevent removal of bacterial cells even for very large flow-velocities. For example, in the large intestine bacteria attached to the mucus layer can help to recolonize the colon after diarrhea and the related strong drop in bacterial density within the colon. However, wall growth might be not so important for high bacterial densities in the colon observed for normal flow conditions. One reason is that microbiota composition in the mucus layer has been shown to be different compared to the microbiota composition in the lumen (see discussion in the main text). Another reason is given by growth dynamics alone: here we estimate the effect on wall-growth on bulk bacterial growth in the luminal tube. The results indicate that wall-growth alone is unlikely to account for high bacterial densities in the channel and that instead mixing is required for high cell densities to be maintained.

To study the effect of wall-growth, let us consider growth without mixing, but an additional growth term. Change of density is given by

$$\partial_t \rho(x,t) = -v\partial_x \rho(x,t) + \lambda_{max}(\rho(x,t) + \rho_0).$$

We here consider nutrients to be non-limiting, $\rho_0$ account for bacteria sitting in the mucus layer. Bacterial density is equal to the bacterial load from the ilium effluent entering the colon. Steady state solution with this boundary condition $\rho(x=0) = \rho_{il}$ is given by:

$$\rho(x) = (\rho_0 + \rho_{il})\, e^{\frac{\lambda}{v}x} - \rho_0.$$

That is, the growth profile is exponential. Assuming growth rates $\lambda = 0.4\ h^{-1}$ and $v = 15\ \mu m \cdot s^{-1}$, the doubling length scale is given by $l_2 \equiv \ln(2)\frac{v}{\lambda} \approx 9.4\ cm$. So even for these rather overestimated growth-rates and underestimated flow-velocities, the bacteria could undergo at most 3 doublings as they transit the human ascending colon (~20-30 cm), and not even one full doubling in the device described here.

As an extreme case mucus layer wall-growth, let us assume a very densely packed mono layer of cells, likely already an overestimation of real bacterial densities in the mucus layer (106). Consider a segment of the luminal pipe with width $dl$, surface area $A_{dl}$ and Volume $V_{dl}$, the number of cells sitting in the mucus layer is given by $N_{dl}^{cell} = A_{dl}/a_0$. The occupied area of a single bacterial cell is $a_0 \approx 1\ \mu m^2$. With a dry weight of a single cell, $m_{cell} \approx 0.3\ pg$, the effective density of the monolayer is given by:

$$\rho_0 = \frac{N_{dl}^{cell} m_{cell}}{V_{dl}} = \frac{4\, m_{cell}}{a_0 d} \approx 6 \cdot 10^{-5}\, \frac{g}{ml}.$$

Observed densities in the feces are about 1000 fold higher and of the order $6 \cdot 10^{-2}\, \frac{g}{ml}$ (107, 108). Now in addition to bacterial growth, there is water uptake in the colon. This uptake can lead to higher bacterial densities even if there is no bacterial growth. For a direct comparison of $\rho_0$ with fecal densities we have to take this effect into account. Given that inflow and outflow volumes are changing by a factor of 15 (see numbers stated before), the total density which is expected at the end of the ascending colon is still at least 50 times higher than the generously estimated density of cells provided by growth in the

mucus layer alone. Based on wall growth alone and without additional mixing, growth of this order of magnitude is unlikely to occur in the proximal colon.

In conclusion, since bacterial densities in the mucus cannot account for substantial densities $\rho_0$ (see below) and with growth limited to a few doublings, wall growth alone is unlikely to be the main factor supporting growth towards very high densities in the ascending colon.

For comparison between the cell counts / volume obtained experimentally and optical cell density as measured from batch culture steady-state growth and as used in the model (two scales in Fig. 3.3C-E and Fig. 3.4 in the main text), we use constant conversion factors. These conversion factors were obtained from linear fits to the calibration data (Fig. 3.S6). Since cell-size is changing with growth-rate, this approximation is justified if growth-rate is not changing much compared to the maximum growth-rate observed in balanced growth in batch-culture as used for the calibration in Fig. 3.S6.

Used conversion for both strains are:

$$\rho_{lac}(counts) = 11122\rho_{lac}(OD) + 13.17$$
$$\rho_{gal}(counts) = 7448.6\rho_{lac}(OD) + 14.88$$

## 3.6 Supplementary Figures

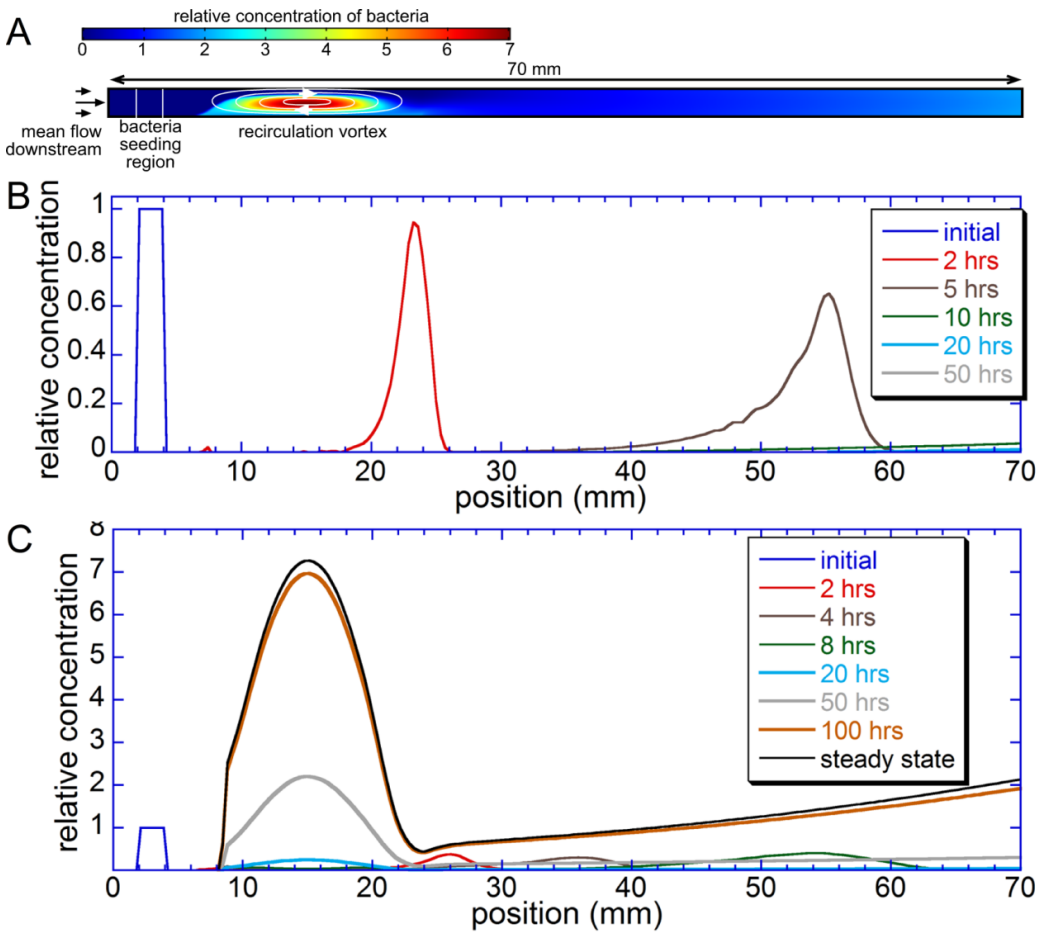


**Figure 3.S1. Hydrodynamic simulations of bacteria growth in a channel with longitudinal flow and recirculation**. (A) Schematics of performed simulations. Laminar flow profile with locally set recirculation vortex centered close to the channel entrance. (B) Spatiotemporal density profile without the recirculation vortex. A band of bacteria is seen to be flushed down the channel without much dispersion. (C) Spatiotemporal density profile with the recirculation vortex. A region of stable bacterial density (corresponding to the location of the vortex) is maintained indefinitely. See section "Mathematical model -- Laminar flow profiles and recirculation by mixing" for details. Note the different vertical scale than in B.

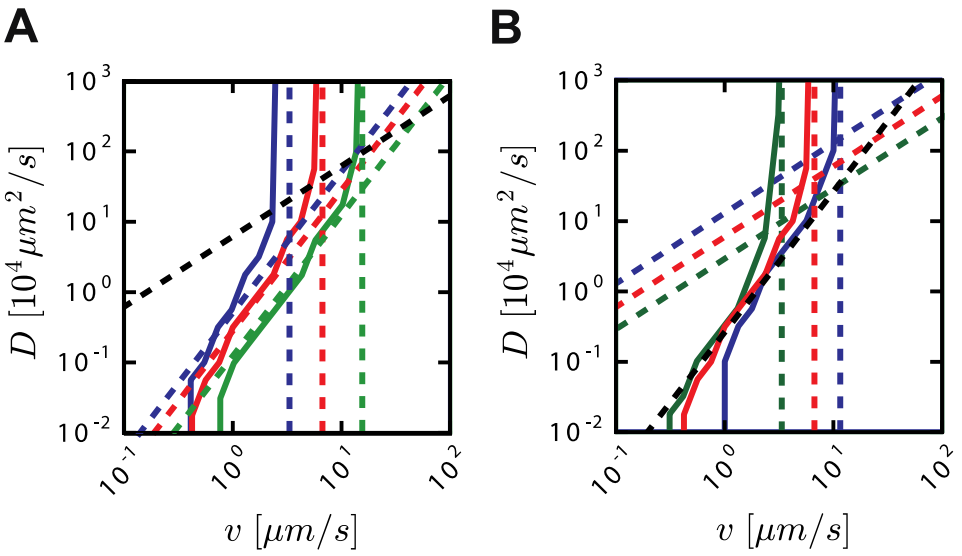


**Figure 3.S2. Phase diagrams in the $v$ - $D$ coordinates showing the dependence of washout conditions on the growth rate and channel length**. Solid lines indicate boundaries between washout and steady states with stable bacterial populations. (A) Washout at different growth rates, $\lambda_0$: $0.21/h$ (blue), $0.42/\text{h}$ (red), and $0.84/\text{h}$ (green) for a channel length $L = 6$ cm. Vertical dashed lines correspond to the chemostat washout, $v = v^* = L\lambda_0$, for different values of $\lambda_0$; tilted dashed lines correspond to $\alpha = 1.8$ (a characteristic value for which the combination of effective diffusion and growth can balance the flow, preventing the washout) for different values of $\lambda_0$. Black dashed line corresponds to $L = D/v$. (B) Washout at different channel length, $L = 3$ cm (green), 6 cm (red), and 12 cm (blue) for , $\lambda_0 = 0.42/\text{h}$ . Vertical dashed lines correspond to chemostat washouts, $v^* = L\lambda_0$. Tilted dashed lines are drawn along $D/v = L$. Black dashed line corresponds to $\alpha = 1.8$. Other parameters are set as in Fig. 3.2, with $n_{in} = 2$ mM.

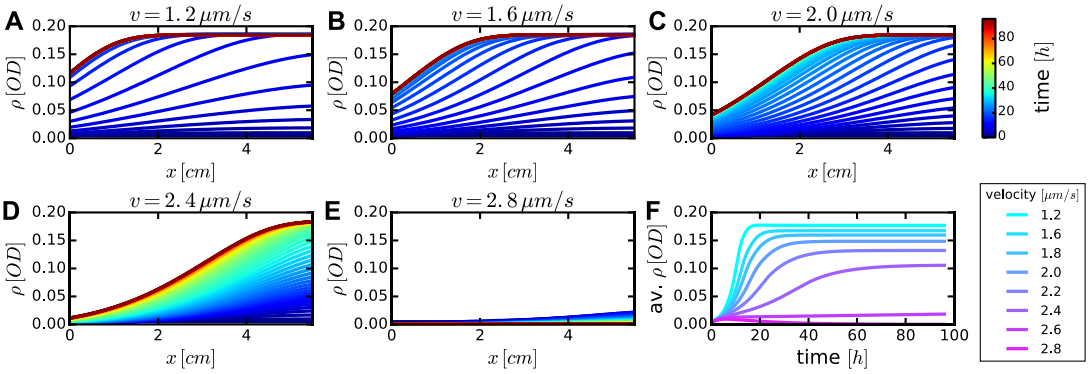


**Figure 3.S3: Convergence to steady state.** Dynamics of reaching steady states. (A)-(E) Spatial profile of bacterial density changing over time for different inflow velocities $v$ as noted above the panels. The simulation run-time (color-coded) was 96 hours. (F) Convergence to steady state illustrated by average density in channel reaching a constant value. Lines correspond to different flow velocities as stated in the legend. Effective diffusion is fixed to $D = 2 \cdot 10^{-4}\ \mu m^2/s$. Other parameters are set as in Figure 3.2.

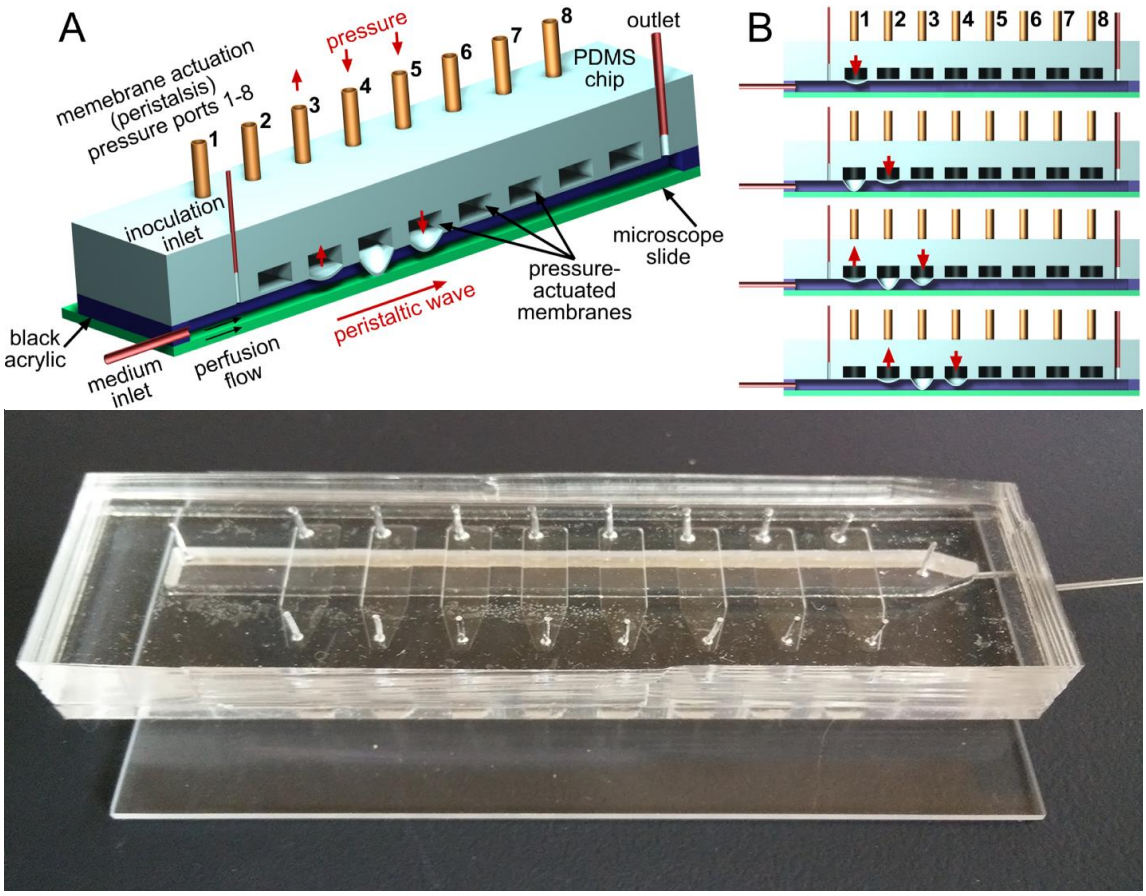


**Figure 3.S4. Mini-gut device.** (A) Schematic of the mini-gut device showing a cross-section of the mini-gut channel and the PDMS structure with the valves and cavities. The shape of the membrane valves corresponds to a phase of the peristaltic wave, when valve 3 has just got depressurized, valve 4 has been pressurized for 0.5 sec, and valve 5 has just got pressurized. (B) Cross-sections of the device at three consecutive stages of a peristaltic wave. (C) Photo of the device.

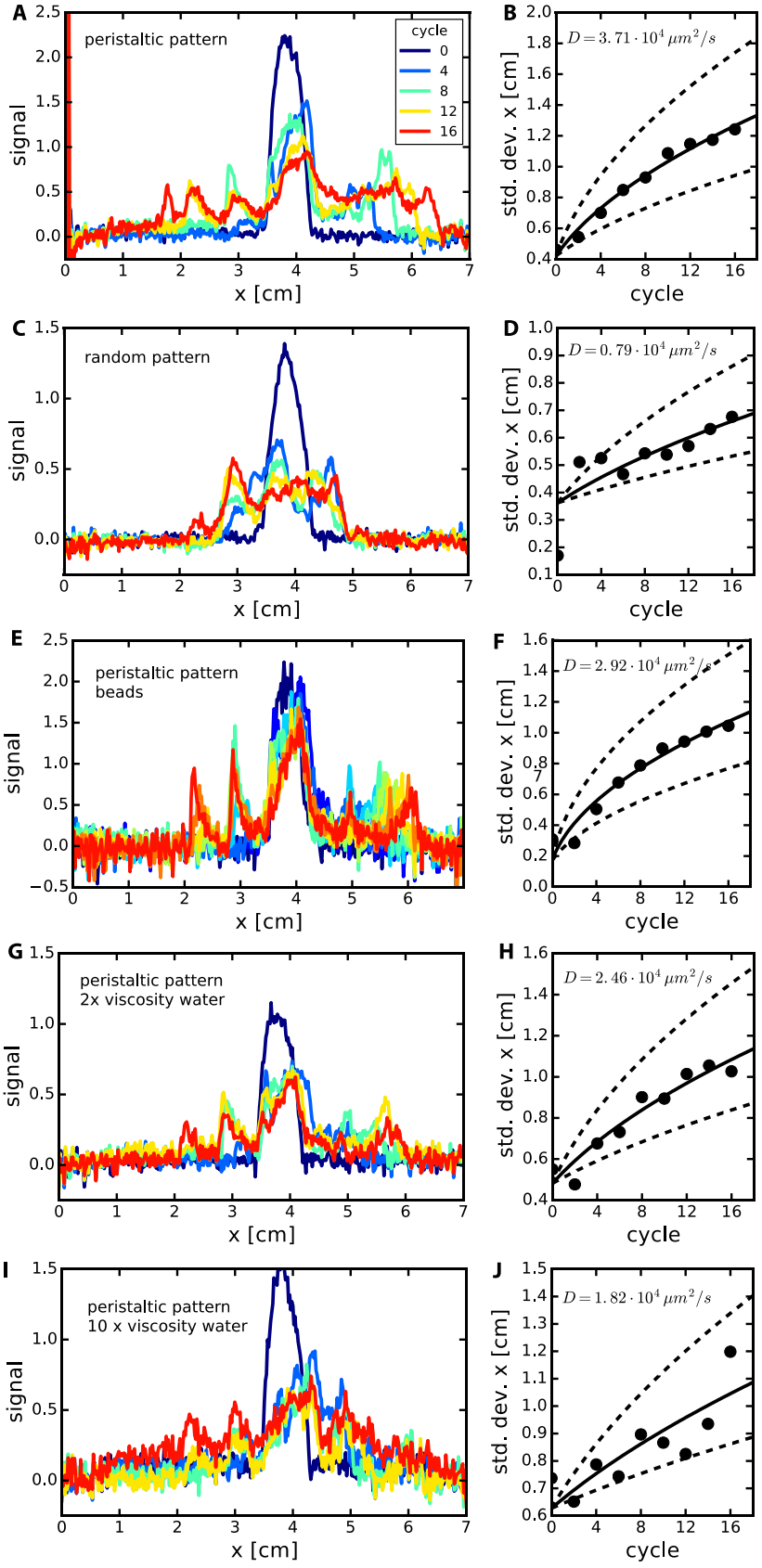
A
peristaltic pattern
cycle
0
4
8
12
16
signal
x [cm]
B
$D = 3.71 \cdot 10^4\ \mu m^2/s$
std. dev. x [cm]
cycle
C
random pattern
signal
x [cm]
D
$D = 0.79 \cdot 10^4\ \mu m^2/s$
std. dev. x [cm]
cycle
E
peristaltic pattern
beads
signal
x [cm]
F
$D = 2.92 \cdot 10^4\ \mu m^2/s$
std. dev. x [cm]
cycle
G
peristaltic pattern
2x viscosity water
signal
x [cm]
H
$D = 2.46 \cdot 10^4\ \mu m^2/s$
std. dev. x [cm]
cycle
I
peristaltic pattern
10 x viscosity water
signal
x [cm]
J
$D = 1.82 \cdot 10^4\ \mu m^2/s$
std. dev. x [cm]
cycle

**Figure 3.S5: Spreading of fluorescent dye and fluorescent beads along the mini-gut channel as a result of peristaltic mixing.** In each experiment, a small amount of low-diffusivity fluorescent dye (500 kDa FITC-dextran, $D \approx 20\ \mu m^2/s$ in water) or 2 μm fluorescent beads was injected into the mini-gut channel between valves 4 and 5, and the distributions of fluorescence intensity were measured after different numbers of cycles of valve contractions (each cycle includes a single contraction of each valve in the device); see SI text for detailed setup description. Left column: normalized fluorescence intensity along the channel (after flat-field correction and fluorescence background subtraction). Right column: characteristic width of the dye distribution (square root of the 2$^{nd}$ moment; standard deviation) as a function of the number of cycles of valve contraction. Solid lines: standard deviation fitted with a square root of the number of cycles, corresponding to a diffusion-like spreading of fluorescent dye (or beads) along the channel; dashed lines correspond to diffusion-like processes with twice and half as large diffusion constants. The diffusion constants are calculated based on a 120 sec periodicity of the valve contraction cycles. (A,B) Regular peristaltic contraction patterns with valves contracted from left to right, with fluorescent dye, and with the carrier fluid with the viscosity of water. (C,D) A random contraction pattern with the order of contractions randomly chosen for each cycle, with fluorescent dye, and with the carrier fluid with the viscosity of water. (E,F) Regular peristaltic contraction patterns, with 2 μm fluorescent beads, and with the carrier fluid with the viscosity of water. (G,H) and (I,J) Regular peristaltic contraction patterns, with fluorescent dye, and with the carrier fluids with the carrier fluid having a viscosity 2x (G,H) and 10x (I,J) higher than water.

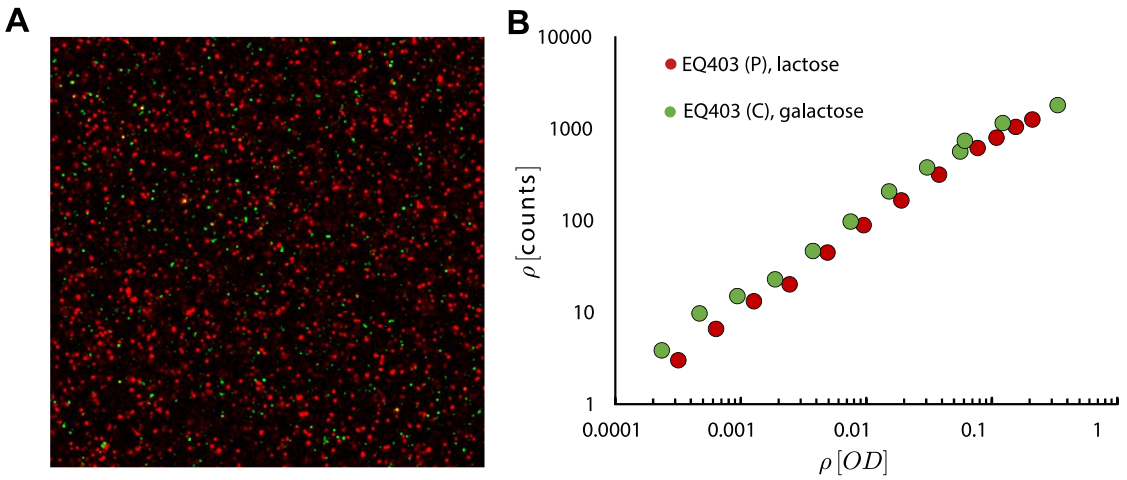


**Figure 3.S6. Cell-density measurements by image analysis.** (A) Representative image of the 465x465 µm confocal field of view at one z-level. In our characterization of the spatiotemporal dynamics of bacteria in the mini-gut, 90 such images were taken every 30 min along the length and across the depth of the mini-gut; see SI for details. (B) Calibration of cell-density. Measured cell counts (y-axis) for device loaded with exponentially growing cultures at different $OD_{600}$ (x-axis). Counts are performed for a volume of 3nl. Strain EQ386 ($C, \Delta lacIYZ$) (green) was grown with galactose as the sole carbon source, while strain EQ403 ($P, \Delta galK$) (red) was grown with lactose. Difference in the two counts can be attributed to the difference in the size of cells grown in the two cultures due to their different growth rates.

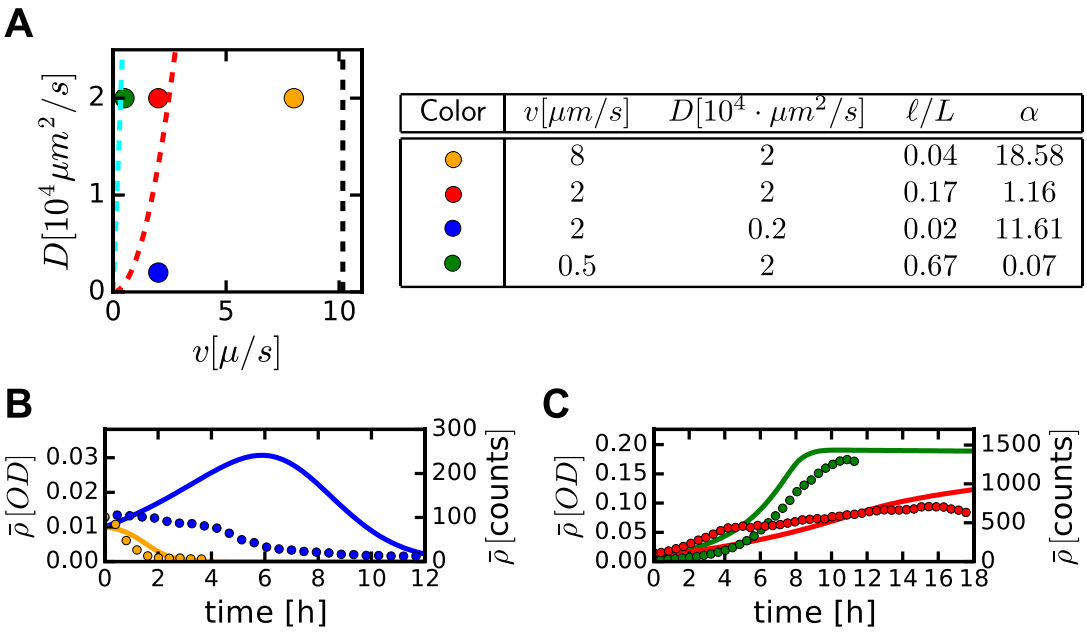


| Color | $v[\mu m/s]$ | $D[10^4 \cdot \mu m^2/s]$ | $\ell/L$ | $\alpha$ |
|---|---|---|---|---|
| ● | 8 | 2 | 0.04 | 18.58 |
| ● | 2 | 2 | 0.17 | 1.16 |
| ● | 2 | 0.2 | 0.02 | 11.61 |
| ● | 0.5 | 2 | 0.67 | 0.07 |

**Figure 3.S7 Bacterial growth in the mini-gut for different flow velocities and mixing strengths**. (A) Experimental paraments are shown by dots in the $v$ - $D$ phase diagram, with the values of $v$ and $D$ listed in the table. Dashed red and cyan lines are the same as those in Fig. 3.2B, delineating boundaries between different regimes in the theoretical model. Black line denotes the chemostat washout condition, $v^*$ (the white dashed line in Fig. 3.2B in the main text). (B) and **(**C) Experimentally observed (circles) and model predicted (lines) density for EQ403 cells as a function of time for different combinations of $D$ and $v$ . Cells are growing in lactose and cell density is averaged over the channel volume. (B) Washout conditions; (C) conditions resulting in steady states with stable bacterial populations in the channel. The agreement between the model and experiment is good, especially given that the model does not have any fitting parameters. The relatively large deviation between the model and experiment when both $v$ and $D$ are small (slow flow and weak mixing; blue symbols and line in B) may be because the simplified 1D model is not a completely accurate representation of the 3D mini-gut channel, especially at a low rate of peristalsis and weak mixing. In the real experiment, the cross-channel distribution of bacteria is not completely uniform (starting from the time of seeding), and this non-uniformity is expected to be coupled with the parabolic velocity profile (not captured by the 1D model). In addition, the low-rate peristaltic mixing in the channel may be less well approximated by a diffusion-like process.

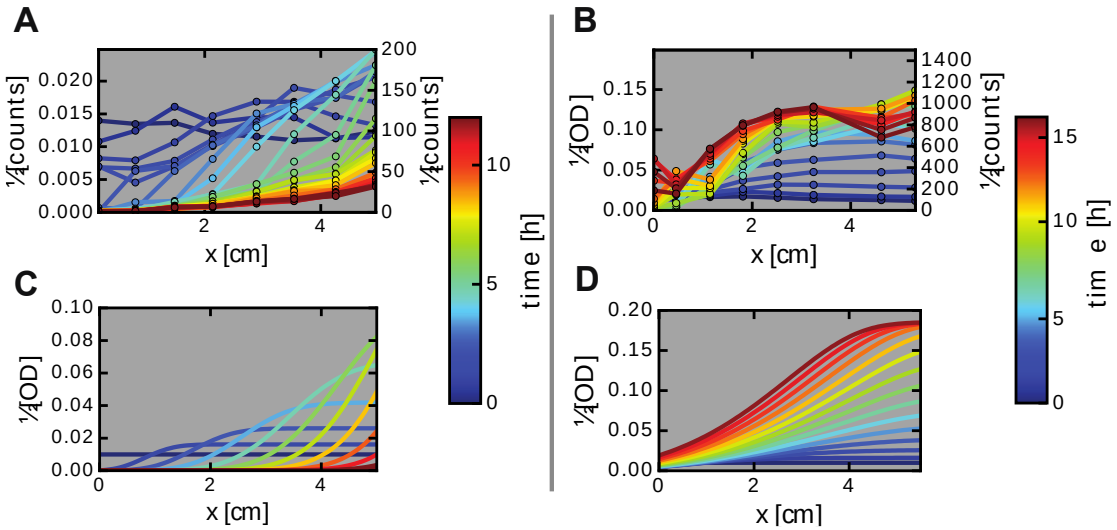


**Figure 3.S8 Effect of mixing in the mini-gut.** (A) and (B) Experimentally measured and (C) and (D) model predicted spatiotemporal growth dynamics. Flow velocity is constant, $v = 2\ \mu m/s$. (A) and (C) Weak peristaltic mixing, with $D = 0.2 \cdot 10^4\ \mu m^2/s$. (B) and (D) Stronger peristaltic mixing, with $D = 2 \cdot 10^4\ \mu m^2/s$ . (B) and (D) are same as Fig. 3.3D,G in the main text.

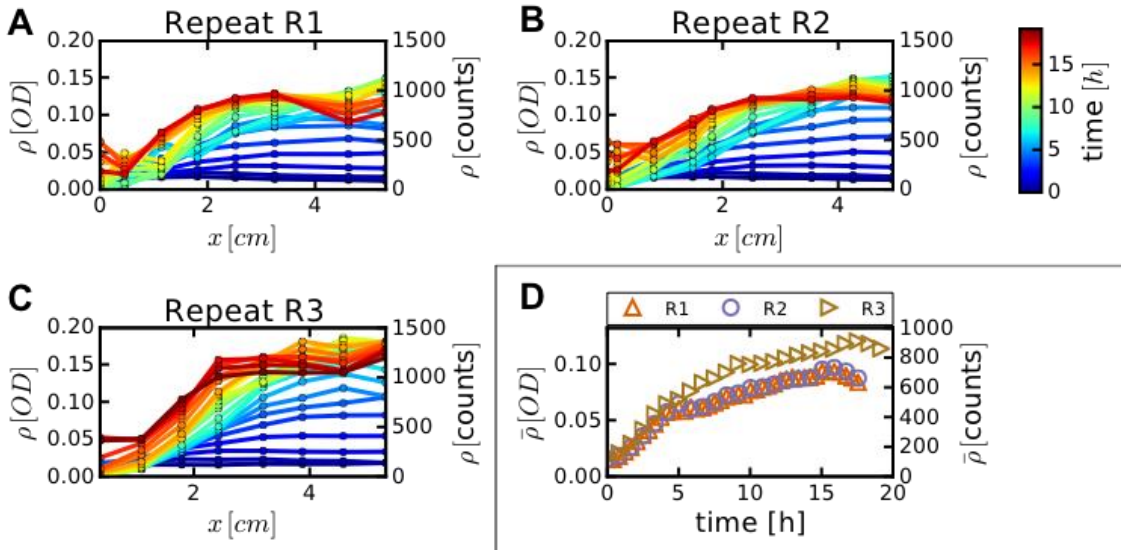


**Figure 3.S9 Reproducibility of spatio-temporal dynamics**. Growth dynamics in three separate experiments (EQ403 strain grown on lactose) at conditions resulting in non-uniform bacterial density along the channel, $D = 2 \cdot 10^4\ \mu m^2/s$, $v = 2\ \mu m/s$ (cf. Fig. 3.3D,G in the main text). R1 (A) same as Fig. 3.3D and R2 (B) is same as Fig. 3.4B. In the latter case, there were also bacteria from the EQ386 strain in the mini-gut channel, but they were not expected to have any effect on the growth of EQ403 bacteria. (D) Temporal evolution of bacterial density averaged over the channel volume in the three experiments shown in A-C.

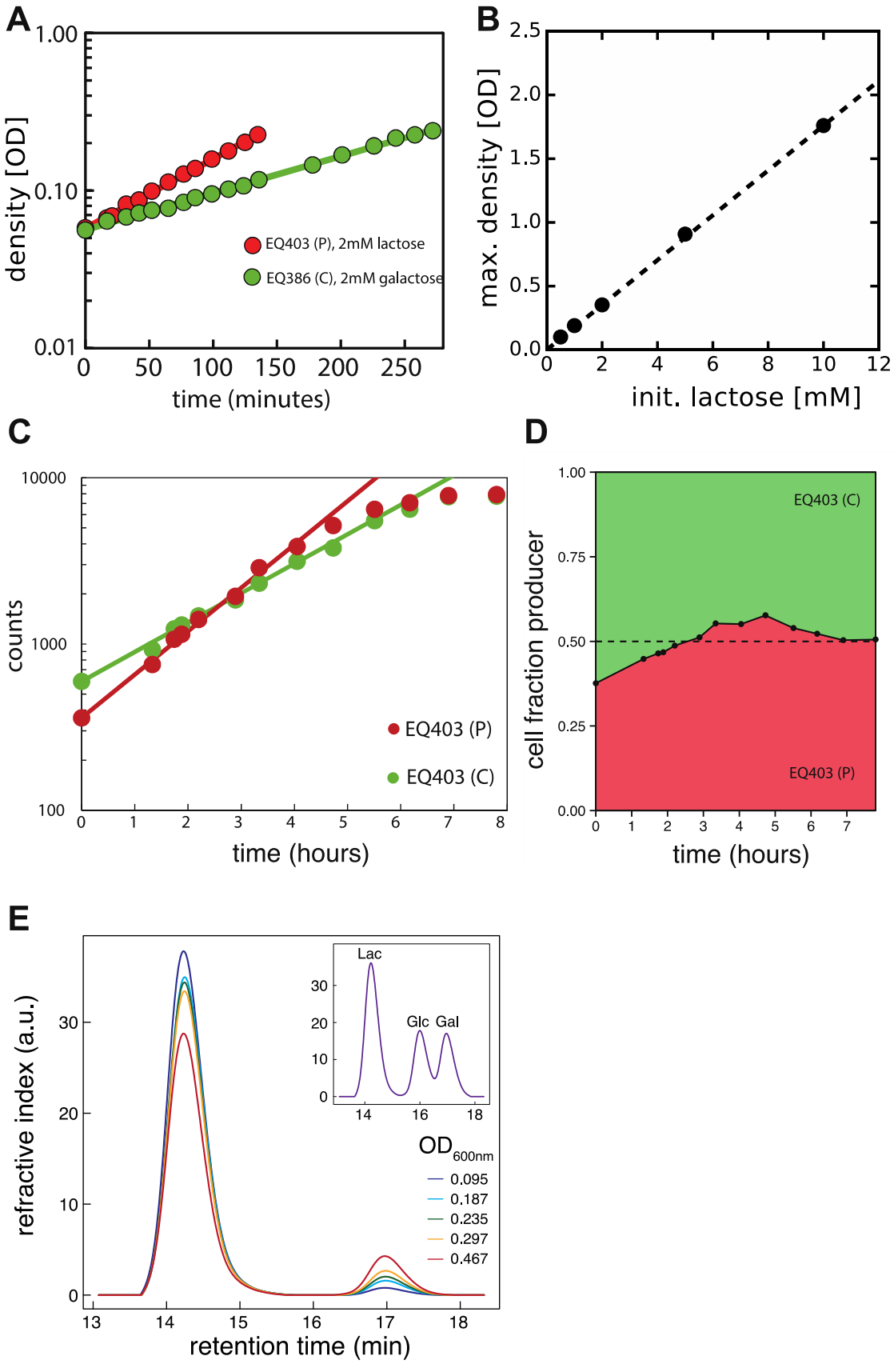
A
density [OD]
1.00
0.10
0.01
0
50
100
150
200
250
time (minutes)
EQ403 (P), 2mM lactose
EQ386 (C), 2mM galactose
B
max. density [OD]
2.5
2.0
1.5
1.0
0.5
0.0
0
2
4
6
8
10
12
init. lactose [mM]
C
counts
10000
1000
100
0
1
2
3
4
5
6
7
8
time (hours)
EQ403 (P)
EQ403 (C)
D
cell fraction producer
1.00
0.75
0.50
0.25
0.00
0
1
2
3
4
5
6
7
time (hours)
EQ403 (C)
EQ403 (P)
E
refractive index (a.u.)
30
20
10
0
13
14
15
16
17
18
retention time (min)
Lac
Glc
Gal
OD600nm
0.095
0.187
0.235
0.297
0.467

**Figure 3.S10 Growth and yield in batch culture**. (A) Exponential growth in batch culture for strain EQ403 (P, $\Delta$ gal, Ptet:mCherry) and strain EQ386 (C, $\Delta$lac, Ptet:gfp), with lactose and galactose, respectively, as the sole carbon source in the medium. The lines are exponential fits with growth rate of 0.32 $h^{-1}$ and 0.61 $h^{-1}$**.** (B) Saturation ODs for strain EQ403 growing in media with different lactose concentrations (with lactose as the sole carbon source). Line shows linear fit with a slope of 0.184 OD/mM. (C) and (D) Co-culturing of strains EQ403 (P) and EQ356 (C). Cells growing exponentially in a medium with lactose and galactose, respectively, were harvested, washed, and mixed into a new culture tube with fresh medium containing lactose as the sole carbon source, and with equal density fractions for each strain to initial total $OD_{600} = 0.025$. Cell density was measured by confocal imaging and counting: 1 $\mu l$ droplets of medium with cells were taken from the culture and put on a cover slip. The imaging and cell counting followed the same procedures as in the mini-gut device (Fig. 3.S5 and supplementary text). (C) shows cell density over time, (D) the relative fraction of the producer strain EQ403. (E) NQ1242 (delta galK strain without fluorescent plasmid) was grown in medium containing 10mM lactose, and lactose consumption as well as excretion of metabolites was monitored using HPLC. The lactose peak (at around 14.4 min retention time) got increasingly smaller as growth occurred, whereas the galacose peak rose (at around 17 min retention time). Glucose (at around 16 min retention time, see insert) was not detected during growth of NQ1242, indicating that the glucose moiety of all lactose is metabolized nearly instantly. The insert shows a chromatogram of 10mM standards of lactose (Lac), glucose (Glc), and galactose (Gal).

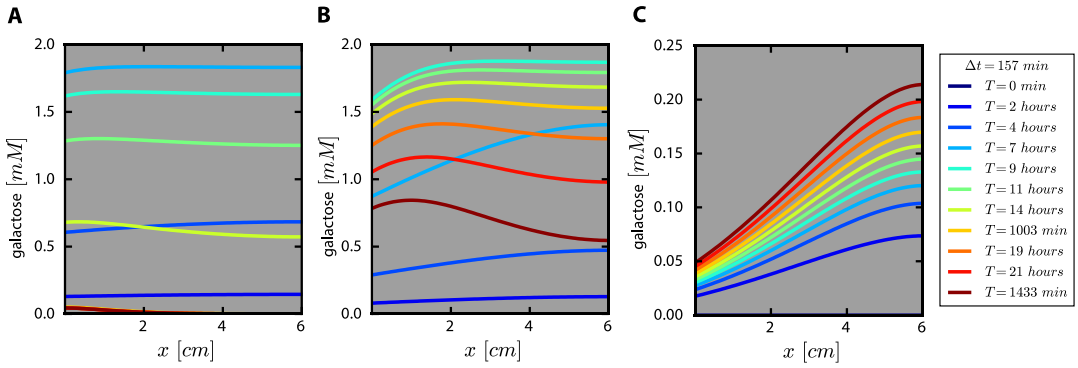


**Figure 3.S11** Model simulation of galactose profiles for the cross-feeding setup. In (A), (B), and (C), the velocity is by 0.5, 2.0, and 8.0 $\mu m/s$ , respectively. Other parameters are the same as in Fig. 3.4 main text.

## 3.7 Supplementary Tables

**Table S1. Simulation parameters used for comparison with experiments**. If not stated otherwise, used parameters for simulations are as given in this table.

| Parameter | Symbol | Value | Source |
|---|---|---|---|
| max growth rate of EQ403 on lactose | $\lambda_0$ or $\lambda_{0,P}$ | $0.61\ h^{-1}$ | measured in batch culture |
| max growth rate of EQ386 on galactose | $\lambda_{0,C}$ | $0.32\ h^{-1}$ | measured in batch culture |
| lactose yield of EQ403 | $Y_P$ | $0.184\ OD/mM$ | measured in batch culture |
| galactose yield EQ386 | $Y_C$ | $0.184\ OD/mM$ | measured in batch culture |
| Km of EQ403 for lactose | $K_{M,L}$ | $0.1\ mM$ | measured in batch culture |
| Km of EQ386 for galactose | $K_{M,G}$ | $0.1\ mM$ | measured in batch culture |
| channel length | $L$ | $6\ cm$ | set by device construction |
| effective diffusion coeff. | $D$ | $10^5 \ldots 10^7\ \mu m^2 \cdot s^{-1}$ varied by device setting | values estimated by the method of Fig. 3.S4 in this study |
| flow rate | $v$ | $0 \ldots 10\ \mu \cdot s^{-1}$ varied by device setting | set according to calibration |
| nutrient inflow concentration | $n_{in}$ | $2 - 10\ mM$ | varied by medium prep |

**Table S2. Strains used in this study.** Details of constructs are given in the supplementary text.

| Strain | Genotype | Plasmid | Parent | Source |
|---|---|---|---|---|
| **NCM3722** | | | | (91) |
| **MG1655Seq** | | | | (109) |
| **EQ356** | $\Delta lacIYZ$ | | NCM3722 | construct this study |
| **EQ386** | $\Delta lacIYZ$ | pZA31 Ptet-M2-GFP | EQ356 | plasmid construct this study |
| **NQ1242** | $\Delta galK$ | | NCM3722 | (93) |
| **EQ403** | $\Delta galK$ | pZA31 Ptet-mCh | NQ1242 | plasmid construct this study |

**Table S3. Primers used in this study**.

| Primer | **Sequence (5' to 3')** | Use |
|---|---|---|
| **lacI-P1** | GTAACGTTATACGATGTCGCAGAGTATGCCGG TGTCTCTTATCAGACCGTTGTAGGCTGGAGCTG CTTCG | lac*IZY* deletion |
| **lacY-P2** | GTGAAGCCCAGCGCCACCAGACCCAGCACCAG ATAAGCGCCCTGGAAACCCATATGAATATCCT CCTTAG | lac*IZY* deletion |
| lacY-ver-R | TGTTCAATGCGATCACTCCGTTATG | Verification of Δlac*IZY* |
| Ptet-mod-F2 | ATACTCGAGACTCTATCATTGATAGAGTTTGAC | PtetM2 cloning |
| Ptet-Kpn-R | AATGGTACCTTTCTCCTCTTTAATG | PtetM2 cloning |
| mCherry-Kpn-F | ATTGGTACCATGGTGAGCAAGGGCGAGGAGGA TAAC | mCherry cloning |
| mCherry-Bam-R | TATGGATCCTTACTTGTACAGCTCGTCCATGC | mCherry cloning |

## Acknowledgments

Chapter 3 covers the materials from “Effect of Flow and Peristaltic Mixing on Bacterial Growth in a Gut-like Channel” by Jonas Cremer, Igor Segota, Chih-Yu Yang, Markus Arnoldini, John T. Sauls, Zhongge Zhang, Edgar Gutierrez, Alex Groisman, and Terence Hwa, which was published in *Proceedings of the National Academy of Sciences* in 2016. The dissertation author was the co-author of this paper, in charge of gut-like device manufacture and flow characterization.

# CHAPTER 4

# CONCLUSION AND FUTURE WORKS

This thesis summarizes the application of microfluidic device on several bacterial experiments. Microfluidic devices are able to generate microenvironment that traditional methods could not achieve. Linear temperature gradients were created with different steepness, to study thermotaxis. Rather than aggregating at a certain range of temperature, *E.coli* aggregated around different temperature with different steepness of gradients. To establish a complete experiment, physics rules were applied to estimate time scale and calibrate non-uniform concentration. Although there is no study explaining such effect, repetitive experiments were done and shown as errorbars. Future work should be done in single cell level to further understand the mechanism.

For the study of the effect of flow and peristaltic mixing on bacterial growth in a gut-like channel, a “minigut” device was able to generate contraction-like motion and supply nutrient for bacterial growth. Without contraction, net flow caused washout and no steady state spatial profile of bacterial density was found. However, with contraction or peristaltic motion, spatial profile was found not only experimentally but also theoretically. The diffusion term in Fokker-Planck equation with growth rate term represents the peristalsis. Similar spatial distribution was shown between simulation and experiment,

which means contraction is critical for a steady state distribution of bacteria in gut. This device and experiment were the first step to human gut research. To understand more complicated mechanism, the device needs to be improved and renewed. For an instance, epithelial cells could be included with the device and oxygen gradient could be generated to achieve an environment closer to real gut.

# APPENDIX A

# POROUS DEVICE MADE OF POLYETHYLENE GLYCOL TO STUDY ENVIRONMENTAL STRESS RESPONSE OF BACTERIA

## A.1 Background

*Escherichia coli* (*E.coli*) are able to respond toward environmental stress including extremes of temperature, mechanical forces, and antibiotic. Although some stress response were well-studied, molecular regulation of mechanical stress response were still unknown. Years ago, Groisman lab in UC San Diego created a device allowing *E.coli* to grow within confined space. The device had three layers, vacuum chamber made of PDMS, microfluidic channels, and coverslip, from top to bottom. The microfluidic channels were made of agarose hydrogel, which was a porous material allowing molecular diffusion from nutrients channels to growth chambers. In order to seal the device with coverslip, PDMS surrounding agarose channels was connected to vacuum pipe, which generating pressure differences between vacuum chamber and atmosphere. Such pressure differences provided strong force to bind the microchannels and coverslip, forming a stable closed network. However, experimental results showed that even under high vacuum, *E.coli* were found to break the mechanical force and expand through the gap between microchannels and coverslip. One

possible reason was that agarose was not hard enough to generate strong and uniform force against coverslip. The expanding force of *E.coli* growth was high enough to break the binding force. A better strategy was needed to confine *E.coli* effectively. Here, we replaced agarose with polyethylene glycol (PEG), which was a porous material with higher rigidity comparing to agarose. Nonetheless, molding PEG to form microchannels was much more difficult due to its fragility. In consequence, we introduced a different protocol to perform the experiment. Microchannels and vacuum outlet were both made of PDMS as top layer. Coverslip was treated and covered by a PEG surface. The top layer was bound to PEG-treated coverslip, forming a closed network. Experiments showed that diffusion between nutrients channels and growth chambers though PEG surface were adequate for cell growth.

## A.2 Materials and Methods

### A.2.1 Multi-layer Device

The device has three layers, Polydimethylsiloxane (PDMS) channel as top layer, polyethylene glycol (PEG) as middle layer, and coverslip as bottom. There were three inlets for nutrients supply, one outlet, and two vacuum outlets for the top PDMS layer. The PDMS has 12 main channels (50μm depth) and 33 shallow channels (3μm depth)(Fig. B1). The main channels were filled with nutrients for the growth of *E.coli*, and the shallow channels have one dead-end aligning with the outlet, which created a semi-closed well for cell growth. The goal of the device was to contain single layer of cells throughout the chambers, which the depth should be slightly larger than the width of *E.coli* (0.5 μm). However, once applying the vacuum to seal the device, the ceiling of PDMS would be lowered due to the force generated by pressure differences between atmosphere and

vacuumed channels. Therefore, the depth of shallow channel should be much larger to allow rooms to prevent collapse of ceiling. The vacuum was adjusted strong enough to seal the top PDMS with middle and bottom layers, but not too strong to collapse the shallow channels, which 3 μm was about the suitable depth to reach the balance. The middle layer was made of polyethylene glycol (PEG, average Mn 700). With the PEG layer, nutrients from main channel in top PDMS could diffuse and expand horizontally toward the shallow channel, providing cells for growth. Middle PEG layer and bottom coverslip was stuck and bound firmly. First, in order to create a sticky surface on the coverslip to stick and bind the PEG layer, the coverslip was cleaned and plasma treated 40 seconds with oxygen, and was treated with the vapor made of a single drop of 3-Trimethoxysilyl propyl methacrylate on 120 $^{o}$C hot plate for 10 mins, covered and sealed by a glass lid. After cooling down, the coverslip was taped on two sides with 250 μm tape as a spacer. The PEG-water solution made of 40% PEG with 5%(??) VA-086 initiator was filled into the space made by the 250 μm tape and covered with another glass to seal and thus create a flat surface. The solidification of PEG-water solution was conducted by illumination of LED light (365nm) for 2 minutes. After illumination, the top glass was removed carefully and the PEG was well bound with coverslip. The PEG-treated coverslip was stored in purified water to prevent cracking.

### A.2.2 Experimental Setup

A droplet of *E.coli* culture was loaded on PEG-treated coverslip and immediately covered with PDMS channel from top. The vacuum was turned to ~ -20 kpi to bound the entire device. Three inlets and outlet were all filled with LB(Lysogeny broth). The

hydrodynamic flows from inlets to outlet in microchannels were driven by gravity with ambient pressure ~ 2 psi to prevent bubbles.

### A.2.3 Microscope and Imaging

The experiment was recorded overnight with Basler A102f camera, with inverse microscope and 40X/0.95 objective. Air pressure ~ 10 psi for several minutes was applied from inlets to force the *E.coli* flowing toward the end of the dead-end channels. One of the dead-end channels (shallow channels ~ 3 μm) was chosen to be recorded overnight, focusing on the bottom of channel. The image was taken every 20 minutes.

## A.3 Results and Future Work

Our goal was to create a limited size of space for bacteria growth, with nutrients provided by main channels through molecular diffusion. However, the results showed that vacuum was not strong enough to trap cells in the semi-closed chamber. *E.coli* were able to grow and expand through the gap of PDMS and PEG-treated coverslip, even before they grew and filled the entire semi-closed chamber (Fig. B2). One solution was to change the vacuum from -20 to -80 (full vacuum strength) kpi to increase the trapping force. In addition, the Sylgard184 PDMS was replaced with 1:1 mixed XP565/184 for higher rigidity to prevent the ceiling from collapse under strong vacuum. Nevertheless, the device was still not able to trap the cells. There was no significant difference comparing to the experiment with -20 kpi vacuum.

Since plasma treating would break the PEG surface, chemical treating between PEG and PDMS might be the next method to bind the entire channel. By treating 3-

trimethoxysilyl propyl methacrylate on the surfaces of PEG and PDMS, permanent binding might be achieved.

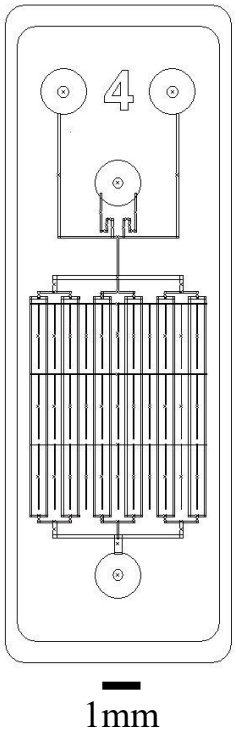


**Figure A.1:** Top PDMS network. Three inlets and one outlet are shown. Channels connecting from inlets to outlet are main channels, to supply nutrient for cell growth in shallow chambers, which are T-shapes with one dead end.

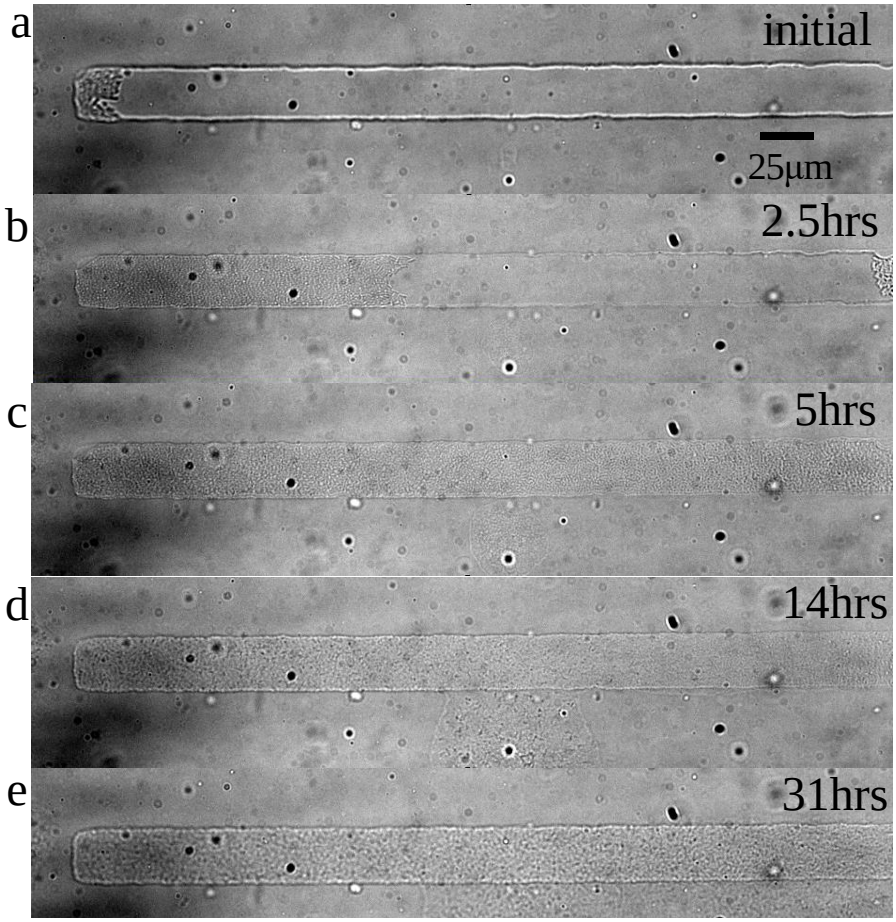


**Figure A.2:** (a)(b) *E.coli* started growing on one end of the chamber, (c) broke the downside wall, and (d)(e) expanded through the whole device. Time scale was shown.

## A.4 Acknowledgement

Appendix A is the project to apply porous device to study environmental stress response of *E.coli*. The project was not fully finished and more future works need to be done.

# BIBLIOGRAPHY


1. Bruus, Henrik. 2008. Theoretical microfluidics. Oxford: Oxford University Press.
2. Brown, D.A., and H.C. Berg. 1974. Temporal stimulation of chemotaxis in *Escherichia coli*. Proc Natl Acad Sci U S A. 71: 1388–1392.
3. Macnab, R.M., and D.E. Koshland. 1972. The gradient-sensing mechanism in bacterial chemotaxis. Proc Natl Acad Sci U S A. 69: 2509–2512.
4. Schnitzer, M.J., S.M. Block, and H.C. Berg. 1990. Strategies for Chemotaxis. Symp. Soc. Gen. Microbiol. 46: 15–34.
5. Schnitzer, M.J. 1993. Theory of continuum random walks and application to chemotaxis. Phys Rev E Stat Phys Plasmas Fluids Relat Interdiscip Topics. 48: 2553–2568.
6. Gegner, J.A., D.R. Graham, A.F. Roth, and F.W. Dahlquist. 1992. Assembly of an MCP receptor, CheW, and kinase CheA complex in the bacterial chemotaxis signal transduction pathway. Cell. 70: 975–982.
7. Hazelbauer, G.L., J.J. Falke, and J.S. Parkinson. 2008. Bacterial chemoreceptors: high-performance signaling in networked arrays. Trends Biochem Sci. 33: 9–19.
8. Sourjik, V. 2004. Receptor clustering and signal processing in *E. coli* chemotaxis. Trends Microbiol. 12: 569–576.
9. Sourjik, V., and H.C. Berg. 2002. Receptor sensitivity in bacterial chemotaxis. Proc Natl Acad Sci U S A. 99: 123–127.
10. Shioi, J., C.V. Dang, and B.L. Taylor. 1987. Oxygen as attractant and repellent in bacterial chemotaxis. J Bacteriol. 169: 3118–3123.
11. Adler, M., M. Erickstad, E. Gutierrez, and A. Groisman. 2012. Studies of bacterial aerotaxis in a microfluidic device. Lab Chip. 12: 4835–4847.
12. Adler, J., and W.W. Tso. 1974. Decision"-making in bacteria: chemotactic response of *Escherichia coli* to conflicting stimuli. Science. 184: 1292–1294.
13. Yang, Y., and V. Sourjik. 2012. Opposite responses by different chemoreceptors set a tunable preference point in *Escherichia coli* pH taxis. Mol Microbiol. 86: 1482–1489.
14. Zhuang, J., R. Wright Carlsen, and M. Sitti. 2015. pH-Taxis of Biohybrid Microsystems. Sci Rep. 5: 11403.
15. Paster, E., and W.S. Ryu. 2008. The thermal impulse response of *Escherichia coli*. Proc Natl Acad Sci U S A. 105: 5373–5377.

16. Yoney, A., and H. Salman. 2015. Precision and variability in bacterial temperature sensing. Biophys J. 108: 2427–2436.

17. Imae, Y., T. Mizuno, and K. Maeda. 1984. Chemosensory and thermosensory excitation in adaptation-deficient mutants of *Escherichia coli*. J Bacteriol. 159: 368–374.

18. Maeda, K., and Y. Imae. 1979. Thermosensory transduction in *Escherichia coli*: inhibition of the thermoresponse by L-serine. Proc Natl Acad Sci U S A. 76: 91–95.

19. Lee, L., T. Mizuno, and Y. Imae. 1988. Thermosensing properties of *Escherichia coli* tsr mutants defective in serine chemoreception. J Bacteriol. 170: 4769–4774.

20. Salman, H., and A. Libchaber. 2007. A concentration-dependent switch in the bacterial response to temperature. Nat Cell Biol. 9: 1098–1100.

21. Nara, T., L. Lee, and Y. Imae. 1991. Thermosensing ability of Trg and Tap chemoreceptors in *Escherichia coli*. J Bacteriol. 173: 1120–1124.

22. Nishiyama, S., S. Ohno, N. Ohta, Y. Inoue, H. Fukuoka, A. Ishijima, and I. Kawagishi. 2010. Thermosensing function of the *Escherichia coli* redox sensor Aer. J Bacteriol. 192: 1740–1743.

23. Demir, M., and H. Salman. 2012. Bacterial thermotaxis by speed modulation. Biophys J. 103: 1683–1690.

24. Oleksiuk, O., V. Jakovljevic, N. Vladimirov, R. Carvalho, E. Paster, W.S. Ryu, Y. Meir, N.S. Wingreen, M. Kollmann, and V. Sourjik. 2011. Thermal robustness of signaling in bacterial chemotaxis. Cell. 145: 312–321.

25. Salman, H., A. Zilman, C. Loverdo, M. Jeffroy, and A. Libchaber. 2006. Solitary modes of bacterial culture in a temperature gradient. Phys Rev Lett. 97: 118101.

26. Maeda, K., Y. Imae, J.I. Shioi, and F. Oosawa. 1976. Effect of temperature on motility and chemotaxis of *Escherichia coli*. J Bacteriol. 127: 1039–1046.

27. Demir, M., C. Douarche, A. Yoney, A. Libchaber, and H. Salman. 2011. Effects of population density and chemical environment on the behavior of *Escherichia coli* in shallow temperature gradients. Phys Biol. 8: 063001.

28. Paulick, A., V. Jakovljevic, S. Zhang, M. Erickstad, A. Groisman, Y. Meir, W.S. Ryu, N.S. Wingreen, and V. Sourjik. 2017. Mechanism of bidirectional thermotaxis in*Escherichia coli*. elife. 6.

29. Ahmed, T., T.S. Shimizu, and R. Stocker. 2010. Microfluidics for bacterial chemotaxis. Integr Biol (Camb). 2: 604–629.

30. Kalinin, Y.V., L. Jiang, Y. Tu, and M. Wu. 2009. Logarithmic sensing in *Escherichia coli* bacterial chemotaxis. Biophys J. 96: 2439–2448.

31. Mao, H., P.S. Cremer, and M.D. Manson. 2003. A sensitive, versatile microfluidic assay for bacterial chemotaxis. Proc Natl Acad Sci U S A. 100: 5449–5454.

32. Vandelinder, V., A.C.M. Ferreon, Y. Gambin, A.A. Deniz, and A. Groisman. 2009. High-resolution temperature-concentration diagram of alpha-synuclein conformation obtained from a single Förster resonance energy transfer image in a microfluidic device. Anal Chem. 81: 6929–6935.

33. Brody, J.P., P. Yager, R.E. Goldstein, and R.H. Austin. 1996. Biotechnology at low Reynolds numbers. Biophys J. 71: 3430–3441.

34. Polinkovsky, M., E. Gutierrez, A. Levchenko, and A. Groisman. 2009. Fine temporal control of the medium gas content and acidity and on-chip generation of series of oxygen concentrations for cell cultures. Lab Chip. 9: 1073–1084.

35. Rebbapragada, A., M.S. Johnson, G.P. Harding, A.J. Zuccarelli, H.M. Fletcher, I.B. Zhulin, and B.L. Taylor. 1997. The Aer protein and the serine chemoreceptor Tsr independently sense intracellular energy levels and transduce oxygen, redox, and energy signals for *Escherichia coli* behavior. Proc Natl Acad Sci U S A. 94: 10541–10546.

36. Zhulin, I.B., E.H. Rowsell, M.S. Johnson, and B.L. Taylor. 1997. Glycerol elicits energy taxis of *Escherichia coli* and Salmonella typhimurium. J Bacteriol. 179: 3196–3201.

37. Adler, J. 1969. Chemoreceptors in Bacteria. Science. 166: 1588–1597

38. Jinpian Diao, Lincoln Young, Sue Kim, Elizabeth A. Fogarty, Steven M. Heilman, Peng Zhou, Michael L. Shuler, Mingming Wu and Matthew P. DeLisa. 2006. A three-channel microfluidic device for generating static linear gradients and its application to the quantitative analysis of bacterial chemotaxis. Lab Chip. 6: 381–388.

39. Adler, J. and Bonnie Templeton. 1966. The Effect of Environmental Conditions on the Motility of *Escherichia coli*. J. gen. Microbiol.46, 175–184

40. Greer-Phillips, S.E., G. Alexandre, B.L. Taylor, and I.B. Zhulin. 2003. Aer and Tsr guide *Escherichia coli* in spatial gradients of oxidizable substrates. Microbiology (Reading, Engl). 149: 2661–2667.

41. Schwabe RF, Jobin C (2013) The microbiome and cancer. *Nature Reviews Cancer* 13(11):800–812.

42. Peterson DA, Frank DN, Pace NR, Gordon JI (2008) Metagenomic approaches for defining the pathogenesis of inflammatory bowel diseases. *Cell Host & Microbe* 3(6):417–427.

43. Stecher B, Hardt W-D (2008) The role of microbiota in infectious disease. *Trends Microbiol* 16(3):107–114.

44. Bahtiyar Yilmaz, Silvia Portugal, Tuan M. Tran, Raffaella Gozzelino, Susana Ramos, Joana Gomes, Ana Regalado,1 Peter J. Cowan, Anthony J.F. d'Apice, Anita S. Chong, Ogobara K. Doumbo, Boubacar Traore, Peter D. Crompton, Henrique Silveira, and Miguel P. Soares. (2014) Gut Microbiota Elicits a Protective Immune Response against Malaria Transmission. *Cell* 159(6):1277–1289.

45. Elaine Y. Hsiao, Sara W. McBride, Sophia Hsien, Gil Sharon, Embriette R. Hyde, Tyler McCue, Julian A. Codelli, Janet Chow, Sarah E. Reisman, Joseph F. Petrosino, Paul H. Patterson, and Sarkis K. Mazmanian. (2013) The microbiota modulates gut physiology and behavioral abnormalities associated with autism. *Cell* 155(7):1451–1463.

46. Peter J. Turnbaugh, Ruth E. Ley, Michael A. Mahowald, Vincent Magrini, Elaine R. Mardis, and Jeffrey I. Gordon. (2006) An obesity-associated gut microbiome with increased capacity for energy harvest. *Nature* 444(7122):1027–131.

47. Cho I, Blaser MJ (2012) The human microbiome: at the interface of health and disease. *Nat Rev Genet* 13(4):260–270.

48. Consortium THMP (2012) Structure, function and diversity of the healthy human microbiome. *Nature* 486(7402):207–214.

49. Paul B. Eckburg, Elisabeth M. Bik, Charles N. Bernstein, Elizabeth Purdom, Les Dethlefsen, Michael Sargent, Steven R. Gill, Karen E. Nelson, David A. Relman. (2005) Diversity of the Human Intestinal Microbial Flora. *Science (New York, NY)* 308(5728):1635–1638.

50. Daniel N. Frank, Allison L. St. Amand, Robert A. Feldman, Edgar C. Boedeker, Noam Harpaz, and Norman R. Pace. (2007) Molecular-phylogenetic characterization of microbial community imbalances in human inflammatory bowel diseases. *Proc Natl Acad Sci USA* 104(34):13780–13785.

51. Donaldson GP, Lee SM, Mazmanian SK (2016) Gut biogeography of the bacterial microbiota. *Nat Rev Micro* 14(1):20–32.

52. Philippe Marteau, Philippe Pochart, Joël Doré, Christel Béra-Maillet, Annick Bernalier, and Gérard Corthier. (2001) Comparative study of bacterial groups within the human cecal and fecal microbiota. *Appl Environ Microb* 67(10):4939–4942.

53. Gorbach SL, Plaut AG, Nahas L, Weinstein L, Spanknebel G, Levitan R. (1967) Studies of intestinal microflora. II. Microorganisms of the small intestine and their relation to oral and fecal flora. *Gastroenterology* 53.

54. Catherine Lozupone, Karoline Faust, Jeroen Raes, Jeremiah J. Faith, Daniel N. Frank, Jesse Zaneveld, Jeffrey I. Gordon, and Rob Knight. (2012) Identifying genomic and metabolic features that can underlie early successional and opportunistic lifestyles of human gut symbionts. *Genome Res* 22(10):1974–1984.

55. Verberkmoes NC, Russell AL, Shah M, Godzik A, Rosenquist M, Halfvarson J, Lefsrud MG, Apajalahti J, Tysk C, Hettich RL, Jansson JK. (2009) Shotgun metaproteomics of the human distal gut microbiota. *Isme J* 3(2):179–189.

56. Cullender TC, Chassaing B, Janzon A, Kumar K, Muller CE, Werner JJ, Angenent LT, Bell ME, Hay AG, Peterson DA, Walter J, Vijay-Kumar M, Gewirtz AT, Ley RE. (2013) Innate and Adaptive Immunity Interact to Quench Microbiome Flagellar Motility in the Gut. *Cell Host & Microbe* 14(5):571–581.

57. Mahowald MA, Rey FE, Seedorf H, Turnbaugh PJ, Fulton RS, Wollam A, Shah N, Wang C, Magrini V, Wilson RK, Cantarel BL, Coutinho PM, Henrissat B, Crock LW, Russell A, Verberkmoes NC, Hettich RL, Gordon JI. (2009) Characterizing a model human gut microbiota composed of members of its two dominant bacterial phyla. *Proc Nat Acad Sci USA* 106(14):5859–5864.

58. Sonnenburg JL, Angenent LT, Gordon JI (2004) Getting a grip on things: how do communities of bacterial symbionts become established in our intestine? *Nature Immunology* 5(6):569–573.

59. Bäckhed F, Ley RE, Sonnenburg JL, Peterson DA, Gordon JI (2005) Host-bacterial mutualism in the human intestine. *Science* 307(5717):1915–1920.

60. Lee SM, Donaldson GP, Mikulski Z, Boyajian S, Ley K, Mazmanian SK. (2013) Bacterial colonization factors control specificity and stability of the gut microbiota. *Nature* 501(7467):426–429.

61. L Albenberg, TV Esipova, CP Judge, K Bittinger, J Chen, A Laughlin, S Grunberg, RN Baldassano, JD Lewis, H Li, SR Thom, FD Bushman, SA Vinogradov, and GD Wu. (2014) Correlation Between Intraluminal Oxygen Gradient and Radial Partitioning of Intestinal Microbiota. *Gastroenterology* 147(5):1055–1063.e8.

62. Espey MG (2013) Role of oxygen gradients in shaping redox relationships between the human intestine and its microbiota. *Free Radical Biology and Medicine* 55:130–140.

63. Zoetendal EG, von Wright A, Vilpponen-Salmela T, Ben-Amor K, Akkermans AD, de Vos WM. (2002) Mucosa-associated bacteria in the human gastrointestinal tract

are uniformly distributed along the colon and differ from the community recovered from feces. *Appl Environ Microb* 68(7):3401–3407.

64. Codling C, O'Mahony L, Shanahan F, Quigley EMM, Marchesi JR (2009) A Molecular Analysis of Fecal and Mucosal Bacterial Communities in Irritable Bowel Syndrome. *Dig Dis Sci* 55(2):392–397.

65. Sarna SK (2010) *Colonic Motility: From Bench Side to Bedside* (Morgan & Claypool Life Sciences, San Rafael (CA)).

66. Gibson GR, Cummings JH, Macfarlane GT (1988) Use of a three-stage continuous culture system to study the effect of mucin on dissimilatory sulfate reduction and methanogenesis by mixed populations of human gut bacteria. *Appl Environ Microb* 54(11):2750–2755.

67. Payne AN, Zihler A, Chassard C, Lacroix C (2012) Advances and perspectives in in vitro human gut fermentation modeling. *Trends in biotechnology*.

68. McDonald JA, Schroeter K, Fuentes S, Heikamp-Dejong I, Khursigara CM, de Vos WM, Allen-Vercoe E. (2013) Evaluation of microbial community reproducibility, stability and composition in a human distal gut chemostat model. *J Microbiol Methods* 95(2):167–174.

69. Allen-Vercoe E (2013) Bringing the gut microbiota into focus through microbial culture: recent progress and future perspective. *Curr Opin Microbiol* 16(5):625–629.

70. Minekus M, Smeets-Peeters M, Bernalier A, Marol-Bonnin S, Havenaar R, Marteau P, Alric M, Fonty G, Huis in't Veld JH. (1999) A computer-controlled system to simulate conditions of the large intestine with peristaltic mixing, water absorption and absorption of fermentation products. *Appl Microbiol Biotechnol* 53(1):108–114.

71. Spratt P, Nicolella C, Pyle DL (2005) An Engineering Model of the Human Colon. *Food and Bioproducts Processing* 83(2):147–157.

72. Kim HJ, Huh D, Hamilton G, Ingber DE (2012) Human gut-on-a-chip inhabited by microbial flora that experiences intestinal peristalsis-like motions and flow. *Lab Chip* 12(12):2165–2174.

73. Kim HJ, Ingber DE (2013) Gut-on-a-Chip microenvironment induces human intestinal cells to undergo villus differentiation. *Integr Biol* 5(9):1130–1140.

74. Kim HJ, Li H, Collins JJ, Ingber DE (2016) Contributions of microbiome and mechanical deformation to intestinal bacterial overgrowth and inflammation in a human gut-on-a-chip. *Proc Nat Acad Sci USA* 113(1):E7–E15.

75. Dahmen KA, Nelson DR, Shnerb NM (1999) Population dynamics and non-Hermitian localization. *Statistical Mechanics of Biocomplexity*, Lecture Notes in Physics. (Springer Berlin Heidelberg), pp 124–151.

76. Dahman KA, Nelson DR, Shnerb NM (2000) Life and death near a windy oasis. *J Math Biol* 41(1):1–23.

77. Monod J (1949) The Growth of Bacterial Cultures. *Annu Rev Microbiol* 3(1):371–394.

78. Unger MA, Chou HP, Thorsen T, Scherer A, Quake SR (2000) Monolithic microfabricated valves and pumps by multilayer soft lithography. *Science* 288(5463):113–116.

79. Lærke HN, Arent S, Dalsgaard S, Bach Knudsen KE (2015) Effect of xylanases on ileal viscosity, intestinal fiber modification, and apparent ileal fiber and nutrient digestibility of rye and wheat in grow... - PubMed - NCBI. *Journal of Animal Science* 93(9):4323–4335.

80. Flint HJ, Duncan SH, Scott KP, Louis P (2007) Interactions and competition within the microbial community of the human colon: links between diet and health. *Environmental Microbiology* 9(5):1101–1111.

81. Belenguer A, Duncan SH, Calder AG, Holtrop G, Louis P, Lobley GE, Flint HJ. (2006) Two routes of metabolic cross-feeding between Bifidobacterium adolescentis and butyrate-producing anaerobes from the human gut. *Appl Environ Microb* 72(5):3593–3599.

82. Christl SU, Murgatroyd PR, Gibson GR, Cummings JH (1992) Production, metabolism, and excretion of hydrogen in the large intestine. *Gastroenterology* 102(4 Pt 1):1269–1277.

83. Narins RG ed. *Maxwell and Kleeman's Clinical Disorders of Fluid and Electrolyte Metabolism* (McGraw-Hill). 5 Ed.

84. Sarna SK (2010) Colonic Motility in Health.

85. Jonas Cremer, Markus Arnoldini and Terence Hwa. 2017. Effect of water flow and chemical environment on microbiota growth and composition in the human colon, PNAS.

86. Hammer J, Phillips SF (1993) Fluid loading of the human colon: Effects on segmental transit and stool composition. *Gastroenterology* 105(4):988–998.

87. Kashyap PC, Marcobal A, Ursell LK, Larauche M, Duboc H, Earle KA, Sonnenburg ED, Ferreyra JA, Higginbottom SK, Million M, Tache Y, Pasricha PJ, Knight R, Farrugia G, Sonnenburg JL. (2013) Complex Interactions Among Diet,

Gastrointestinal Transit, and Gut Microbiota in Humanized Mice. *Gastroenterology* 144(5):967–977.

88. Levitan R, Fordtran JS, Burrows BA, Ingelfinger FJ Water and salt absorption in the human colon. *J Clin Invest* 41.

89. Evans DF, Pye G, Bramley R, Clark AG, Dyson TJ, Hardcastle JD. (1988) Measurement of gastrointestinal pH profiles in normal ambulant human subjects. *Gut* 29(8):1035–1041.

90. Novick A, Szilard L (1950) Description of the chemostat. *Science* 112(2920):715–716.

91. Eric Soupene, Wally C. van Heeswijk, Jacqueline Plumbridge, Valley Stewart, Daniel Bertenthal, Haidy Lee, Gyaneshwar Prasad, Oleg Paliy, Parinya Charernnoppakul, and Sydney Kustu. (2003) Physiological Studies of *Escherichia coli* Strain MG1655: Growth Defects and Apparent Cross-Regulation of Gene Expression. *J Bacteriol* 185(18):5611–5626.

92. Datsenko KA, Wanner BL (2000) One-step inactivation of chromosomal genes in *Escherichia coli* K-12 using PCR products. *Proc Nat Acad Sci USA* 97(12):6640–6645.

93. Klumpp S, Zhang Z, Hwa T (2009) Growth rate-dependent global effects on gene expression in bacteria. *Cell* 139(7):1366–1375.

94. Levine E, Zhang Z, Kuhlman T, Hwa T (2007) Quantitative Characteristics of Gene Regulation by Small RNA. *PLoS Biol* 5(9):e229.

95. Shaner NC, Patterson GH, Davidson MW Advances in fluorescent protein technology. *jcsbiologistsorg*.

96. Neidhardt FC, Bloch PL, Smith DF (1974) Culture medium for enterobacteria. *J Bacteriol* 119(3):736–747.

97. Team RDC (2010) *R: A language and environment for statistical computing.* (R Foundation for Statistical Computing, Vienna).

98. Guyer JE, Wheeler D, Warren JA FiPy: Partial Differential Equations with Python. *Computing in Science & Engineering* 11(3):6–15.

99. Novick A, Szilard L (1950) Description of the chemostat. *Science* 112(2920):715–716.

100. Herbert D, Elsworth R, Telling RC (1956) The Continuous Culture of Bacteria; a Theoretical and Experimental Study. *Microbiology* 14(3):601–622.

101. Narins RG ed. *Maxwell and Kleeman's Clinical Disorders of Fluid and Electrolyte Metabolism* (McGraw-Hill). 5 Ed.

102. Phillips SF, Giller J (1973) The contribution of the colon to electrolyte and water conservation in man. *J Lab Clin Med*:733–746.

103. Ladas SD, Isaacs PE, Murphy GM, Sladen GE (1986) Fasting and postprandial ileal function in adapted ileostomates and normal subjects. *Gut* 27(8):906–912.

104. Devroede GJ, Phillips SF (1969) Studies of the perfusion technique for colonic absorption. *Gastroenterology* 56(1):92–100.

105. Cummings JH, Hill MJ, Jenkins DJ, Pearson JR, Wiggins HS (1976) Changes in fecal composition and colonic function due to cereal fiber. *Am J Clin Nutr* 29(12):1468–1473.

106. Johansson MEV, Larsson JMH, Hansson GC (2011) The two mucus layers of colon are organized by the MUC2 mucin, whereas the outer layer is a legislator of host-microbial interactions. *Proc Nat Acad Sci USA* 108(Supplement_1):4659–4665.

107. Moore WE, Holdeman LV (1974) Human fecal flora: the normal flora of 20 Japanese-Hawaiians. *Applied Microbiology* 27(5):961–979.

108. Van Houte J, Gibbons RJ (1966) Studies of the cultivable flora of normal human feces. *Antonie Van Leeuwenhoek* 32(2):212–222.

109. Frederick R. Blattner, Guy Plunkett III, Craig A. Bloch, Nicole T. Perna, Valerie Burland, Monica Riley, Julio Collado-Vides, Jeremy D. Glasner, Christopher K. Rode, George F. Mayhew, Jason Gregor, Nelson Wayne Davis, Heather A. Kirkpatrick, Michael A. Goeden, Debra J. Rose, Bob Mau, Ying Shao. (1997) The complete genome sequence of *Escherichia coli* K-12. *Science* 277(5331):1453–1462.

110. Jonas Cremer, Igor Segota, Chih-yu Yang, Markus Arnoldini, John T. Sauls, Zhongge Zhang, Edgar Gutierrez, Alex Groisman, Terence Hwa. 2016. The effect of flow and peristaltic mixing on bacterial growth in a gut-like channel, PNAS 113: 11414-9.